

DISS. ETH NO. 21452

Large Eddy Simulation of Tracer Dispersion in an Idealised River Canyon Setup

A dissertation submitted to
ETH ZURICH

for the degree of
DOCTOR OF SCIENCES

presented by

IRINA HEESE

Diplom-Physikerin, Westfälische Wilhelms-Universität Münster, Germany
Born on 08 October 1979
Citizen of Germany

Accepted on the recommendation of:

Prof. Dr. Heini Wernli
Dr. Andreas Dörnbrack
Dr. Johannes Keller

2014

Contents

Abstract

Kurzfassung

1	Introduction	1
2	Theoretical Background	5
2.1	The Atmospheric Boundary Layer	5
2.1.1	Mixed Layer	6
2.1.2	Residual Layer	6
2.1.3	Stable Boundary Layer	7
2.1.4	Surface Layer	7
2.1.5	Thermal Stratification	7
2.1.6	Influence of the Atmospheric Stratification on Smoke Plumes	7
2.2	Gaussian Plume Models	9
2.2.1	Theoretical Derivation	9
2.2.2	Stability Classes and σ -Values	10
2.2.3	Concentration Distribution	11
2.2.4	Statistical Theory of Taylor	12
2.3	Statistical Description of Turbulence	13
2.4	Large Eddy Simulation (LES)	15
2.4.1	Turbulent Scales	15
2.4.2	Governing Equations	16
2.4.3	Subgrid Model	17

3	EULAG	19
3.1	Governing Equations	19
3.2	Numerical Solution	21
3.2.1	One-Dimensional MPDATA	21
3.2.2	MPDATA as a Flow Solver	23
3.3	Applications	25
4	Model Setups	28
4.1	Horizontally Homogeneous and Inhomogeneous Flat Terrain	28
4.1.1	Computational Setups	28
4.1.2	Simulation Strategy	30
4.2	Simulations in an Idealised Aare Valley	30
4.2.1	Computational Setup	31
4.2.2	Tracer Dispersion	31
4.3	Simulations in an Idealised Aare Valley including a Building	32
4.3.1	Computational Setup	33
4.3.2	Tracer Dispersion	33
4.4	Acronyms and Symbols	34
5	Tracer Dispersion over Horizontally Homogeneous and Inhomogeneous Flat Terrain	37
5.1	Moderate Wind Speed without Thermal Convection	38
5.1.1	Velocity and Temperature Profiles	38
5.1.2	Tracer Release over Horizontally Homogeneous Terrain	39
5.1.2.1	Temporal Development	39
5.1.2.2	Influence of the Release Height	41
5.1.2.3	Concentration Distribution	44
5.1.3	Tracer Release over Horizontally Inhomogeneous Terrain	45
5.1.3.1	Influence of Release Height and Surface Shape	47
5.1.3.2	Concentration Distribution	48

5.1.4	Conclusions	49
5.2	Moderate Wind Speed including Thermal Convection	49
5.2.1	Velocity and Temperature Profiles	49
5.2.2	Tracer Release	49
5.2.3	Conclusions	52
5.3	Characteristics of the Concentration Distribution	53
6	Tracer Dispersion in an Idealised Aare Valley	55
6.1	Comparison of the EULAG Simulations with a Street Canyon Flow	55
6.1.1	Street Canyon Flow	55
6.1.2	Velocity and Concentration Profiles	57
6.1.3	Turbulent Kinetic Energy and Turbulent Statistics	59
6.1.4	Surface Heat Flux	63
6.1.4.1	Influence on the Turbulence	63
6.1.4.2	Influence on the Tracer Dispersion	63
6.1.5	Conclusions	65
6.2	Comparison of the EULAG Simulations with a Gaussian Plume Model	66
6.2.1	Analytical Gaussian Plume Model	66
6.2.2	First Results	67
6.2.3	Application of the Gaussian Plume Model in the Idealised Aare Canyon Setup	69
6.2.4	Plume Behaviour at the Pedestrian Height	71
6.2.5	Vertical Concentration Distribution	73
6.2.6	Conclusions	73
7	Tracer Dispersion with Idealised Building and Aare Valley	75
7.1	The Atmospheric Flow	75
7.1.1	Velocity Profiles	75
7.1.2	Turbulent Statistics	77
7.1.3	Conclusions	78
7.2	Tracer Dispersion	78
7.2.1	Contour Plots and Vertical Concentration Profiles	78
7.2.2	Conclusions	82

8 Summary and Outlook	83
References	87
Curriculum Vitae	93
Acknowledgements	96

Abstract

For decades Gaussian plume models have been used to predict pollutant emissions. Also the Paul Scherrer Institute (PSI) predicts the dispersion of radioactive particles in airborne discharges to estimate the dose rate at the PSI and its surroundings. Currently, the Gaussian plume model ESS41 is used for this purpose. While Gaussian models are very robust they lack the capability of taking into account the varying atmospheric background states and, especially, the dispersion of the plume in a complex topography.

An evaluation of different numerical models allowing for both a high spatial resolution of 2 m in the x -, y - and z -direction and a great flexibility, yielded the numerical flow solver EULAG as a suitable modelling system. The approach chosen in this thesis is to perform idealised simulations of passive tracer dispersion under neutral and convective thermal stratification. Three flow settings are applied, including a flat terrain, a river canyon and the latter setup extended by a building. The building is numerically treated as immersed boundary while terrain-following coordinates are used to simulate turbulent flow and tracer dispersion in the canyon setup. Only west wind conditions are investigated.

The following main results are found:

- Over a flat terrain both a surface roughness and a surface heat flux lead to a vertical plume spread. The tracer therefore reaches the ground at closer distances to the source and after shorter advection times in situations with increased roughness and/or surface heat fluxes.
- The idealised river canyon setup corresponds to an Isolated Roughness Flow (IRF) regime, showing the characteristic canyon flow profile. A turbulent downward transport of the tracer into the river canyon is observed due to the large eddies near the western shore. As a consequence, a simple surface roughness change in a flat terrain setup is not capable to mimic the canyon.
- Under convective thermal stratification the tracer dispersion is almost independent of release height and surface inhomogeneities.

- A large building in the river canyon setup influences the flow substantially in the vicinity of the building and leads to a higher pollutant concentration both behind the building and at the western shore of the river.

A simple roughness parameterisation used in the model ESS41 is thus not sufficient to mimic the canyon topography. Furthermore, the temporal development of the plume, including temporal and local concentration peaks, cannot be modelled. Using EULAG, there is no constraint on time steps and spatial resolution apart from numerical restrictions. The tracer concentration can be determined in the vicinity of the source and therefore an on-site dose calculation is in principle possible.

Based on the studies in this PhD thesis, EULAG can be considered as a suitable tool to replace the Gaussian plume model ESS41 for the modelling of tracer emissions at PSI in the future.

Kurzfassung

Seit Jahrzehnten werden Gauß-Fahnenmodelle verwendet, um die Ausbreitung von Schadstoffen vorherzusagen. Auch das Paul Scherrer Institut (PSI) verwendet ein Gaußmodell, um die Abgabe von luftgetragenen radioaktiven Teilchen zu modellieren und die Dosis am PSI und in der Umgebung abzuschätzen. Aktuell wird hierfür das Gauß-Fahnenmodell ESS41 verwendet. Gauß-Modelle sind sehr robust, können aber die variierenden atmosphärischen Hintergrundzustände und insbesondere die Ausbreitung im komplexen Gelände nicht berücksichtigen.

Ein Vergleich verschiedener numerischer Modelle, die mit einer hohen räumlichen Auflösung von 2 m in x -, y - und z -Richtung verwendet werden können, wurde EULAG als geeignetes Modell ausgewählt. Es wurden Computersimulationen zur Ausbreitung eines passiven Skalars bei neutraler und konvektiver thermischer Schichtung sowie Westwindbedingungen durchgeführt. Drei idealisierte Set-ups, bestehend aus einem flachen Gebiet, einem Flusstal und einem Flusstal mit zusätzlichem Gebäude, wurden verwendet. Die Modellierung des Gebäudes erfolgte mit dem numerischen Immersed Boundary (IMB) Ansatz, die Modellierung des Flusstals mit geländefolgenden Koordinaten.

Folgende Ergebnisse wurden gefunden:

- Über einer flachen Ebene führen sowohl ein Bodenwärmefluss als auch eine Oberflächenrauigkeit zu einer vertikalen Verbreiterung der Schadstofffahne. Der Tracer erreicht den Boden nach kürzerer Zeit und mit geringerem Abstand zur Quelle unter Bedingungen erhöhter Rauigkeit oder eines Bodenwärmeflusses.
- Das idealisierte Flusstal entspricht einem Isolated Roughness Flow (IRF) System und zeigt das zugehörige charakteristische Profil. Aufgrund der großen Wirbel am Westufer findet ein Abwärtstransport der Schadstoffe in das Flusstal statt. Eine Bodenrauigkeit wie im Set-up des flachen Geländes kann das Flusstal daher nicht nachbilden.
- Bei konvektiver atmosphärischer Schichtung ist die Schadstoffausbreitung nahezu unabhängig von Emissionshöhe und Bodenrauigkeit.

- Ein großes Gebäude im Flusstal hat einen signifikanten Einfluss in der Nähe des Gebäudes. Dies führt zu einer erhöhten Schadstoffkonzentration hinter dem Gebäude und am Westufer des Flusses.

Eine einfache Parametrisierung der Oberflächenrauigkeit, wie sie im Modell ESS41 verwendet wird, kann die idealisierte Aare-Topographie daher nicht ersetzen. Zudem kann das Modell die Entwicklung der Schadstofffahne mit zeitlichen und räumlichen Konzentrationsmaxima nicht modellieren. Bei der Verwendung von EULAG gibt es, mit Ausnahme der numerischen Restriktionen, keine Einschränkungen bei der Wahl der Zeitschritte und der räumlichen Auflösung. Dies steht im Gegensatz zu Gaußmodellen, die nah zur Quelle keine realistischen Werte berechnen und lediglich zeitgemittelte Konzentrationswerte bestimmen können.

Basierend auf den Studien dieser Arbeit stellt EULAG prinzipiell ein geeignetes Modell dar, um das Gauß-Fahnenmodell ESS41 in der Zukunft zu ersetzen.

Chapter 1

Introduction

Air pollution is a major problem for human health. Many pollutants are emitted within or slightly above the urban canopy layer where many people live (Figure 1.1). Urban areas and outskirts grow continuously (United Nations Population Division, 2011) therefore studies on air pollution in an urban environment are an increasing research issue.

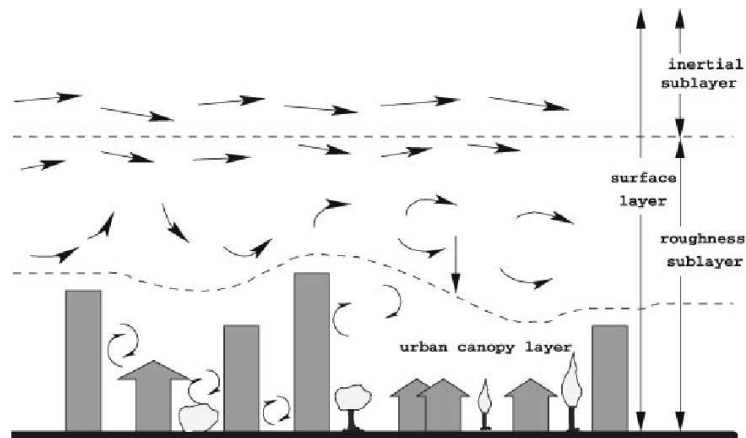


Figure 1.1: Wind flow through and above an urban region (Britter and Hanna, 2003).

For decades Gaussian plume models have been used to predict pollutant emissions. These models suppose a horizontal and vertical concentration distribution in a uniform flow under steady-state conditions. This is a simplified description, especially in the urban canopy layer where the flow is disturbed by buildings, trees and other obstacles (see Figure 1.1). A second type of models used for plume prediction are Lagrangian

dispersion models (Rotach et al., 1996; Kljun et al., 2002). These models simulate the different paths of the plume parcels based on a random walk process. Information about the flow field and other meteorological data is required to drive such models, and therefore, the results of a Lagrangian model are dependent on the input data set. In the third kind of models, applied in this PhD thesis, the Navier-Stokes equations are solved. Those high-resolution models are capable of taking into account both the topography and the building structures. The turbulent flow and the dispersion of tracers can be simulated with a high spatial and temporal resolution. There are mainly three approaches to solve the Navier-Stokes equations and simulate turbulent flows: Reynolds Averaged Navier-Stokes (RANS), Large Eddy Simulation (LES) and Direct Numerical Simulation (DNS). RANS models solve the turbulent spectrum based on a statistical treatment while DNS models compute the turbulent flow on all scales directly. LES models are a compromise between the two: The large-scale turbulent motions are solved directly while the small-scale motions are parameterised (see e.g. Pope (2000)). While DNS is rarely used due to the high computational costs the other two model techniques are applied over a wide range. Many studies have been performed to investigate flow and tracer dispersion over homogeneous and inhomogeneous flat terrain both analytically (Panofsky and Townsend, 1963; Taylor, 1968) and numerically (Peterson, 1969; Rao et al., 1973). The inhomogeneity is hereby considered as a surface roughness change. Other studies focused on flow and dispersion through urban canyons (Oke, 1988; Huang et al., 2000; Assimakopoulos et al., 2003). Some canyon studies consider different building configurations such as roofs (Kastner-Klein et al., 2004) or the influence of thermal effects (Sini et al., 1996; Park et al., 2012). Many authors investigated the flow over simple arrays of obstacles consisting of cubes (Hanna et al., 2002; Kanda et al., 2004; Coceal et al., 2006) or cuboids of different heights (Milliez and Carissimo, 2006; Xie et al., 2008). Some studies mimic real cities or obstacles in comparison with field experiments (Rotach et al., 2004; Yee, 2004; Xie and Castro, 2009) or wind tunnel studies (Smolarkiewicz et al., 2007). The described models and applications can be applied to different kinds of pollutants. In this PhD thesis the considered particles are radionuclides.

From nuclear and research facilities working with radioactive material, liquid and airborne discharges occur. For protecting environment and human health, the maximum effective dose of radiation is set by law to 1 millisievert per year. In Switzerland, the Swiss Federal Nuclear Safety Inspectorate (ENSI) defines a maximum dose rate for

each facility which must be below the legal safety limit. To estimate the dose rate of airborne discharges atmospheric dispersion models are used. A detailed guideline for dispersion modelling and computing the dose rate is defined in Swiss Federal Nuclear Safety Inspectorate (2009, G14), which is based on international guidelines by the International Atomic Energy Agency (IAEA) (International Atomic Energy Agency (IAEA), 2000, 2002). These guidelines are derived from research studies of Gifford and Briggs (Slade, 1968). For the Swiss nuclear power plants with only one emission source (stack) a maximum radioactive decay rate is specified. For the Paul Scherrer Institute (PSI), a research center in the North of Switzerland (Figure 1.2) the spatial and temporal emission pattern is different. The PSI has 13 sources (two main sources) and

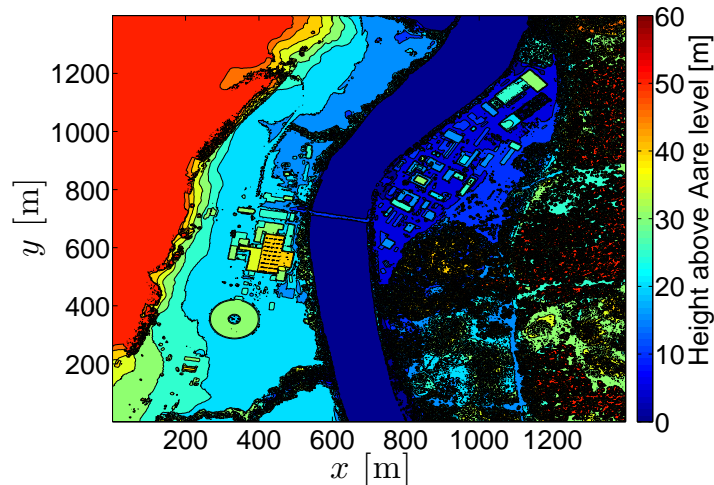


Figure 1.2: Topography of the Paul Scherrer Institute (PSI) and its surroundings. The reference height 0 m is defined at the level of the Aare river which divides the PSI into an eastern and a western part.

as a research institute temporally varying emissions. Therefore the PSI must guarantee that a certain dose rate is not exceeded by airborne emissions. Currently, the Gaussian plume model ESS41 is used to predict the dispersion of radioactive particles and to estimate the dose rate at the PSI and surroundings (defined as the region closer than 5 km to the sources) where the concentration of radionuclides is highest.

The emitted radionuclides are mainly positrons (β^+ emitters) (C^{11} , N^{13} , O^{15} , F^{18} , Ar^{41}) with a half-life time between some minutes and two hours. Once the positron is emitted, it annihilates with an electron by sending off γ radiation, which can be detected. In this PhD thesis only one main source at PSI is considered, the Zentrale

Fortluftanlage PSI West (ZFA), a stack at the northern wall of the building Experimentierhalle PSI West. As the concentration is proportional to the detected radiation the radioactive decay is not considered explicitly. Instead a passive scalar¹ is released into the flow and the concentration distribution is determined. The applied setup is not the PSI geometry as shown in Figure 1.2 but an idealised version including the river Aare and the ZFA in the final setup. The tracer dispersion at PSI is simulated with the numerical flow solver EULAG (see Chapter 3).

The main questions that will be addressed are:

1. How do release height, thermal stratification and the Aare canyon influence the tracer dispersion?
2. What are the advantages and disadvantages of EULAG compared to a Gaussian plume model?
3. Is EULAG capable to replace the Gaussian plume model ESS41 for radionuclide dispersion simulations in the future?

The following Chapter 2 provides an overview of the underlying theory, important for this PhD thesis. In Chapter 3 the flow solver EULAG is described. Chapter 4 deals with three different setups that are used in the subsequent chapters. The tracer dispersion over a homogeneous and inhomogeneous flat terrain is modelled in Chapter 5. An area with an idealised Aare valley is considered in Chapter 6 which is extended by a building representing the Experimentierhalle and the ZFA in Chapter 7. A summary and an outlook in Chapter 8 close this PhD thesis.

¹A passive scalar is a contaminant in a fluid that has no effect on the fluid motion itself.

Chapter 2

Theoretical Background

In this chapter the theoretical background on atmospheric boundary layer turbulence is briefly summarised. After a description of the atmospheric boundary layer and Gaussian plume models, the basic concepts of turbulence are presented. The chapter closes with a summary of LES.

2.1 The Atmospheric Boundary Layer

The atmospheric boundary layer (ABL) is the lowest part of the atmosphere that is adjacent to the earth's surface. In other words: the ABL is "that part of the troposphere that is directly influenced by the presence of the earth's surface, and responds to surface forcings with a timescale of about an hour or less." (Stull, 1989). The upper part of the troposphere is called free atmosphere. Characteristics of the ABL are a diurnal variation of temperature and the occurrence of turbulence as a very important transport process. The structure of the ABL mainly consists of four layers, which depend on the diurnal cycle¹: the mixed, residual, stable boundary and surface layer (see Figure 2.1). They are explained in the following.

¹The diurnal cycle as shown in Figure 2.1 is mainly relevant over land on sunny days and in our latitudes in the summer.

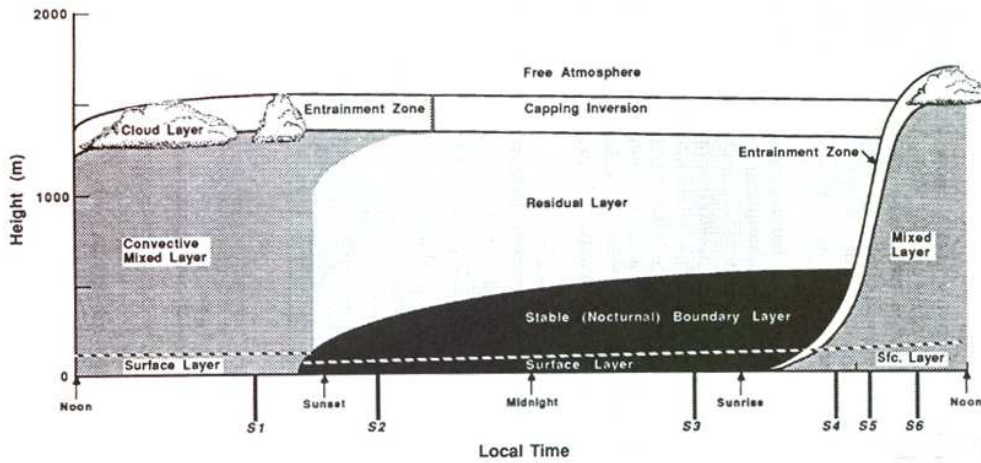


Figure 2.1: Diurnal evolution of the vertical structure of the atmospheric boundary layer. From Stull (1989)

2.1.1 Mixed Layer

The mixed layer (ML) or convective boundary layer (CBL) consists of three regions: the surface layer at the bottom, the mixed layer in the middle and the entrainment zone at the top. Buoyancy is the dominant effect for generating turbulence on sunny days. Warm air rises from the ground while colder air sinks from the top, which causes an intensive mixing. Therefore the meteorological characteristics (e.g., wind velocity or potential temperature) are nearly uniform with height in the upper part. The ML depth ranges from a few hundred to a few thousand meters in the late afternoon. The eddies can reach a size of 100 to 3000 m.

2.1.2 Residual Layer

The residual layer (RL) is not a boundary layer by definition, because it has no contact to the earth. It is presented as an exception from the rule. Before sunset the turbulence decreases because of the radiative cooling. The resulting RL is neutrally stratified and has the same mean state and concentration variables as in the ML.

2.1.3 Stable Boundary Layer

Below the RL the stable boundary layer (SBL) forms during the night. Around sunset when the energy input at the surface ceases, the turbulence decays. The air above the surface cools due to the heat flux from the atmosphere to the ground and the stability (strongly) increases. The height of the SBL is not very well defined because the top blends smoothly in the RL above.

2.1.4 Surface Layer

The surface layer (SL) or constant flux layer covers approximately the lowest 10 % of the ABL. It is independent of the thermal stratification, experiences typically a strong wind shear, and mechanical generation of turbulence is the dominant process, which is much bigger than the buoyant turbulence generation. The height of the SL is a few tens of meters.

2.1.5 Thermal Stratification

The static stability of the vertical stratification of an unsaturated atmosphere can be derived from the vertical gradient of the potential temperature θ :

$$\begin{aligned}\frac{\partial \theta}{\partial z} < 0 & \quad \text{convective} \\ \frac{\partial \theta}{\partial z} = 0 & \quad \text{neutral} \\ \frac{\partial \theta}{\partial z} > 0 & \quad \text{stable}\end{aligned}$$

2.1.6 Influence of the Atmospheric Stratification on Smoke Plumes

Tracers are emitted either episodically at regular time intervals (called puffs) or continuously (called plumes). In this PhD thesis a continuous emission is considered. Five different types of plumes can be identified depending on the wind speed and the vertical temperature profile called fanning, fumigation, looping, coning and lofting (Figure 2.2).

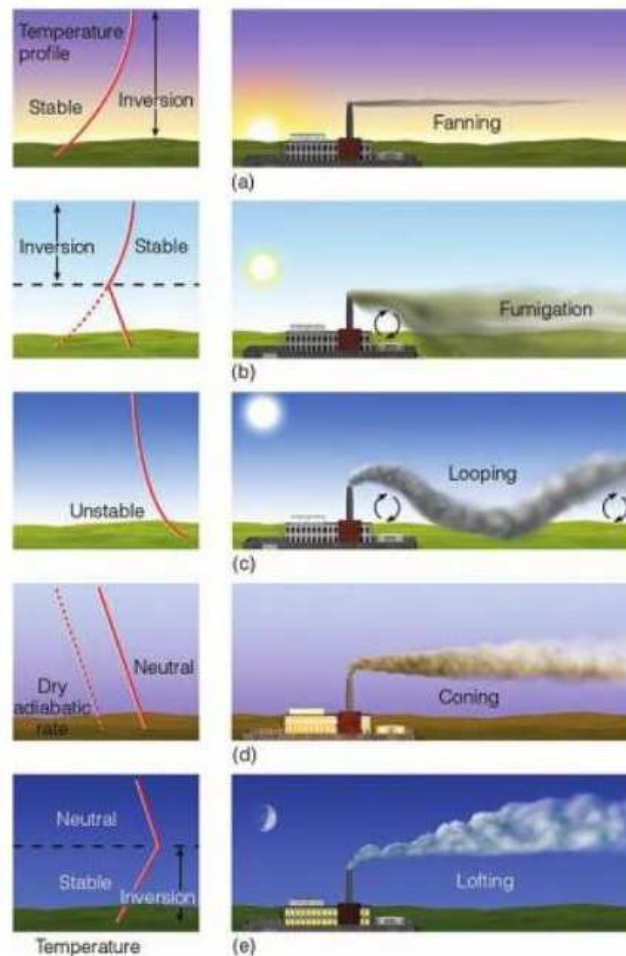


Figure 2.2: Different smoke plumes and corresponding temperature profiles. From Ahrens et al. (2012, p. 582).

- **Fanning:** There is almost no vertical spread and pollutants are transported over long distances without reaching the ground. This plume occurs mainly under strong inversions with a stable stratification, e.g. around sunrise.
- **Fumigation:** A stable air layer above the stack height and an unstable one below the stack lead to fumigation. There is a stronger downward transport of tracers. This condition is often found in the morning.
- **Looping:** Under unstable conditions convection causes large eddies and dominates the energy generation process. There is a fast mixing and dispersion due to the strong atmospheric turbulence under unstable conditions during a sunny day.

- Coning: At covered sky conditions and high wind speed (near-neutral stratification) the turbulence energy is mainly generated by mechanical production and causes small eddies. Vertical and horizontal motions are almost equal and the plume has the shape of a cone.
- Lofting: The contrary to fumigation. An unstable layer lies above the stack height while a stable one lies below. There is a greater upward dispersion and the pollutants are carried over long distances. This plume shape often occurs after sunset.

2.2 Gaussian Plume Models

Gaussian plume models are widely used and they belong to the oldest dispersion models that exist. The underlying principle is a Gaussian distribution function of the pollutant distribution. In the following the general equation of a Gaussian model is derived.

2.2.1 Theoretical Derivation

Gaussian plume models are based on the principle of the conservation of mass which implies that chemical transformation processes are negligible due to the short lifetime of the plume. The probability that a particle lies in the interval $[x, x + dx]$ is defined as the probability density $F(x)$. For a three-dimensional case, $G(y)$ and $H(z)$ can be defined in the same way. Assuming that the probability densities are independent of each other it follows:

$$\int_{-\infty}^{\infty} \int_{-\infty}^{\infty} \int_{-\infty}^{\infty} F(x) G(y) H(z) dx dy dz = 1$$

with the probability densities $F(x)$, $G(y)$ and $H(z)$ in the x -, y - and z -direction, respectively. The variable $\chi(x, y, z)$ describes the probability that the emitted pollutant from

a point source Q is located at (x,y,z) such that

$$Q = \int_{-\infty}^{\infty} \int_{-\infty}^{\infty} \int_{-\infty}^{\infty} \chi(x,y,z) dx dy dz \quad \text{with}$$

$$\chi(x,y,z) = Q \cdot F(x) G(y) H(z)$$

The main challenge is to define the form of the probability densities $F(x)$, $G(y)$ and $H(z)$. This can be done by applying Fick's law of diffusion. The result for χ is:²:

$$\chi(x,y,z) = \frac{Q}{2\pi\langle u \rangle \sigma_y(x) \sigma_z(x)} \exp \left(- \left(\frac{y^2}{2\sigma_y^2(x)} + \frac{z^2}{2\sigma_z^2(x)} \right) \right)$$

where $\langle u \rangle$ is the mean velocity at the source point, $\sigma_y(x)$ and $\sigma_z(x)$ denote the standard deviations of the concentration distribution, dependent on the distance x to the source, and thus the width and the depth of the plume. Hence, the form of the probability density functions $F(x)$, $G(y)$ and $H(z)$ are normal distributions. The σ -values must be determined as a function of x to predict the tracer concentration at different points and the success of the model results strongly depends on these values.

2.2.2 Stability Classes and σ -Values

The concentration distribution of the plume depends on the height above the surface, the distance from the source, the wind speed, the temperature, the surface roughness and the sampling time, i.e., the time between successive measurements of a physical quantity. In most cases stability classes are used to determine the σ -coefficients that describe the width and the depth of the plume (Pasquill, 1961). Based on net radiation and wind speed the atmospheric stability is divided into six classes A–F ranging from "very unstable" to "stable" (see Figure 2.3). $\sigma_y = \sigma_y(x)$ and $\sigma_z = \sigma_z(x)$ can be estimated for each class as a function of the distance x to source. Beginning in the 1960's many scientists tried to determine the σ -values experimentally, e.g., Pasquill (1961); Turner (1964); Klug (1969); Vogt (1977). Due to the different experimental conditions such as surface roughness or averaging time (e.g. hourly average or daily average) the values differ significantly. More sophisticated Gaussian models, known as second

²The interested reader is referred to Blackadar (1996)

Table 1: The Pasquill stability classes					
Stability class	Definition	Stability class	Definition		
A	very unstable	D	neutral		
B	unstable	E	slightly stable		
C	slightly unstable	F	stable		

Table 2: Meteorological conditions that define the Pasquill stability classes						
Surface windspeed		Daytime incoming solar radiation			Nighttime cloud cover	
m/s	mi/h	Strong	Moderate	Slight	> 50%	< 50%
< 2	< 5	A	A - B	B	E	F
2 - 3	5 - 7	A - B	B	C	E	F
3 - 5	7 - 11	B	B - C	C	D	E
5 - 6	11 - 13	C	C - D	D	D	D
> 6	> 13	C	D	D	D	D

Note: Class D applies to heavily overcast skies, at any windspeed day or night

Figure 2.3: The Pasquill stability classes.

generation models, determine the σ -values based on Monin-Obokhov similarity theory parameters. As this method is not used at PSI it is not further discussed.

2.2.3 Concentration Distribution

Measurements show a Gaussian distribution for the concentration in case of an undisturbed and time-averaged dispersion. For a continuous source the concentration χ at a point (x, y, z) is given by

$$\chi(x, y, z) = \underbrace{\frac{Q}{2\pi\langle u \rangle \sigma_y(x) \sigma_z(x)}}_I \underbrace{\exp\left(\frac{-y^2}{2\sigma_y^2(x)}\right)}_II \underbrace{\left[\exp\left(\frac{-(h_{\text{eff}} - z)^2}{2\sigma_z^2(x)}\right) + \exp\left(\frac{-(h_{\text{eff}} + z)^2}{2\sigma_z^2(x)}\right) \right]}_III \quad (2.1)$$

where z is the height above the ground and h_{eff} the effective height of the source. The first term represents the source, the second term the Gaussian concentration distribution in the horizontal and the third term the concentration distribution in the vertical. The second summand in term III denotes a virtual source to deal with particles that reach the surface. Due to this summand the plume reflects at the surface and the Gaussian distribution becomes asymmetric (see Figure 2.4).

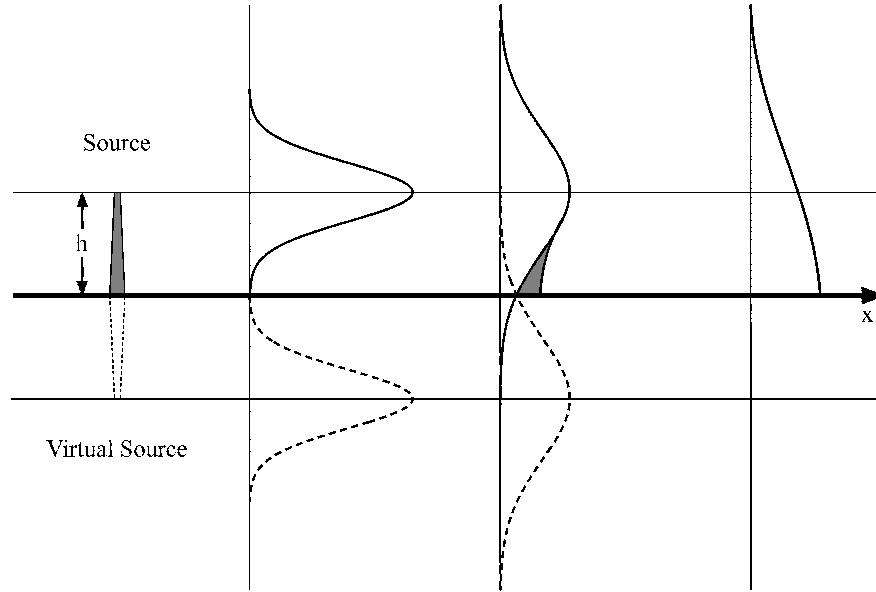


Figure 2.4: Vertical concentration distribution of a Gaussian plume model. A virtual source (dashed line) is added to deal with particles that reach the surface. The shaded area denotes the reflected material (middle) resulting in an asymmetric vertical profile (right).

2.2.4 Statistical Theory of Taylor

The statistical theory of Taylor states that the random particle displacement for a passive tracer can be found from the Lagrangian velocity autocorrelation. This is the correlation of the particle velocity at a time t and a later time $t + \tau$ after its release, where τ is a time lag. The Lagrangian integral time scale or memory time is defined as

$$T = \int_{-\infty}^{\infty} f(\tau) d\tau$$

with a dimensionless autocorrelation function:

$$f(\tau) = \frac{\overline{v(t)v(t+\tau)}}{\overline{v^2(\tau \equiv 0)}}.$$

v denotes the lateral particle velocity component and $\overline{v^2(0)}$ equals the local velocity variance σ^2 of the fluid. For short times, i.e. close to the source, the plume spread is

linear with time

$$\sigma^2 \sim t^2 \quad \text{for } t \ll T,$$

while σ grows parabolically with t for long times³

$$\sigma^2 \sim t \quad \text{for } t \gg T.$$

As a consequence, Gaussian plume models are incorrect close to the source (see Figure 2.5). The model ESS41 therefore does not consider distances closer than 200 m to the source for dose rate calculations.

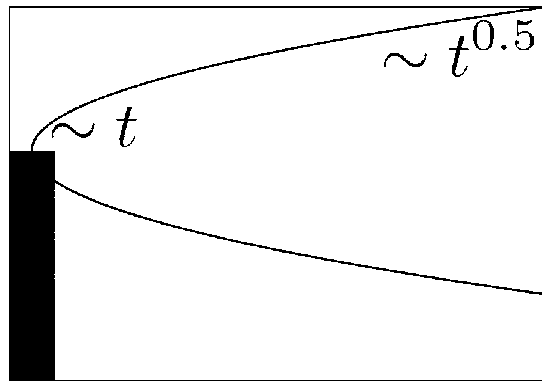


Figure 2.5: Outline of the plume spread dependent on the time t .

2.3 Statistical Description of Turbulence

The description of turbulent flows is one of the most complex problems in fluid dynamics. The characteristics cannot be described in detail but have to be considered as a stochastic process by means of a probability density function. Let P_k be the probability density that a variable k has a value in the interval $[k, k + \Delta k]$. Assuming stationarity the expected value $\langle k \rangle$ (expectation) is given by:

$$\langle k \rangle = \int_{-\infty}^{\infty} k P_k dk \quad (2.2)$$

³For a detailed derivation see e.g. Blackadar (1996).

The expectation is often called 'mean value' as an average over an infinite number of realisations of k . For different moments n of k , equation (2.2) becomes

$$\langle k^n \rangle = \int_{-\infty}^{\infty} k^n P_k dk$$

Central moments are defined as the deviation from the mean, $k' = (k - \langle k \rangle)$ and thus

$$\langle (k - \langle k \rangle)^n \rangle = \int_{-\infty}^{\infty} (k - \langle k \rangle)^n P_k dk$$

The first moment $n = 1$ is zero by definition, the second moment $n = 2$ is called variance. $n = 3$ and $n = 4$ are skewness and kurtosis, respectively. In statistics of measurements or computer simulations the so-called ensemble average (Equation 2.2) is not exactly known. As a proxy it is usually substituted by the temporal average of the measurements or simulation results. Over a homogeneous surface the spatial average is often used as a substitute.

An important variable for the description of a turbulent flow is the covariance that describes the turbulent transport of a quantity. In most cases one variable is a velocity component. Covariances used in this thesis are the turbulent fluxes of momentum $\langle u'w' \rangle$ and heat $\langle w'\theta' \rangle$. u and w are the velocities in streamwise and vertical direction, respectively and θ denotes the potential temperature. If the covariance does not vanish, a turbulent flow can transport a quantity without a mean velocity. The kinematic fluxes can be transformed into physical units by

$$\begin{aligned} \rho \langle u'w' \rangle &: \text{turbulent flux of momentum [Nm}^{-2}\text{]} \\ \rho c_p \langle w'\theta' \rangle &: \text{turbulent flux of sensible heat [Wm}^{-2}\text{]} \end{aligned}$$

where c_p denotes the specific heat of air at constant pressure and ρ the density. Another important variable is the turbulent kinetic energy (TKE) defined as

$$\text{TKE} = 0.5 (\langle u' \rangle^2 + \langle v' \rangle^2 + \langle w' \rangle^2).$$

It is a measure of the turbulence intensity in a flow. In the TKE budget equation all processes that generate turbulence are included. With $\frac{\text{TKE}}{m} = \bar{e}$ the following equation

can be derived:

$$\frac{\partial \bar{e}}{\partial t} = + \underbrace{\frac{g}{\bar{\theta}} \overline{w'\theta'}}_I - \underbrace{\overline{u'w'}}_{II} \frac{\partial U}{\partial z} - \underbrace{\frac{\partial \overline{w'e}}{\partial z}}_{III} - \underbrace{\frac{1}{\bar{\rho}} \frac{\partial \overline{w'p'}}{\partial z}}_{IV} - \underbrace{\varepsilon}_V \quad (2.3)$$

The terms represent the following⁴:

- I: buoyancy production
- II: shear / mechanical production
- III: turbulent transport
- IV: pressure transport
- V: molecular dissipation

2.4 Large Eddy Simulation (LES)

Large Eddy Simulation (LES) is an important modelling approach for simulating a turbulent flow, developed in meteorology (Fröhlich, 2006) and first published by Smagorinsky (Smagorinsky, 1963). There are two other approaches for modelling turbulence known as Reynolds Averaged Navier-Stokes (RANS) and Direct Numerical Simulation (DNS). While the DNS computes the turbulent flow on all length scales directly, the whole spectrum is modelled by statistical turbulent models when using RANS.

2.4.1 Turbulent Scales

In the atmosphere a wide span of eddies occur from millimeters to thousands of kilometers. Richardson found out that a cascade process exists in which energy is transported from the largest eddies to the smallest ones and finally into heat. Kolmogorov postulated the turbulence of the large scale is inhomogeneous and anisotropic while it can be considered as locally homogeneous and isotropic on small scales.

⁴For a comprehensive description of the different terms see e.g. Stull (1989).

The basic idea of LES is a separation of the variables into a large scale and a small scale part, called grid-scale (GS) and subgrid-scale (SGS) variables, respectively. While the large scales are computed explicitly the short-living small scale eddies, which are supposed to be homogeneous and isotrop with universal properties, are parameterised.

2.4.2 Governing Equations

For the separation of the two scales different approaches exist, the most common approach being a spatial filtering (Leonard, 1974)⁵. After separating the continuity equation, the Navier-Stokes equation, the first law of thermodynamics and the passive scalar conservation law, the filtered basic equations in a Cartesian coordinate system can be written as follows⁶:

$$\begin{aligned} \frac{\partial \langle u_j \rangle}{\partial x_j} &= 0 \\ \frac{\partial \langle u_i \rangle}{\partial t} + \frac{\partial \langle u_i u_j \rangle}{\partial x_j} &= -\frac{\partial \pi}{\partial x_j} + \frac{g}{\theta_0} (\langle \theta \rangle - \theta_0) \delta_{ij} - \frac{\partial \tau_{ij}}{\partial x_j} \\ \frac{\partial \langle \theta \rangle}{\partial t} + \frac{\partial \langle u_j \rangle \langle \theta \rangle}{\partial x_j} &= -\frac{\partial H_j}{\partial x_j} \end{aligned} \quad (2.4)$$

$$\frac{\partial \langle \varphi \rangle}{\partial t} + \frac{\partial \langle u_j \rangle \langle \varphi \rangle}{\partial x_j} = -\frac{\partial \phi_j}{\partial x_j} \quad (2.5)$$

$\langle \rangle$ denotes the GS part of the variables. It defines a numerical procedure with filter width Δ in contrast to the ensemble average when applying Reynolds averaging. The brackets are explicitly written in this section but omitted in the following chapters. x_j are the Cartesian coordinates ($j = 1, 2, 3$). $\langle u_i \rangle$, $\langle \varphi \rangle$ and $\langle \theta \rangle$ and θ_0 refer to the resolved-scale velocity, passive scalar, virtual potential temperature and the reference state potential temperature that is constant with height, respectively. $\pi = \frac{\langle p \rangle - p_0}{\rho_0} + \frac{2}{3}E$ represents the air pressure perturbation term with the reference pressure p_0 , the reference density ρ_0 and the SGS turbulent kinetic energy E . g denotes the gravitational acceleration parallel to x_3 . $\phi_j = (\langle u_j \varphi \rangle - \langle u_j \rangle \langle \varphi \rangle)$ represents the subgrid turbulent flux of a passive scalar, $H_j = (\langle u_j \theta \rangle - \langle u_j \rangle \langle \theta \rangle)$ the subgrid turbulent temperature flux and $\tau_{ij} = (\langle u_i u_j \rangle - \langle u_i \rangle \langle u_j \rangle)$ the subgrid stress tensor.

⁵A detailed description of the filter can be found in Fröhlich (2006).

⁶The governing equations in a terrain-following coordinate system that are used within this thesis are presented in Section 3.1.

2.4.3 Subgrid Model

The subgrid turbulent fluxes τ_{ij} , H_j and ϕ_j must be parameterised. In EULAG two subgrid models can be used: the Smagorinsky approach (Smagorinsky, 1963) and Schumann's parameterisation (Schumann, 1991). In this thesis Schumann's parameterisation is applied and therefore briefly described.

Set (2.5) contains six equations with six unknown quantities and additionally the subgrid terms τ_{ij} , H_j and ϕ_j . These terms must be related to the resolved-scale quantities and are therefore defined as:

$$\begin{aligned}\tau_{ij} &= -k_m \left(\frac{\partial \langle u_j \rangle}{\partial x_i} + \frac{\partial \langle u_i \rangle}{\partial x_j} \right) \\ H_j &= -k_h \frac{\partial \langle \theta \rangle}{\partial x_j} \\ \phi_j &= -k_\phi \frac{\partial \langle \varphi \rangle}{\partial x_j}\end{aligned}$$

where k_m is the eddy viscosity and k_h and k_ϕ are the eddy diffusivities. To determine these coefficients an additional equation is derived from set (2.5) with the subgrid turbulent kinetic energy E that satisfies the following equation⁷:

$$\frac{\partial E}{\partial t} + \frac{\partial \langle u_j \rangle E}{\partial x_j} = -\tau_{ij} \frac{\partial \langle u_i \rangle}{\partial x_j} + \frac{g}{\theta_0} H_3 - \frac{\partial}{\partial x_j} (T_j + P_j) - \varepsilon$$

T_j symbolises the turbulent transport term, $P_j = (\langle \pi u_j \rangle - \langle \pi \rangle \langle u_j \rangle)$ the pressure term and ε the viscous dissipation rate.

Based on E the coefficients k_m , k_h and k_ϕ are written as

$$\begin{aligned}k_m &= c_m \lambda E^{(\frac{1}{2})} \\ k_h &= k_\phi = \frac{k_m}{\text{Pr}}\end{aligned}$$

where λ , Pr and c_m denote the mixing length, the Prandtl number and a constant,

⁷This equation should not be confused with equation 2.3 that deals with the resolved-scale turbulent kinetic energy.

respectively. T_j , P_j and ε can be parameterised as follows:

$$T_j + P_j = -c_e k_m \frac{\partial E}{\partial x_j}$$
$$\varepsilon = c_\varepsilon \frac{E^{\frac{2}{3}}}{\lambda}$$

Here c_e and c_ε are constants. The mixing length λ is defined as:

$$\lambda = \min(\Delta, c_l z)$$

with

$$\Delta = \frac{1}{3}(\Delta x + \Delta y + \Delta z)$$

The used constants get the following values: $c_m = 0.0856$, $c_e = 2.0$, $c_\varepsilon = 0.845$ and $c_l = 0.845$ (Schumann, 1991). For a comprehensive description of the model see e.g. Sorbjan (1996).

Chapter 3

EULAG

EULAG is an anelastic, non-hydrostatic flow solver that is used to simulate all-scale geophysical flows either in an Eulerian or in a semi-Lagrangian framework. In the following, the basic set of equations used in this thesis shall be presented and an overview of different applications using EULAG is given.

3.1 Governing Equations

For modelling the Aare canyon a curvilinear coordinate transformation based on the classical terrain-following Gal-Chen and Somerville transformation (Gal-Chen and Somerville, 1975) is used. The transformed coordinates are given by

$$[\bar{x}_1, \bar{x}_2, \bar{x}_3] = \left[x_1, x_2, \frac{H(x_3 - h)}{H - h} \right]$$

where H is the model depth, and h the height of the lower boundary. In the governing equations the coordinate transformation is considered by the transformation coefficients

$$G_{ij} = \sum_{k=1}^n \frac{\partial \bar{x}_i}{\partial x_k} \frac{\partial \bar{x}_j}{\partial x_k}$$

and the Jacobian of the coordinate transformation

$$\bar{G} = (\det(G_{ij}))^{-\frac{1}{2}}.$$

For the small-scale dispersion of pollutants studied in this thesis, the incompressible Boussinesq approximation is applied leading to the following governing equations:

$$\frac{\partial}{\partial \bar{x}_j} (\rho^* \bar{u}_j^*) = 0 \quad (3.1)$$

$$\frac{\partial u_i}{\partial \bar{t}} + \frac{\partial}{\partial \bar{x}_j} (u_i \bar{u}_j^*) = -G_{ij} \frac{\partial \pi'}{\partial \bar{x}_j} + g \frac{\theta'}{\theta_b} - \frac{\partial \tau_{ij}}{\partial \bar{x}_j} - \beta (u_i - u_i^B) \quad (3.2)$$

$$\frac{\partial \theta'}{\partial \bar{t}} + \frac{\partial}{\partial \bar{x}_j} (\theta' \bar{u}_j^*) = -\frac{\partial}{\partial \bar{x}_j} (\theta_e \bar{u}_j^*) - \frac{\partial H_j}{\partial \bar{x}_j} \quad (3.3)$$

$$\frac{\partial \phi}{\partial \bar{t}} + \frac{\partial}{\partial \bar{x}_j} (\phi \bar{u}_j^*) = -\frac{\partial \phi_j}{\partial \bar{x}_j} - \beta (\phi - \phi^B) \quad (3.4)$$

$$\frac{\partial E}{\partial \bar{t}} + \frac{\partial}{\partial \bar{x}_j} (E \bar{u}_j^*) = -\tau_{ij} \frac{\partial u_i}{\partial \bar{x}_j} + \frac{g}{\theta_b} H_3 - \frac{\partial T_j}{\partial x_j} - \varepsilon - \beta (E - E^B) \quad (3.5)$$

Rotational effects are neglected in all simulations discussed in this thesis. u_i are the components of the physical velocity vector ($i = 1, 2, 3$). θ , ρ , ϕ and g denote potential temperature, density, passive scalar and gravitational acceleration that is parallel to x_3 , respectively. Primes indicate deviations from the hydrostatically balanced ambient states which again are symbolised by the subscript e . The subscript b refers to the Boussinesq reference state. $\pi' = \frac{(p-p_e)}{\rho_b}$ is a density normalised pressure added by a term that is proportional to the subgrid turbulent kinetic energy E .

The terms τ_{ij} , H_j and ϕ_j are the stress tensor, the subgrid turbulent fluxes of heat and a passive scalar, respectively. Using Schumann's parameterisation as a turbulence closure, an additional equation (3.5) for the subgrid turbulent kinetic energy must be solved (see Section 2.4.3). The variables T_j , P_j and ε appearing in this equation are the turbulent transport term, the pressure term and the viscous dissipation rate.

The building in the third setup (see Section 4.3) is modelled using the immersed boundary (IMB) method (Goldstein et al., 1993; Mittal and Iaccarino, 2005) whereby buildings and obstacles can be resolved explicitly with a high resolution. This numerical approach enters the equations (3.2), (3.4) and (3.5) through the coefficient β . It denotes additional forcings that appear because of a virtual building symbolised by the superscript B . In contrast to a terrain-following coordinate system perpendicular walls

and rectangular edges can be modelled. Furthermore, the existence of virtual obstacles to approximate internal boundary conditions leads to a computational simplicity and thus a high performance. Within the body of the solid building $u_i^B \equiv \varphi^B \equiv E^B \equiv 0$. The IMB approach is applied to model the Experimentierhalle at PSI that represents the source of the radionuclides (see Section 4.3 and Chapter 7).

3.2 Numerical Solution

MPDATA (Multidimensional Positive Definite Advection Transport Algorithm) is a finite-difference numerical solver to solve the generalised transport equation (3.11). It was developed to model the transport of non-negative thermodynamic variables in atmospheric models (Smolarkiewicz, 1983). During the years the algorithm was extended to advection-diffusion equations with further application, e.g. the use of curvilinear frameworks (Smolarkiewicz and Margolin, 1998). The algorithm is iterative and consists of a series of donor cell steps. The first step leads to a first-order accurate solution while the following steps compensate higher-order truncation errors. It is analytically derived from an analysis of the upwind scheme.

3.2.1 One-Dimensional MPDATA

As an example for the MPDATA scheme the one-dimensional transport of a scalar variable in a uniform flow is described. The advection equation for a scalar variable $\psi = \psi(x, t)$ is given by

$$\frac{\partial \psi}{\partial t} = -\frac{\partial}{\partial x}(u\psi), \quad (3.6)$$

where u is a nonzero velocity. The upstream or donor cell approximation to this equation is written as

$$\psi_i^{n+1} = \psi_i^n - \alpha^+ (\psi_i^n - \psi_{i-1}^n) - \alpha^- (\psi_{i+1}^n - \psi_i^n) \quad (3.7)$$

with

$$\begin{aligned}\alpha &= \frac{u\Delta t}{\Delta x} \\ \alpha^+ &= \frac{1}{2}(\alpha + |\alpha|) \\ \alpha^- &= \frac{1}{2}(\alpha - |\alpha|) \\ |\alpha| &= \alpha^+ - \alpha^-\end{aligned}$$

Performing von Neumann stability analysis one can see that a solution to equation (3.7) is only stable if

$$|\alpha| = \frac{|u|\Delta t}{\Delta x} \leq 1 \iff |u| \leq \frac{\Delta x}{\Delta t}$$

where Δx and Δt are the length of a grid cell and the time step, respectively. In other words, the real velocity u must not be larger than the numerical velocity $\frac{\Delta x}{\Delta t}$. This is called the Courant-Friedrich-Lewy (CFL) criterium with the corresponding Courant number α .

The flux form of equation (3.7) is written as

$$\psi_i^{n+1} = \psi_i^n - \left[F(\psi_i^n, \psi_{i+1}^n, \alpha_{i+\frac{1}{2}}) - F(\psi_{i-1}^n, \psi_i^n, \alpha_{i-\frac{1}{2}}) \right]. \quad (3.8)$$

with the flux function F that is defined by:

$$F(\psi_L, \psi_R, \alpha) = \alpha^+ \psi_L + \alpha^- \psi_R$$

The integer indices refer to the cell centers while the half integer indices denote the cell walls.

Assuming $u = \text{const}$, $\psi \geq 0$ and expanding ψ about (x_j, t^n) , one can see that Equation (3.8) approximates rather the advection-diffusion equation

$$\frac{\partial \psi}{\partial t} = -\frac{\partial}{\partial x}(u\psi) + \frac{\partial}{\partial x} \left(K \frac{\partial \psi}{\partial x} \right), \quad (3.9)$$

$$K = \frac{\Delta x^2}{2\Delta t} (|\alpha| - \alpha^2) \quad (3.10)$$

with a diffusion coefficient K and a second order error. The error must be numerically

estimated and subtracted from Equation (3.8). The basic idea of MPDATA is to use a donor cell approximation to the error term. Herefore the error term is rewritten as

$$\text{error}^{(1)} = \frac{\partial}{\partial x}(v^{(1)}\psi)$$

where

$$v^{(1)} \equiv \frac{\Delta x^2}{2\Delta t}(|\alpha| - \alpha^2) \frac{1}{\psi} \frac{\partial \psi}{\partial x}$$

denotes a pseudo velocity. The superscript ⁽¹⁾ is a first approximation to the error. The diffusive flux in the second term of Equation (3.8) is now multiplied by unity:

$$\frac{1}{\psi} \frac{\partial \psi}{\partial x} \cdot \psi = \frac{1}{1} \frac{\partial \psi}{\partial x}$$

but in the donor cell approximation the factor in the denominator and numerator is approximated using a centered value and an upstream value, respectively. In this way a nonlinear higher-order approximation is found that is positiv definite. A first order estimate of the pseudo velocity is

$$V_{i+\frac{1}{2}}^{(1)} = (|\alpha| - \alpha^2) \frac{\psi_{i+1}^{(1)} - \psi_i^{(1)}}{\psi_{i+1}^{(1)} + \psi_i^{(1)}}.$$

After subtracting the the donor cell estimate of the error one gets:

$$\psi_i^{(2)} = \psi_i^{(1)} \left[F(\psi_i^{(1)}, \psi_{i+1}^{(1)}, V_{i+\frac{1}{2}}^{(1)}) - F(\psi_{i-1}^{(1)}, \psi_i^{(1)}, V_{i-\frac{1}{2}}^{(1)}) \right]$$

This is the basic MPDATA algorithm for the one-dimensional advection equation. For both an extension to more than one dimension and a curvilinear framework see Smolarkiewicz and Margolin (1998).

3.2.2 MPDATA as a Flow Solver

A generalised transport equation can be written as

$$\frac{\partial}{\partial t}(G\psi) + \nabla \cdot \mathbf{u}\psi = GR, \quad (3.11)$$

where $G = G(\mathbf{x})$ is the Jacobian, $\mathbf{u} = \mathbf{u}(\mathbf{x}, t) = G\dot{\mathbf{x}}$ denotes a generalised velocity vector and R combines all forcings and/or sources. A temporal discretisation of equation (3.11) has the form:

$$\frac{G\psi^{n+1} - G\psi^n}{\Delta t} + \nabla \cdot \left(\mathbf{u}^{n+\frac{1}{2}} \psi^n \right) = GR^{n+\frac{1}{2}} \quad (3.12)$$

For a second-order MPDATA scheme of (3.11) the procedure shown in Section 3.2.1 must be extended. As a result¹ the modified equation is given by:

$$\begin{aligned} \frac{\partial}{\partial t}(G\psi) + \nabla \cdot \mathbf{u}\psi &= GR - \nabla \cdot \left(\frac{\Delta t}{2} \frac{1}{G} \mathbf{u}(\mathbf{u} \cdot \nabla \psi) + \frac{\Delta t}{2} \frac{1}{G} \mathbf{u}\psi(\nabla \cdot \mathbf{u}) \right) \\ &+ \nabla \cdot \left(\frac{\Delta t}{2} \mathbf{u}R \right) + \mathcal{O}(\Delta t^2) \end{aligned} \quad (3.13)$$

The time levels $n + \frac{1}{2}$ of \mathbf{u} and R in equation (3.12) are required to eliminate $\mathcal{O}(\Delta t)$ truncation errors proportional to Δt in equation (3.13). The truncation errors on the RHS of (3.13) are either due to advection or else due to the forcing and its dependence on ψ . While the first one depends linearly on ψ the second one is in general unknown and often nonlinear.

For an inhomogeneous transport $R \neq 0$ the compensation of the $\mathcal{O}(\Delta t)$ truncation error proportional to the advective flow on the RHS of equation (3.13) is important to preserve both the global accuracy and the stability of forward-in-time approximations (3.12). Advection and forcing are linked by the term $\nabla \cdot \left(\frac{\Delta t}{2} \mathbf{u}R \right)$ and not treated separately as in many non-oscillatory algorithms.

Assuming, $R^{n+\frac{1}{2}}$ in equation (3.12) is approximated by $R^{n+\frac{1}{2}} = \frac{1}{2} \left(R^n + R^{n+\frac{1}{2}} \right)$, a fully second-order accurate MPDATA realisation can be written as:

$$\begin{aligned} \psi_i^{n+1} &= \text{MPDATA} \left(\tilde{\psi}, \mathbf{V}_i^{n+\frac{1}{2}}, G \right) + \frac{\Delta t}{2} R_i^{n+1} \\ \text{with} \quad \tilde{\psi} &= \psi^n + \frac{\Delta t}{2} R^n \end{aligned}$$

By integrating equations (3.1) - (3.5) using the MPDATA scheme, the quantities \mathbf{u} , θ and ϕ can be determined.

¹For a derivation see Smolarkiewicz and Margolin (1998).

3.3 Applications

Many numerical experiments have been performed using the fluid solver EULAG, e.g. the modelling of urban flows (Smolarkiewicz et al., 2007), oceanic currents (Warn-Varnas et al., 2007), solar convection (Ghizaru et al., 2010) or cloud physics (Grabowski, 2007; Spichtinger et al., 2009).

Several experiments deal with small-scale boundary-layer flows using the incompressible Boussinesq approximation and the IMB method. Smolarkiewicz et al. (2007) studied the contaminant dispersion around the Pentagon with a resolution of 1 m and 2 m in the vertical and horizontal, respectively. They wanted to quantify flow characteristics under different meteorological conditions and thereby compared terrain-following coordinates with the IMB method. Figure 3.1 shows an example for the high-resolved urban flow around the Pentagon.

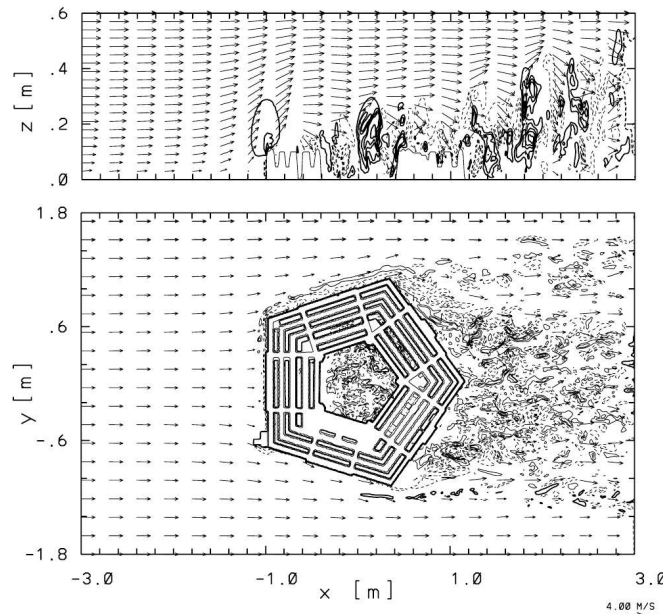


Figure 3.1: Flow above and around the Pentagon using EULAG. The vertical velocity field, superimposed by flow vectors, in the central vertical plane (above) and in the horizontal plane at the half height of the building (below) is shown. From Smolarkiewicz et al. (2007).

In analogy to a fluid flow in porous media Wyszogrodzki and Smolarkiewicz (2010) performed numerical simulations of boundary layer flows through Oklahoma City downtown area. They analysed the numerical results of random porous media to find a

relation between the momentum flux and the macroscopic pressure gradient. Furthermore, they investigated whether a porous-media analogy could be applied to parameterise urban effects in mesoscale models. The embedded structure of Oklahoma City used for the EULAG simulations (left) and a horizontal cross-section of the vertical velocity (right) are illustrated in Figure 3.2.

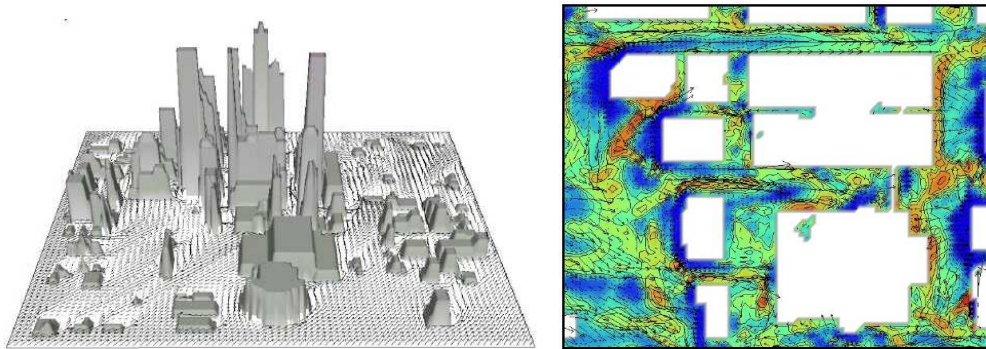


Figure 3.2: Embedded structure of the Oklahoma City area in the EULAG simulations (left) and a horizontal cross-section of both instantaneous vertical velocity and horizontal wind vectors at $z = 4$ m above the ground (right). From Wyszogrodzki and Smolarkiewicz (2010).

Schrötle and Dörnbrack (2012) studied the turbulent flow through a heterogeneous forest canopy by treating fractal Pythagoras trees in the computational domain numerically as immersed boundaries. The IMB approach allowed for a resolution from the scale of small branches up to the tree height. An investigation of the turbulent structure of the flow through diabatically heated trees for both neutral and stable stratification was performed. Figure 3.3 shows the potential temperature perturbation and vertical velocity for the flow under initially neutral background stratification with heated crowns.

Relevant for this PhD thesis is the Pentagon study. While Smolarkiewicz et al. (2007) examined neutral and stably stratified flows this study deals with neutral and convective boundary layer flows and, additionally, the dispersion of a passive scalar. The building is modelled with real dimensions whereas the Pentagon is scaled to 1:200 based on the sizes of the wind tunnel setup. Furthermore, in this thesis a combination of terrain-following coordinates and IMB method is used to deal with the Aare canyon and the building, respectively.

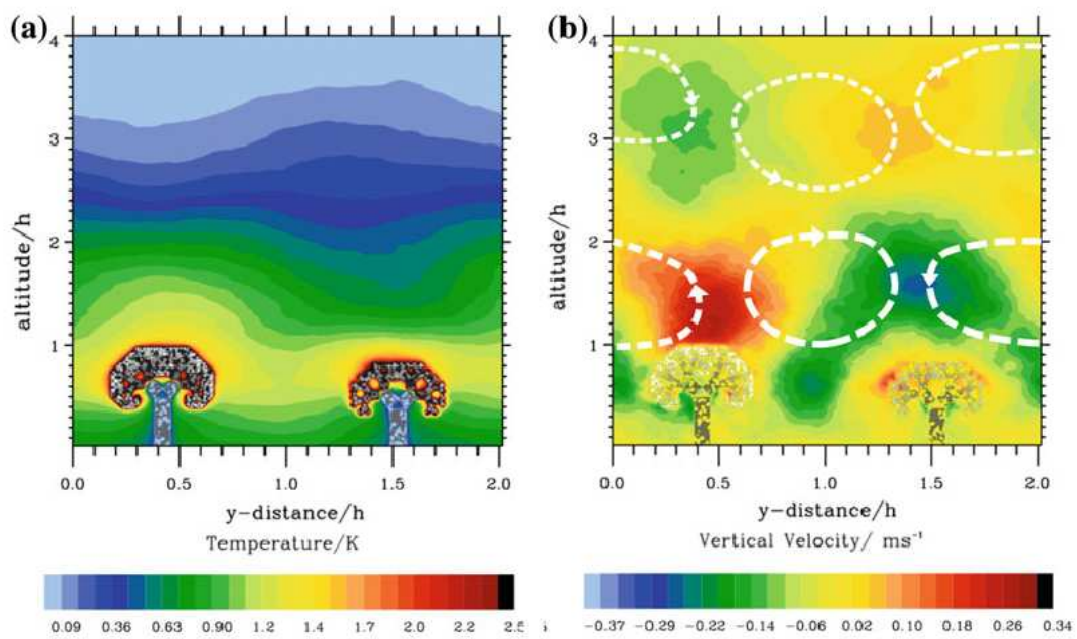


Figure 3.3: Flow through a forest canopy with heated crowns under initially neutral background stratification. The long-term averaged potential temperature perturbation (left) and the vertical velocity (right) as an $y-z$ slice are shown. From Schrötle and Dörnbrack (2012).

Chapter 4

Model Setups

In this chapter the different model setups containing topography, initial and boundary conditions are presented. The simulation procedure is briefly described. Two tables at the end list acronyms and symbols of all performed simulations and averaging procedures.

4.1 Horizontally Homogeneous and Inhomogeneous Flat Terrain

In the first setup the model domain is supposed to be flat with a homogeneous and an inhomogeneous surface roughness, respectively. These setups can be regarded as control cases and shall be compared with the simulation results of the more complex setups (Section 4.2 and Section 4.3).

4.1.1 Computational Setups

The computational domain has a size of $(L_x, L_y, L_z) = (766 \text{ m}, 126 \text{ m}, 200 \text{ m})$, resolved with $n = 384, m = 64, l = 101$ grid points using terrain-following coordinates (see Section 3.1). The inflow boundary is located in the west of the domain at $(x = -154 \text{ m}, y, z)$ because the point of origin $x_0 = 0 \text{ m}$ is set to the position where the tracer is released.

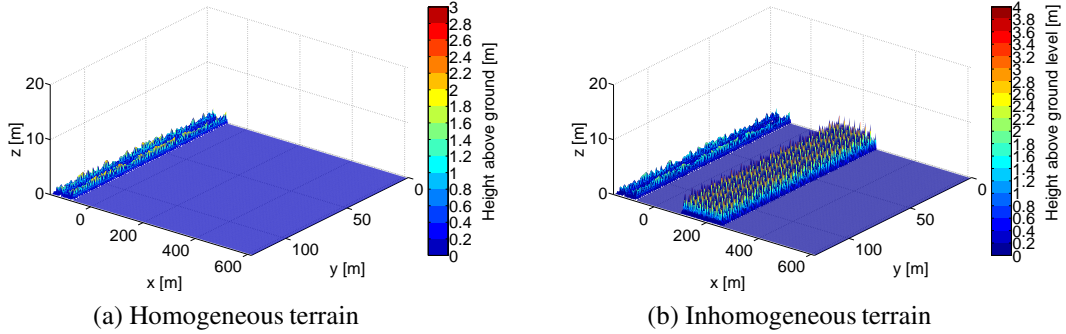


Figure 4.1: Setups for tracer dispersion over homogeneous (a) and inhomogeneous (b) terrain. z denotes the height above the ground.

Surface elevations within the inflow region between $x = 10$ m and $x = 80$ m lead to enhanced roughness for generating turbulence (Figure 4.1 (a)). The roughness elements consist of sine and cosine functions

$$z(x, y) = A [0.5 (\cos(\pi(x + rd)))y + 0.3 (\cos(0.8\pi(x + 1))) (\sin(0.5\pi(y + rd)))]$$

with an amplitude $A = 2.5$ m and random numbers rd . The random numbers are generated using a Gaussian distribution with a mean value $\mu = 0$ m and a standard deviation $\sigma = 1$ m. The inflow and the outflow region are not shown in the figures of the following chapters. Both cyclic and open boundary conditions are applied in the x - and in the y -direction while a rigid lid is assumed at the upper boundary. At the bottom of the domain a partial-slip condition allows for a subgrid-scale momentum transport in the vicinity of the lower boundary (see Section 2.4.1). The effect of surface friction in Equation (3.2) is modelled by means of a drag coefficient C_D where the surface stress is defined as $\tau_{ij}^0 = C_D |u_{ij}^0| u_{ij}^0$ with u_{ij}^0 being the near surface flow velocity.

Two different computational setups are chosen. The first setup consists of a homogeneous flat terrain while the second setup is extended by a roughness area of 150 m width in the x -direction. In the following this terrain inhomogeneity is also called as "roughness elements" or "roughness area". It consists of sine waves without a random noise and is located where the river Aare flows in later simulations (Figure 4.1 (b)). The amplitude is $A = 5.5$ m. Six different simulations are performed. At first, cyclic and open boundary conditions without a surface heat flux are applied in both computational domains. The subsequent simulations consist of cyclic boundary conditions in

the x - and in the y -direction and, additionally, a surface heat flux Q_{hf} .

Initial conditions for the velocity components are $(u, v, w) = (5 \frac{\text{m}}{\text{s}}, 0, 0)$. The Boussinesq reference state is $\theta_b = 300$ K and potential temperature fluctuations θ' are set to zero. Convection is driven by a constant surface heat flux $Q_{\text{hf}} = H_0 = 0.06 \text{ Kms}^{-1}$ distributed in the lowest grid cell through the subgrid-scale fluxes (see Section 2.4.1). For the use of cyclic boundary conditions a constant mass flux is acquired by calculating the mean streamwise velocity $\langle u \rangle_{yz}$ over each $y - z$ plane. A pressure gradient in the x -direction is determined at each time step Δt by the difference of $\langle u \rangle_{yz}$ to the inflow velocity u divided by Δt . This auxiliary forcing $\frac{u - \langle u \rangle_{yz}}{\Delta t}$ is added at each grid point.

4.1.2 Simulation Strategy

By performing an auxiliary simulation using the homogeneous setup, fully developed wind and temperature profiles are achieved. A time step $\Delta t = 0.1$ s is used to get a Courant number $\alpha < 1$. With $nt = 18000$ integration steps this leads to a simulation time of 30 minutes. After a restart a tracer is continuously released from a point source in a three-dimensional grid cell with an emission rate of $Q = 50 \text{ s}^{-1}$. The surface heat flux Q_{hf} is applied in both the auxiliary simulations and after the restart.

Over a flat terrain the simulation after the restart is stopped after 100 s when the tracer reaches the domain boundary. The source is located at $x = x_r = 0$ m, $y = y_r = \frac{ny \cdot \Delta y}{2}$ and at three different release heights: $z_r = 52$ m and $z_r = 32$ m and $z_r = 12$ m.

Table 4.1 summarises the simulation parameters.

4.2 Simulations in an Idealised Aare Valley

The next setup is a simplified version of the Aare river that flows between the western and the eastern part of the PSI. Flow evolution and tracer dispersion of this more complex setup, as well as the differences to the flow and dispersion over a flat homogeneous and inhomogeneous terrain (Section 4.1.1), are studied.

Geometrical parameters	Initial conditions
$\Delta x = 2$ m	$u = 5$ ms ⁻¹
$\Delta y = 2$ m	$v = w = 0$ ms ⁻¹
$\Delta z = 2$ m	$\theta_b = 300$ K
$nx = 384$	$\theta' = 0$ K
$ny = 64$	$C_D = 0.001$
$nz = 101$	Q_{hf} (see Table 4.4)
$\Delta t = 0.1$ s	
$nt = 1000$	

Table 4.1: Δx , Δy , Δz denote the mesh spacing, nx , ny and nz the number of grid points in the x -, y - and z -direction, respectively. Δt is the time step and nt refers to the iteration steps. u , v and w are the velocity components in the respective x -, y - and z -direction directions. θ_b is the Boussinesq reference state, θ' symbolises the potential temperature fluctuations, C_D the drag coefficient and Q_{hf} the surface heat flux.

4.2.1 Computational Setup

The setup consists of three different ground levels with $z_h = 0$ m corresponding to the river Aare in the middle of the domain. The height of the terrain is $z_h = 22$ m and $z_h = 8$ m in the west and in the east of the river, respectively (Figure 4.3). The Aare is represented as a straight river along the y -direction with a width of 150 m. A filter function for smoothing the surface is used to avoid points of discontinuity.

Because of the cyclic boundary conditions an artificial hill with a small slope in the outflow region levels the different terrain heights. This leads to an extension of the domain in the x -direction compared to the setups over a flat terrain.

4.2.2 Tracer Dispersion

The locations x_r and y_r of the point source are the same as in Section 4.1.2, but the release heights z_r change because the ground level $z = 22$ m in the west of the Aare must be added to make the experiments comparable to those over a flat terrain. As the mesh in the vertical direction is not equidistant due to the terrain-following coordinates, the three release heights are $z_r = 73.74$ m, $z_r = 54.55$ m and $z_r = 34.35$ m. The domain is extended in the x -direction and the simulation is stopped after 200 s. Table 4.2 shows the simulation parameters.

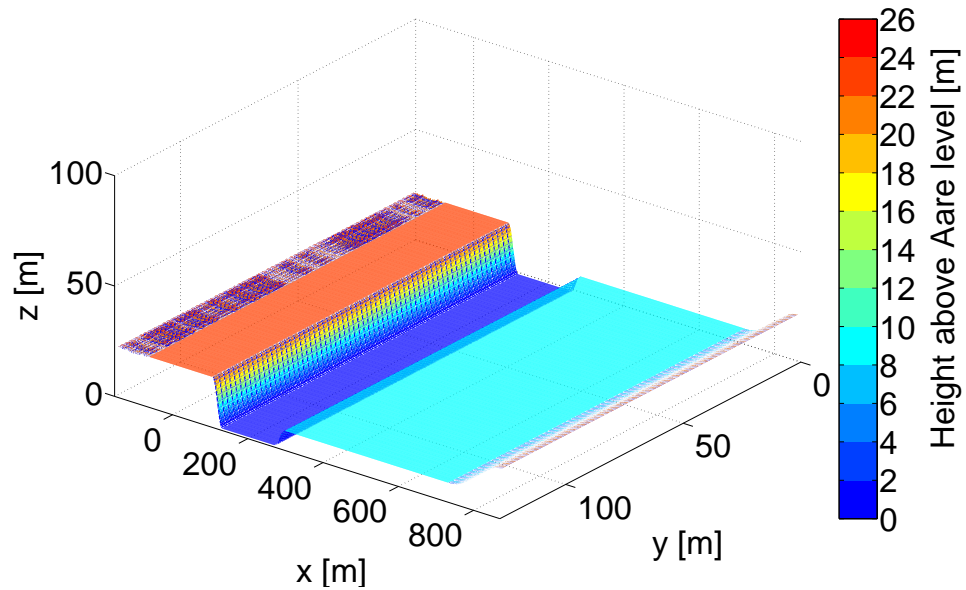


Figure 4.2: Setup for the tracer dispersion with an idealised Aare valley.

Geometrical parameters	Initial conditions
$\Delta x = 2 \text{ m}$	$u = 5 \text{ ms}^{-1}$
$\Delta y = 2 \text{ m}$	$v = w = 0 \text{ ms}^{-1}$
$\Delta z = 2 \text{ m}$	$\theta = 300 \text{ K}$
$n_x = 512$	$\theta' = 0 \text{ K}$
$n_y = 64$	$C_D = 0.001$
$n_z = 101$	Q_{hf} (see Table 4.4)
$\Delta t = 0.1 \text{ s}$	
$nt = 2000$	

Table 4.2: Same as Table 4.1 but with a different number of grid points and iteration steps.

4.3 Simulations in an Idealised Aare Valley including a Building

The idealised Aare valley setup (Figure 4.3) is extended by an obstacle that represents the building Experimentierhalle PSI West and the source Zentrale Fortluftanlage PSI West (ZFA), where the emissions occur. The building consists of a cuboid and a stack at the northern wall of the building, numerically modelled by the IMB method (see Section 3.1). Its influence on flow and dispersion shall be investigated.

4.3.1 Computational Setup

For this setup the same topography as described in Section 4.2.1 is used except for the number of grid points n_x and n_y because the distance of the building to the inflow area and the lateral boundaries shall be increased. The building has a size of $60\text{ m} \times 150\text{ m} \times 20\text{ m}$ while the stack size is $2\text{ m} \times 2\text{ m} \times 12\text{ m}$ in the x -, y - and z -direction, respectively (Figure 4.3). Building and stack are modelled using the IMB approach and they are not heated under convective conditions. Due to the terrain following coordinates the stack height is $z = 54.04\text{ m}$: 22 m terrain height + 20 m building height + 12 m stack height. The release occurs one grid cell above, at $z_r = 55.82\text{ m}$ above the Aare ($z = 0\text{ m}$). Cyclic boundary conditions are used in the x -direction, open boundary conditions at the lateral boundaries.

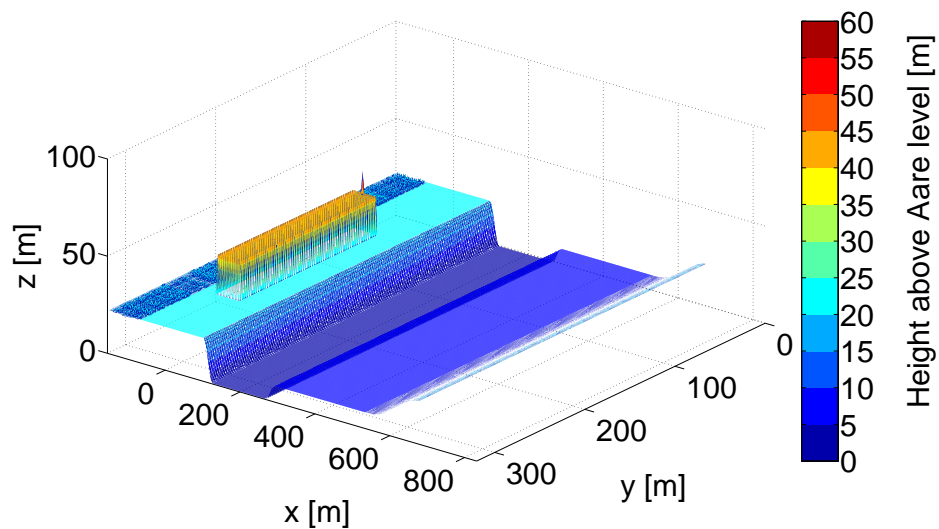


Figure 4.3: Setup for the tracer dispersion with an idealised Aare valley including a building representing the ZFA PSI West. The stack is not considered in the simulations.

4.3.2 Tracer Dispersion

In contrast to the first two setups only one release height at $z_r = 55.82\text{ m}$ for the tracer emission is considered. The simulation is stopped after 200 s . Table 4.3 shows the simulation parameters.

Geometrical parameters	Initial conditions
$\Delta x = 2$ m	$u = 5$ ms ⁻¹
$\Delta y = 2$ m	$v = w = 0$ ms ⁻¹
$\Delta z = 2$ m	$\theta = 300$ K
$nx = 416$	$\theta' = 0$ K
$ny = 160$	$C_D = 0.001$
$nz = 101$	Q_{hf} (see Table 4.4)
$\Delta t = 0.1$ s	
$nt = 2000$	

Table 4.3: Same as in Table 4.1 but with a different number of grid points.

4.4 Acronyms and Symbols

Different boundary conditions, initial conditions and terrain shapes are used for the EULAG simulations. Table 4.4 gives the acronyms of each simulation that are written in the captions of the following chapters. Only the initial condition parameters that vary between the simulations are listed.

Cases	Boundary cond.		Terrain	Surface heat flux Q_{hf}
	x	y		
Fc	cyclic	cyclic	homogeneous	0 Kms ⁻¹
Fo	open	open	homogeneous	0 Kms ⁻¹
FRc	cyclic	cyclic	inhomogeneous	0 Kms ⁻¹
FRo	open	open	inhomogeneous	0 Kms ⁻¹
FHc	cyclic	cyclic	homogeneous	0.06 Kms ⁻¹
FHRc	cyclic	cyclic	inhomogeneous	0.06 Kms ⁻¹
T1	cyclic	cyclic	Aare valley	0 Kms ⁻¹
TH1	cyclic	cyclic	Aare valley	0.06 Kms ⁻¹
TH2	cyclic	cyclic	Aare valley	0.6 Kms ⁻¹
Z	cyclic	open	Aare valley + building	0 Kms ⁻¹
ZH	cyclic	open	Aare valley + building	0.06 Kms ⁻¹

Table 4.4: Acronyms for the different setups specified by the boundary conditions, the terrain shape and the surface heat flux.

Different averaging procedures depending on the setups are used. A horizontal average $\langle \rangle_{xy}$ as a vertical profile

$$\langle \psi \rangle_{xy}(z, t) = \frac{1}{nx \cdot ny} \sum_{i=78}^{nx-84} \sum_{j=1}^{ny} \psi_{ij}$$

without considering the inflow and the outflow region is only calculated for the flow over a flat terrain. ψ represents any quantity. The lateral average $\langle \rangle_y$ is defined as

$$\langle \psi \rangle_y(x, z, t) = \frac{1}{ny} \sum_{j=1}^{ny} \psi_j.$$

Unless otherwise specified, the temporal average is calculated using an online statistical evaluation (Fröhlich, 2006). $\langle \rangle_t$ is determined at each grid point and new time t^{n+1} as follows:

$$\begin{aligned} \langle \psi \rangle_t^{n+1} &= \varepsilon \psi^{n+1} + (1 - \varepsilon) \langle \psi \rangle_t^n \\ \langle \psi' \phi' \rangle_t^{n+1} &= \varepsilon (\psi^{n+1} - \langle \psi \rangle_t^{n+1}) (\phi^{n+1} - \langle \phi \rangle_t^{n+1}) + (1 - \varepsilon) \langle \psi' \phi' \rangle_t^n \end{aligned}$$

$\psi, \phi = u, v, q, \theta$ and $\varepsilon = \Delta t / t^n - t^{\text{start}}$ where t^n denotes the time of the n th time step and $t^{\text{start}} = 6000$ s hence the data are averaged over 20 min within the auxiliary simulations.

The notation of the averaging procedures is summarised in Table 4.5.

Averaging procedure	Description
$\langle \rangle_t$	Temporally averaged quantity
$\langle \rangle_y$	Averaged quantity in lateral direction
$\langle \rangle_{yt}$	Laterally and temporally averaged quantity
$\langle \rangle_{xy}$	Horizontally averaged quantity
$\langle \rangle_{xyt}$	Horizontally and temporally averaged quantity
$\langle a' b' \rangle$	a' and b' are the fluctuating parts of the temporally averaged quantities $\langle a \rangle_t$ and $\langle b \rangle_t$

Table 4.5: Notation of averaging procedures used in the next chapters.

The following terms are used synonymously in the following chapters:

- y-direction, spanwise, across-flow, lateral direction

- x -direction, streamwise, along-flow

Chapter 5

Tracer Dispersion over Horizontally Homogeneous and Inhomogeneous Flat Terrain

The dispersion of a passive scalar over a flat area shall be investigated. First, a homogeneous terrain is chosen. Second, additional roughness elements are included (Figure 4.1 (b)). A tracer release at $z_r = 52$ m, $z_r = 32$ m and $z_r = 12$ m under convective and non-convective vertical conditions is studied, applying both cyclic and open boundaries. The following questions are to be answered:

- Do the roughness elements influence the atmospheric flow and the tracer dispersion?
- What is the difference between the use of open and cyclic boundary conditions?
- Does the additional heat flux affect the tracer dispersion?
- How does the source height influence the tracer dispersion?

5.1 Moderate Wind Speed without Thermal Convection

5.1.1 Velocity and Temperature Profiles

As described in Chapter 4 an auxiliary simulation is performed for both open and cyclic boundary conditions to get fully developed wind and temperature profiles. Figure 5.1 shows the contour lines of the horizontal and vertical velocities u and w after 30 min simulation time as well as the temporally and laterally averaged velocity component $\langle u \rangle_{yt}$. Using cyclic boundary conditions there is an iterated transition from a

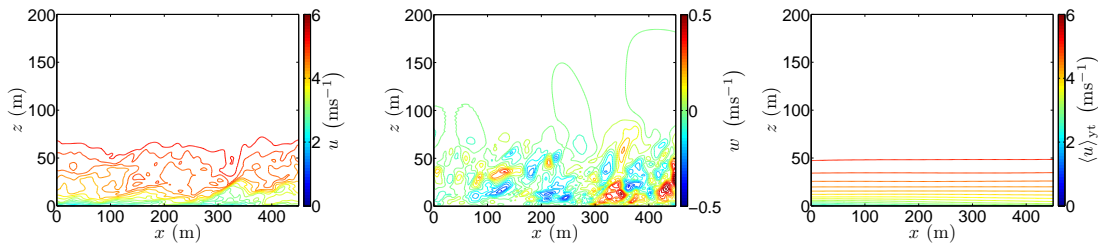


Figure 5.1: [F_c] Contours of longitudinal velocity u (left), vertical velocity w (middle) and temporally and laterally averaged longitudinal velocity $\langle u \rangle_{yt}$ (right). The $x - z$ cross section for u and w is taken at $y = \frac{ny \cdot \Delta y}{2}$ and $t = 18000$ s.

smooth to a rough surface that leads to small disturbances in all directions. The additional movements lead to an intensive mixing of the atmospheric flow in the lowest 50 m. In comparison, a turbulent boundary layer does not evolve when open boundary conditions are applied (Figure 5.2).

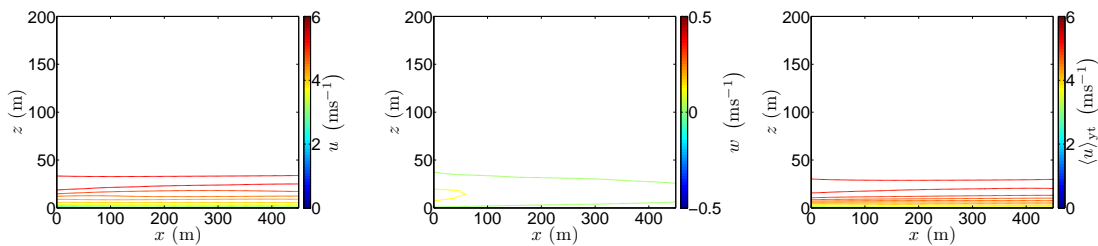


Figure 5.2: [F_o] Same as 5.1, but for open boundary conditions.

Figure 5.3 shows the logarithmic vertical profiles $\langle u \rangle_{xyt}$ for both cyclic and open boundary conditions. Due to the equidistant grid size a perfectly logarithmic wind profile, typical for a neutral boundary layer, does not evolve close to the ground. For $z \lesssim 50$ m and $z \lesssim 20$ m a boundary layer forms using cyclic and open boundaries, respectively. In the latter case $\langle u \rangle_{xyt}$ reaches a maximum at $z \approx 20$ m, which can be interpreted as a low-level jet.

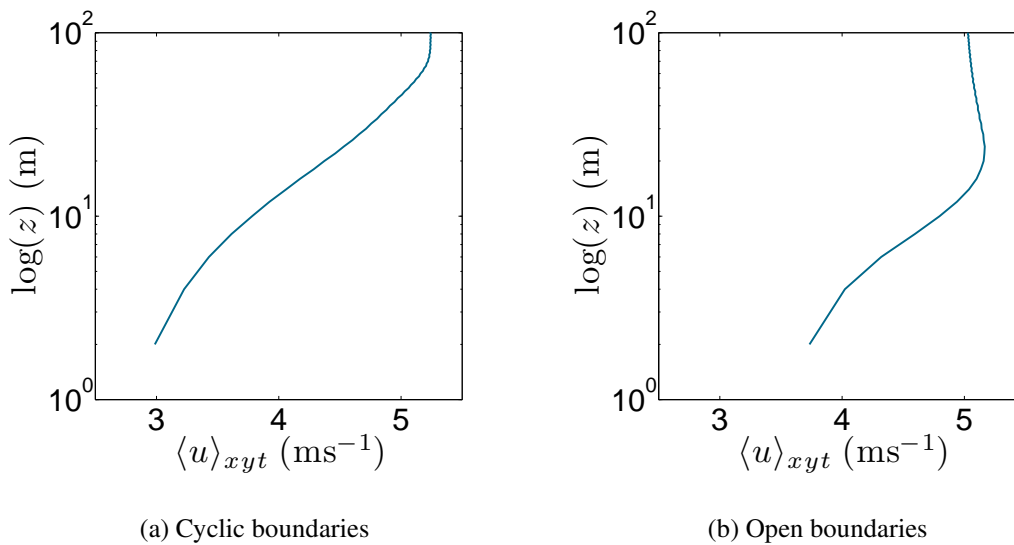


Figure 5.3: [F_c,F_o] Horizontally and temporally averaged vertical profiles of the streamwise velocity $\langle u \rangle_{xyt}$ for cyclic (left) and open (right) boundary conditions.

In the following the setups are referred to as turbulent and laminar boundary layer.

5.1.2 Tracer Release over Horizontally Homogeneous Terrain

A passive tracer is released at the three heights $z_r = 52$ m, $z_r = 32$ m and $z_r = 12$ m and the characteristics of the plume dispersion are discussed.

5.1.2.1 Temporal Development

Figure 5.4 shows the temporal development of the plume for the release height at $z_r = 32$ m and the turbulent setup F_c. This height is chosen because the stack height of

the ZFA, which is used in later simulations, is approximately $z_{st} = 32$ m above ground. Turbulence leads to a meandering of the plume and increasing vertical dispersion with distance from the source. As a consequence the concentration is not homogeneously distributed.

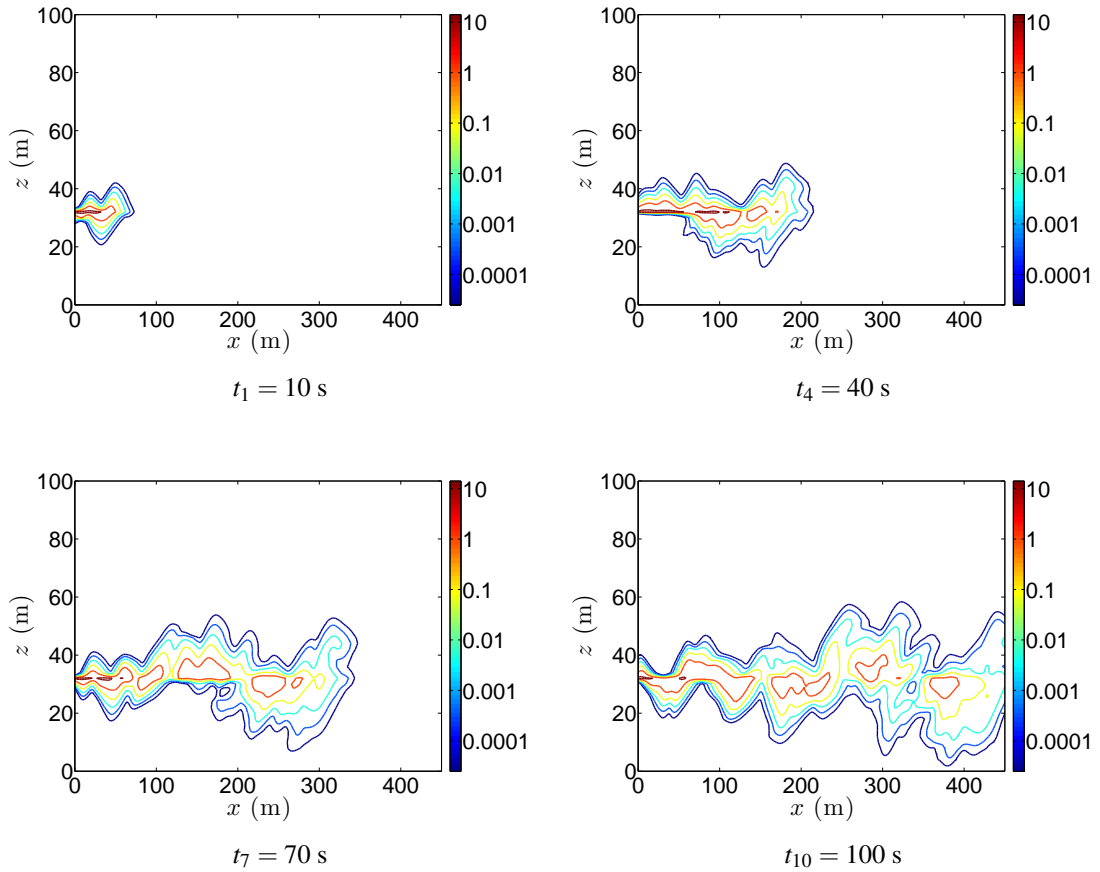


Figure 5.4: [Fc] Dimensionless concentration contours in the $x-z$ plane showing the temporal development of the plume. The cross section is taken at $y = \frac{ny \cdot \Delta y}{2}$.

To determine the speed of dispersion u_{plume} the integral of the concentration C in the $y-z$ planes is computed as a function of x and for discrete timesteps t_i :

$$I(x, t_i) = \sum_{j=0}^{ny-1} \sum_{k=0}^{nz-1} \frac{C_{jk}(x, t_i)}{ny \cdot nz} \quad i = 0, \dots, 10$$

For each t_i the coordinate x_{HM} is calculated, where

$$I_{\text{HM}}(x_{\text{HM}}, t_i) = \frac{I_0(x_0, t_i)}{2} \quad i = 0, \dots, 10$$

with
$$I_0(x_0, t_i) = I(x = 0, t_i)$$

holds. At (x_{HM}, t_i) the function $I(x, t_i)$ reduces to the half of the concentration at the source point $I_0(x_0, t_i)$. Figure 5.5 shows the result for $z_r = 32$ m and the same timesteps t_i as in Figure 5.4.

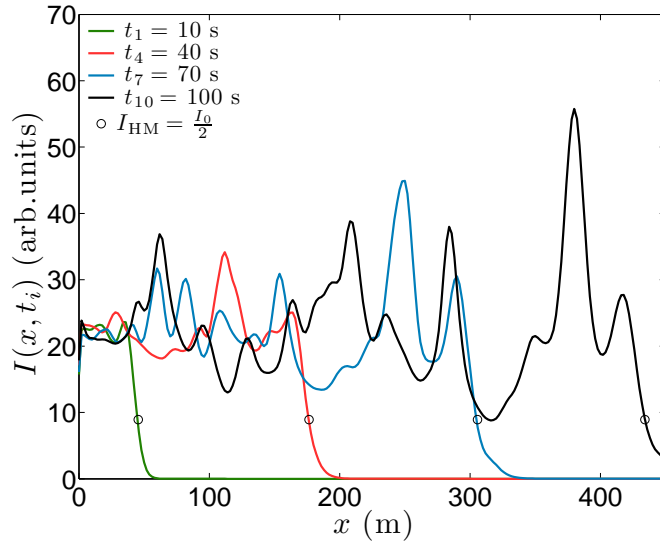


Figure 5.5: **[Fc]** Integrated concentration $I(x, t_i)$ in the $y-z$ planes as a function of x for the timesteps t_i . The points denote the locations x_{HM} where $I(x, t_i)$ reduces to the half of the concentration at the source.

Plotting x_{HM} against t gives the speed of dispersion by the gradient of the fit function (Figure 5.6). For the discussed case it is $u_{\text{plume}} = 4.33 \text{ ms}^{-1}$.

5.1.2.2 Influence of the Release Height

The influence of the tracer release height on the plume shape in the $x-z$ and $x-y$ planes is shown in Figure 5.7 (a) and Figure 5.7 (b), respectively. The closer the source to the ground the higher the influence of the turbulence on both the vertical and

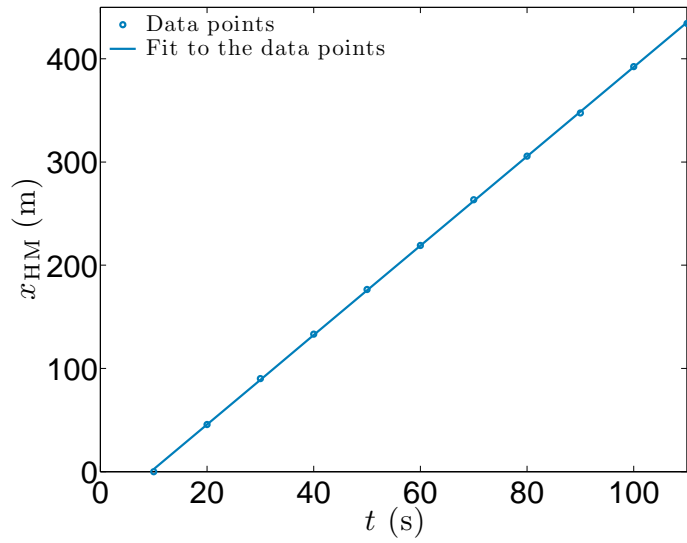


Figure 5.6: [Fc] x_{HM} at each timestep t_i . The gradient of the fit gives the plume speed $u_{\text{plume}} = 4.33 \text{ ms}^{-1}$.

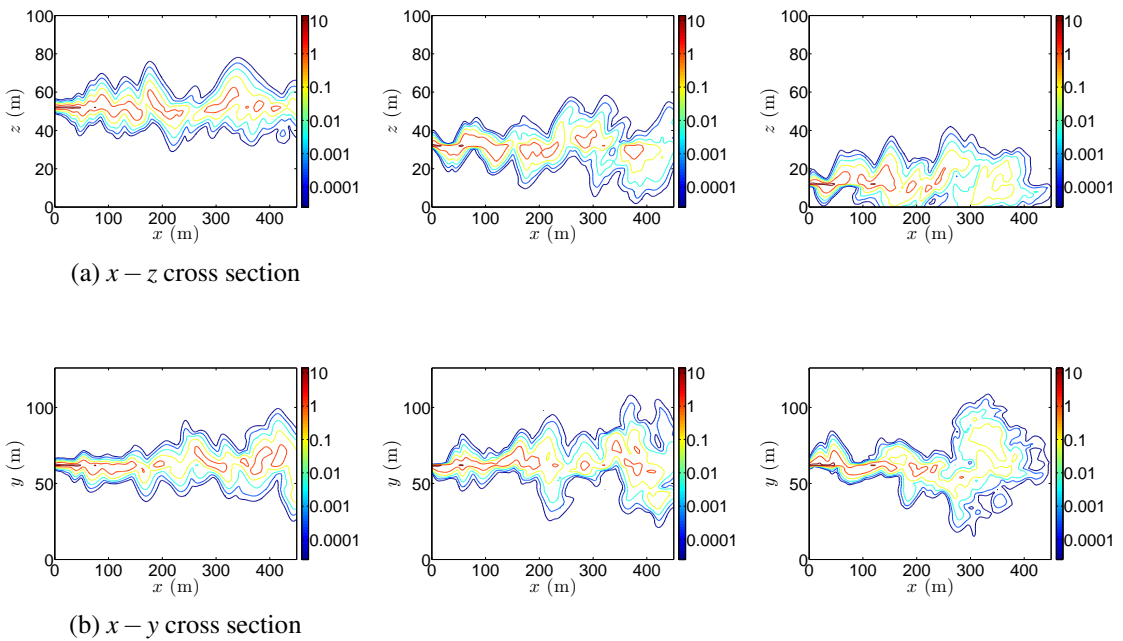


Figure 5.7: [Fc] Dimensionless concentration contours in the $x-z$ plane (a) and $x-y$ plane at heights $z_r = 52 \text{ m}$ (left), $z_r = 32 \text{ m}$ (middle) and $z_r = 12 \text{ m}$ (right). The cross sections are taken at $y = \frac{ny-\Delta y}{2}$ (a), the three release heights z_r (b) and $t = 100 \text{ s}$.

the horizontal dispersion. Each plume shows a horizontal and vertical widening in the streamwise direction.

Depending on z_r , time t and distance from the source x at which the tracer reaches the pedestrian height $z_p = 2$ m, the concentration $C(x, z_p, t)$ averaged over the y -direction shall be determined. For a specified threshold concentration $C_{th} = 0.0001$ which corresponds to 0.0002% of the emission rate Q , the distance from the source x where

$$C(x, z_p, t) > C_{th}$$

is identified and plotted as a function of t (Figure 5.8). The plume does not hit the

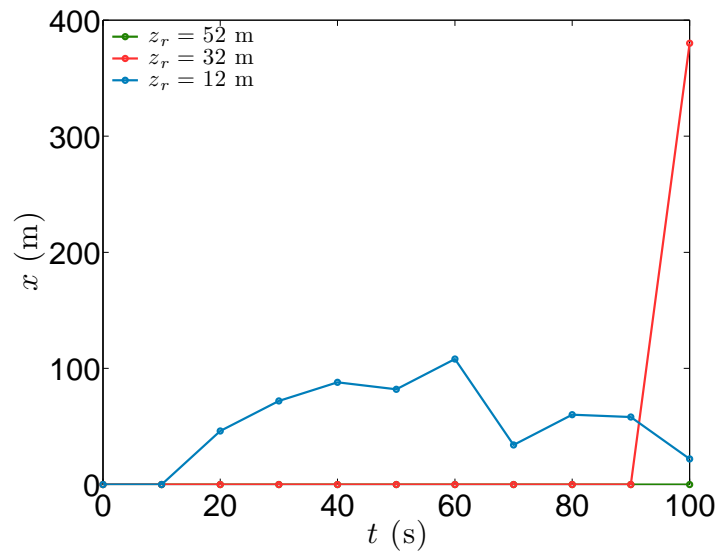


Figure 5.8: [Fc] Distance from the source x where the concentration C at the pedestrian height z_p is larger than the threshold C_{th} . The results are shown for the different release heights z_r and timesteps t .

ground when the tracer is released at $z_r = 52$ m. For $z_r = 12$ m the plume begins to reach the surface at $x = 46$ m and $t = 20$ s after the release. When the source is located at $z_r = 32$ m the concentration exceeds C_{th} at $x = 380$ m after $t = 100$ s. Thus the lower z_r , the closer to the source the tracer hits z_p and the smaller the time until reaching z_p .

5.1.2.3 Concentration Distribution

The concentration contours and corresponding vertical profiles at three different x -locations are shown in Figure 5.9 and 5.10 for cyclic and open boundary conditions. The plots show the plume at $t = 100$ s after the release, averaged in the y -direction.

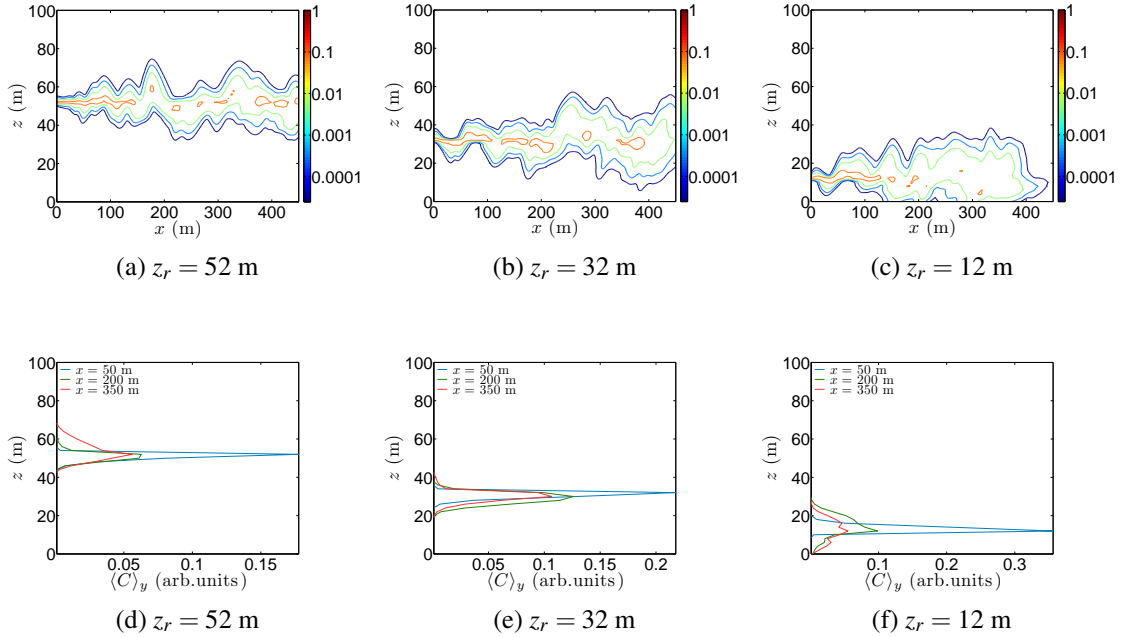


Figure 5.9: [Fc] Dimensionless laterally averaged concentration contours with a release at (a) 52 m, (b) 32 m, (c) 12 m and related vertical profiles (d)-(f). The vertical profiles are taken 50 m (blue), 200 m (green) and 350 m (red) downwind the source at $t = 100$ s. Cyclic boundary conditions are used.

In the turbulent boundary layer there is a vertical plume spread with increasing distance to the source. The tracer only reaches the ground when it is released at $z_r = 12$ m, which leads to a slower horizontal transport because of the reduced wind speed at the surface (see Figure 5.3 (a)). Compared to the non-averaged contour plots (Figure 5.7) the maximum mean concentration is lower¹ because the tracer concentration decreases in the spanwise direction with increasing distance from the source plane $y = \frac{ny \cdot \Delta y}{2}$ (Figure 5.7 (b)).

Under laminar conditions the plume spreads slowly in the vertical at the release heights $z_r = 52$ m and $z_r = 32$ m. The maximum mean concentration remains almost at the

¹Please note the different colour bars.

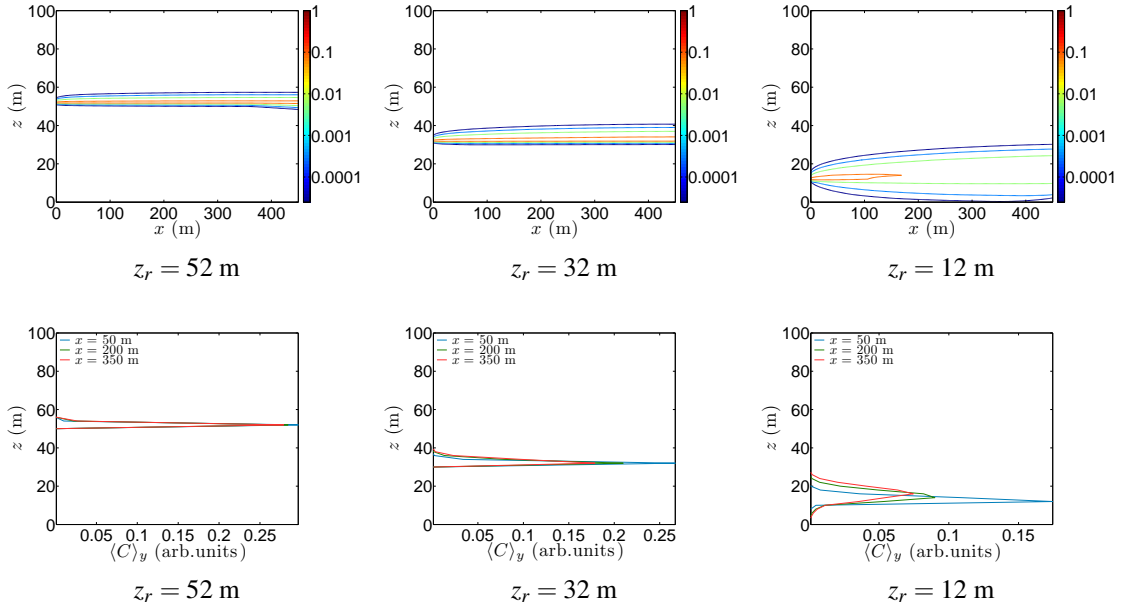


Figure 5.10: [Fo] Same as Figure 5.9 but for open boundary conditions.

source height because the wind speed is constant for $z \gtrsim 20$ m (see Figure 5.3 (b)). For $z_r = 12$ m the mean concentration drifts upwards and the plume widens with further distance from the source, so that it can reach the ground at $x \gtrsim 270$ m.

5.1.3 Tracer Release over Horizontally Inhomogeneous Terrain

As a next step the tracer is released over the horizontally inhomogeneous terrain. Figure 5.11 shows the acceleration of $\langle u \rangle_y$ behind the rough-to-smooth transition between $z = 0$ m and $z \approx 11$ m. This acceleration is the higher the larger the fetch². The air above 20 m is not influenced by the surface transition.

Figure 5.12 shows the tracer dispersion. Under turbulent conditions the concentration contours are the same as the contours over a homogeneous terrain (Figure 5.9) until the tracer reaches the roughness elements at $x = 106$ m. Above the roughness elements and further downstream, the plume widens which leads to a lower maximum mean concentration. The tracer reaches the ground when released at $z_r = 32$ m due to the increased turbulence.

²The distance from a surface change in downwind direction is called fetch.

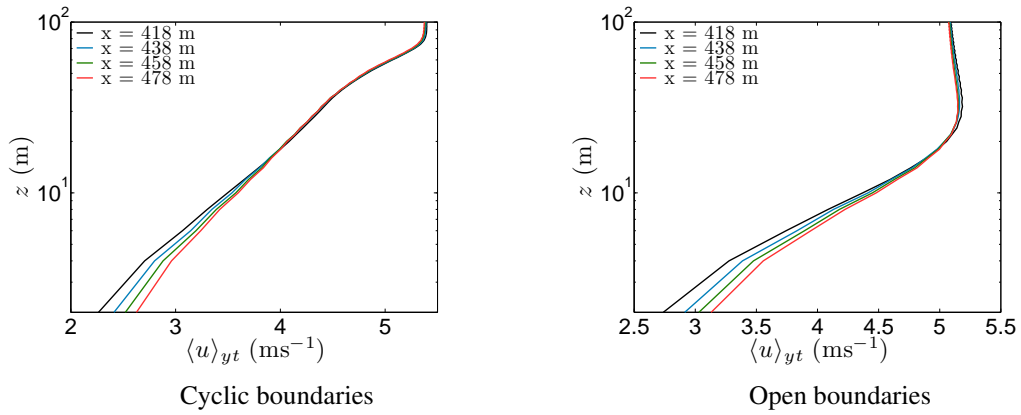


Figure 5.11: [FRc,FRo] Change of wind profiles downwind of rough-to-smooth transition. Values are taken 10 m (black), 20 m (blue), 30 m (green) and 40 m (red) behind the roughness change.

The same systematic behaviour can be found for laminar conditions (Figure 5.13). Compared to turbulent conditions the tracer concentration decreases more slowly because of the smaller vertical dispersion.

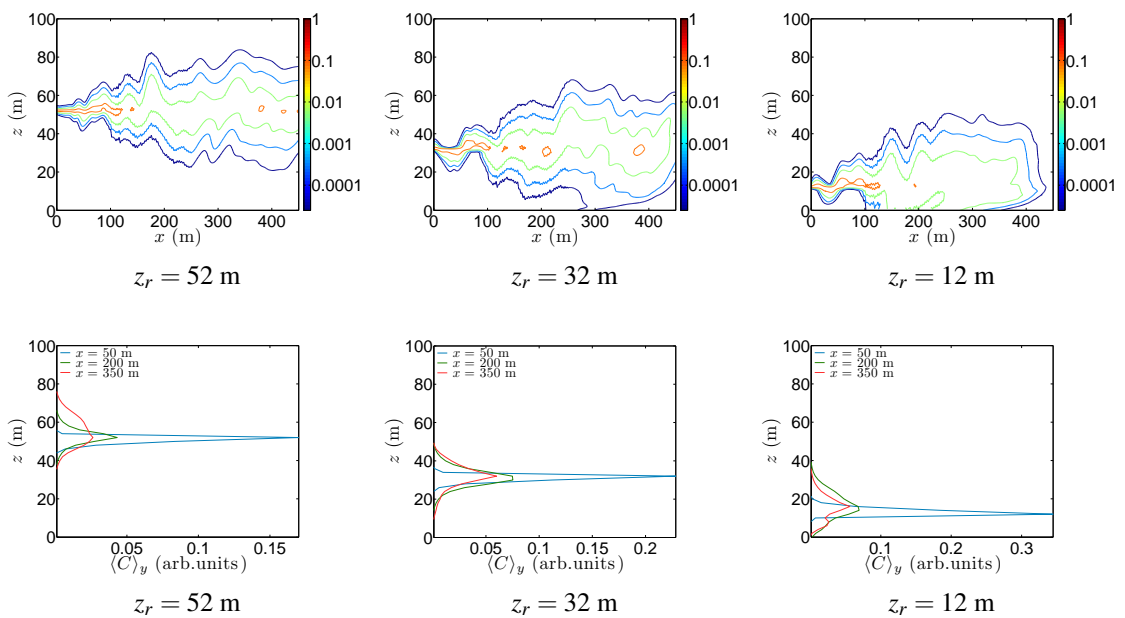


Figure 5.12: [FRc] Same as Figure 5.9 but with additional roughness elements.

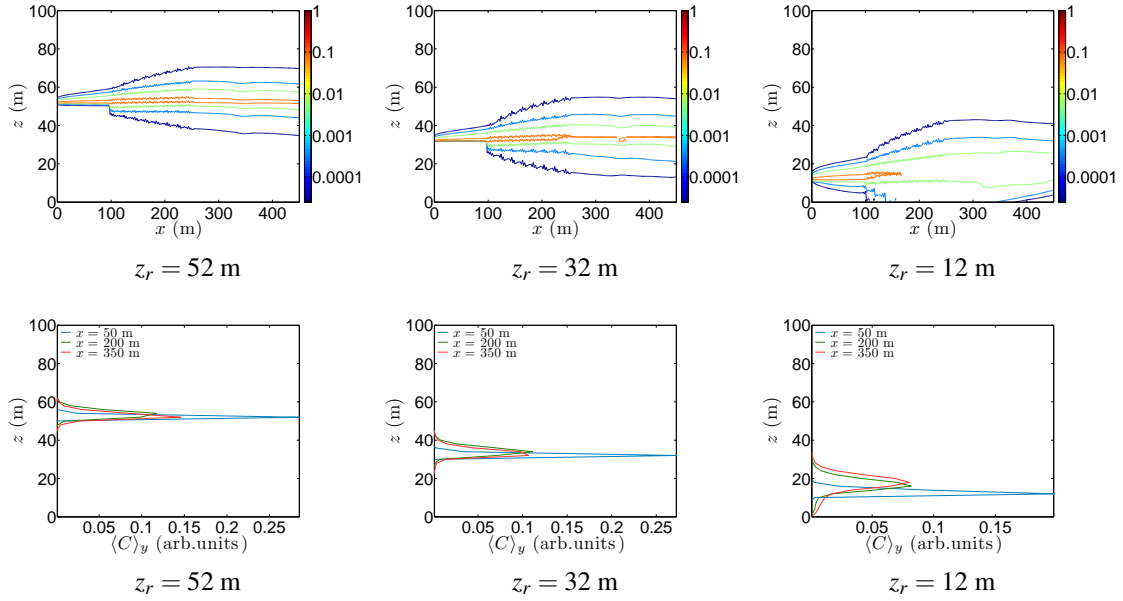


Figure 5.13: [FRo] Same as Figure 5.9 but with additional roughness elements and open boundary conditions.

5.1.3.1 Influence of Release Height and Surface Shape

To determine the time t_{th} until the tracer hits $z_p = 2$ m, the distance x to the source is identified as described in Section 5.1.2.2. t_{th} is defined as

$$t_{\text{th}} = t(x > 0) \quad \text{for } C(x, z_p, t) > C_{\text{th}} \text{ at } z = z_p.$$

In Figure 5.14 (a) z_r is plotted vs. t_{th} . Figure 5.14 (b) shows the smallest distance x_{dist} from the source where the tracer reaches z_p . It is defined as:

$$x_{\text{dist}} = \min(x) \quad \text{for } x > 0 \wedge C(x, z_p, t) > C_{\text{th}} \text{ at } z = z_p.$$

When the tracer is released at $z_r = 52$ m the tracer concentration never exceeds C_{th} at z_p within the domain boundaries. The surface inhomogeneity leads to a higher turbulent mixing that has an influence when $z_r \leq 32$ m. For a release height $z_r = 32$ m, t_{th} and x_{dist} are twice as large over a homogeneous surface. For $z_r = 12$ m there is no difference in the turbulent cases but for laminar conditions the tracer only hits the ground over an inhomogeneous terrain.

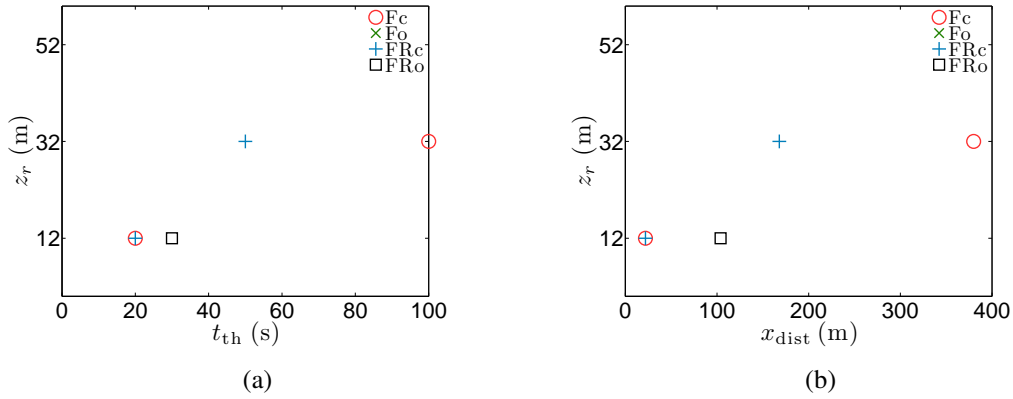


Figure 5.14: [**Fc,FRc,Fo,FRo**] Time t_{th} (a) and distance from the source x_{dist} (b) until the tracer hits z_p depending on z_r .

5.1.3.2 Concentration Distribution

Figure 5.15 shows the maximum mean concentration $\max(\langle C \rangle_l)$ at $x = 50$ m, $x = 200$ m, $x = 350$ m for the different case studies. It decreases with increasing distance to the source, except for the laminar case FRo. $\max(\langle C \rangle_l)$ rises again for $x > 200$ m ($z_r = 52$ m) or remains nearly constant ($z_r = 32$ m and $z_r = 12$ m). This behaviour can be explained as follows: When the plume reaches the roughness elements it widens vertically and the advective transport decelerates. This leads to a local rise of $\max(\langle C \rangle_l)$ travelling further downstream. It decreases for smaller timesteps until $t = 80$ s (not shown). At $t = 100$ s the local maximum is reached at $x = 350$ m and $\max(\langle C \rangle_l)$ is therefore larger than the value at $x = 200$ m.

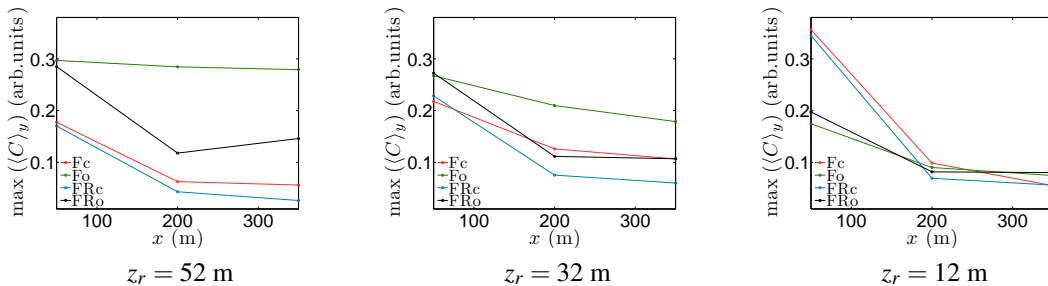


Figure 5.15: [**Fc,FRc,Fo,FRo**] Maximum mean concentration $\max(\langle C \rangle_l)$ at $x = 50$ m, $x = 200$ m, $x = 350$ m for the different case studies and release heights z_r .

5.1.4 Conclusions

Using cyclic boundary conditions a well-mixed turbulent boundary layer forms, while a laminar boundary layer is reached using open boundary conditions. A surface inhomogeneity due to roughness elements leads to a velocity change close to the surface. Above the roughness area and further downstream the vertical plume spread is larger than the vertical spread over a homogeneous surface. The pollutants reach the surface faster and closer to the source both above an inhomogeneous surface and with decreasing release height.

5.2 Moderate Wind Speed including Thermal Convection

In the following, the turbulent flow and the tracer distribution under neutral atmospheric stratification are compared with the atmospheric flow and tracer dispersion over a heated surface.

5.2.1 Velocity and Temperature Profiles

Figure 5.16 shows a snapshot of w and the contours of $\langle w \rangle_y$ at $t = 18000$ s. The surface heat flux causes free convection, consisting of thermals of warm air rising from the ground and cold air sinking due to buoyancy forces. The instantaneous $x - z$ cross section of w shows eddies of different sizes, the small of which disappear when w is averaged in the y -direction. Vertical profiles of $\langle \theta \rangle_{xyt}$ and $\langle u \rangle_{xyt}$ (Figure 5.17) indicate a decrease of $\langle \theta \rangle_{xyt}$ that remains almost constant with height for $z \gtrsim 50$ m. $\langle u \rangle_{xyt}$ decreases towards the surface for $z \lesssim 110$ m and the wind speed at the ground is larger than the value under neutral stratification (Figure 5.3 (a)) due to the additional surface heat flux.

5.2.2 Tracer Release

For homogeneous and inhomogeneous terrain settings the tracer concentration under convective conditions does not differ significantly (Figure 5.18). Compared to the

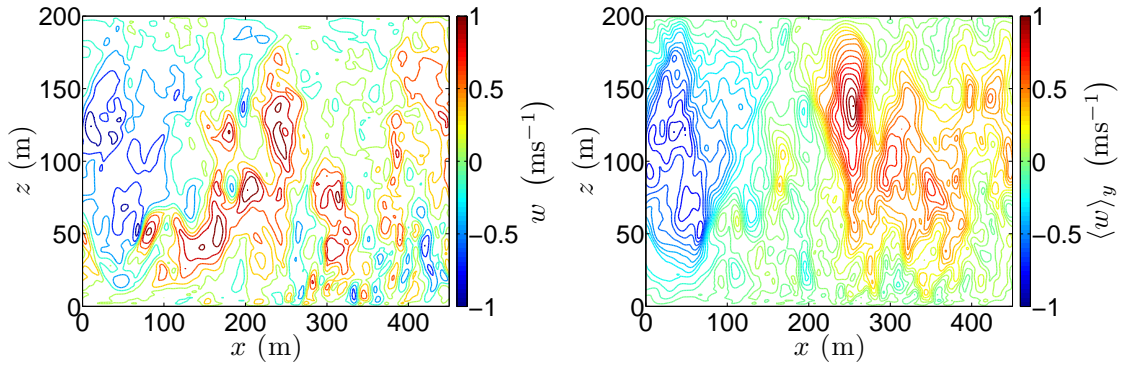


Figure 5.16: [FHC] Snapshot of w taken at $y = \frac{\Delta y_{ny}}{2}$ and laterally averaged vertical velocity $\langle w \rangle_y$ at $t = 18000$ s (right).

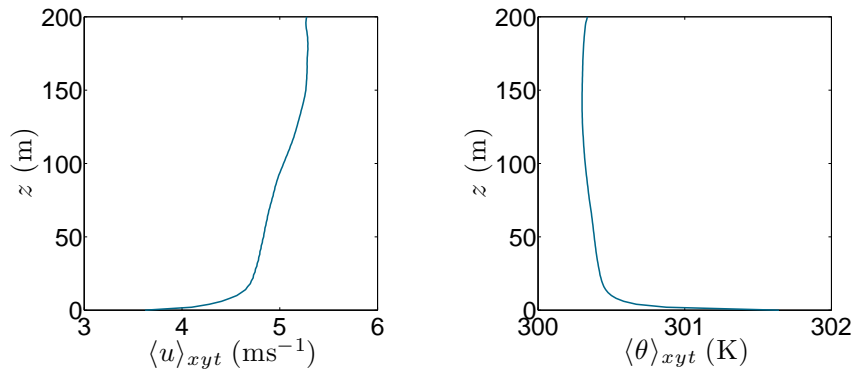


Figure 5.17: [FHC] Same as Figure 5.3 but for convective stratification.

plume in the turbulent boundary layer the additional buoyant turbulence can be clearly seen. The height of the maximum mean concentration changes significantly downstream and a distinctive vertical plume spread occurs. Pollutants can reach the surface even when released at $z_r = 52$ m. The decrease of $\max(\langle C \rangle_l)$ is rather continuous in the convective cases while $\max(\langle C \rangle_l)$ is reduced by more than a factor of two between $x = 50$ m and $x = 200$ m in the neutral simulations (Figure 5.20). In the turbulent cases $\max(\langle C \rangle_l)$ is strongly influenced by z_r .

As a further analysis the distance x_{dist} to the source and the time t_{th} until the tracer hits the ground are plotted for both neutral and convective stratification (Figure 5.19). x_{dist} and t_{th} are smaller under convective stratification due to the additional vertical velocity. The surface heat flux causes convection with large eddies so that the plume can reach

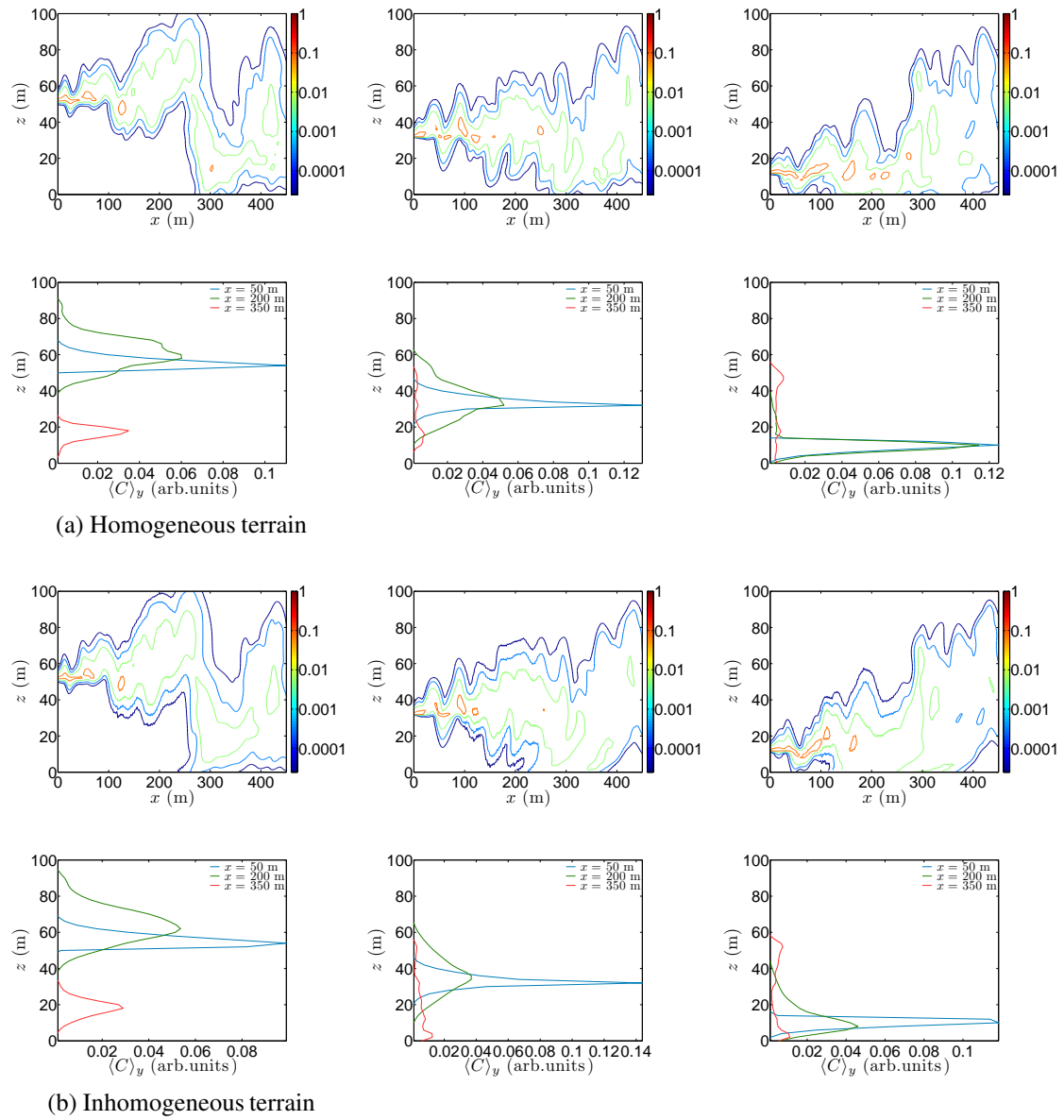


Figure 5.18: [FHC,FHRC] Dimensionless laterally averaged concentration contours and corresponding vertical concentration profiles over homogeneous (a) and inhomogeneous terrain (b). The height of the tracer release and the distance from the source at which the profiles are taken are the same as in Figure 5.9.

the surface for all values of z_r in contrast to the neutral cases. An influence of the surface inhomogeneity can only be observed when the source is located at $z_r = 52$ m.

The plume speed u_{plume} is computed as described in Section 5.1.2.1. It is influenced by z_r and by the surface roughness. For $z_r = 52$ m, u_{plume} is larger under neutral

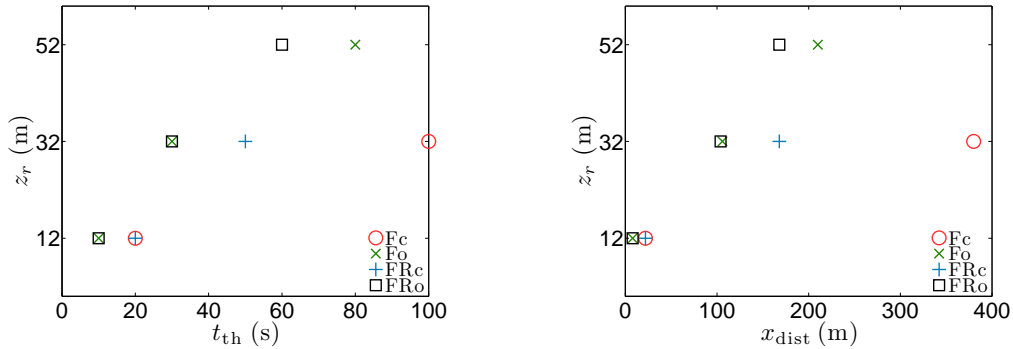


Figure 5.19: [Fc,FHc,FRc,FHRc] Same as Figure 5.14 but for convective and turbulent stratification.

stratification, while it is larger under convective stratification for $z_r = 12$ m (Figure 5.21). Differences between the four values of u_{plume} are smallest for $z_r = 32$ m and the variation is dependant on the terrain shape. While u_{plume} decreases with decreasing z_r in the turbulent boundary layer, there is no continuous decrease in the convective boundary layer because of the additional buoyant turbulence.

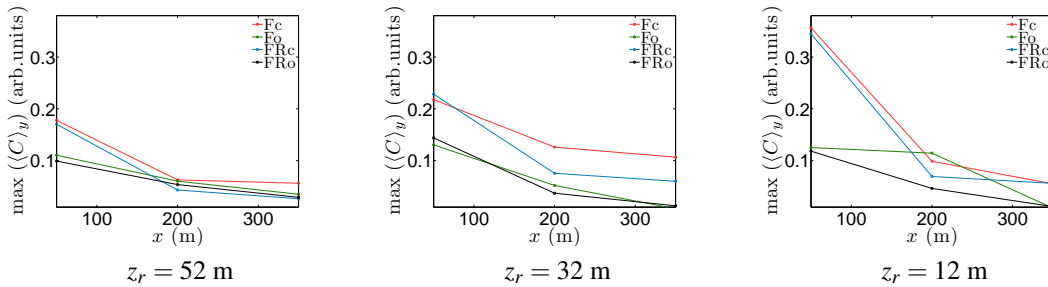


Figure 5.20: [Fc,FHc,FRc,FHRc] Same as Figure 5.15 but for convective and turbulent stratification.

5.2.3 Conclusions

A convective boundary layer develops when a surface heat flux is applied. The additional thermal turbulence has a significant influence on the tracer dispersion including a larger vertical spread of the plume. The higher the wind shear the longer the advection

time and the distance to the source where the tracer reaches the ground (Figure 5.19). The shear reduces the looping of the plume especially close to the source where large turbulent eddies are the main contribution to the vertical dispersion. This is consistent with the studies on buoyancy- and shear-driven flows by Moeng and Sullivan (1994) and Dosio et al. (2003). They performed LES studies considering the combined effect of thermal and mechanical forcing and observed that increasing wind tends to advect the plume horizontally for a longer time. The main effect of the wind shear is a reduction of the vertical plume spread, therefore the ground concentrations are strongly influenced.

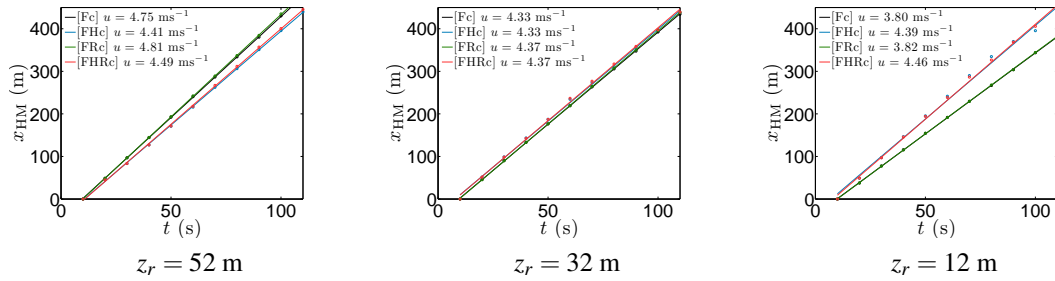


Figure 5.21: [Fc,FHc,FRc,FHRc] Same as Figure 5.6.

Table 5.1 shows a summary of the different simulations and the resulting atmospheric stratifications.

Cases	Turbulent (neutral)	Laminar (neutral)	Convective
Fc	X		
FRc	X		
Fo		X	
FRo		X	
FHc			X
FHRc			X

Table 5.1: Different simulations and their resulting atmospheric stratifications.

5.3 Characteristics of the Concentration Distribution

The concentration distribution with distance from the source shall be investigated. Therefore, the maximum mean concentration C_{peak} for each $y-z$ plane is computed

as a function of x . C_{peak} is continuously getting smaller with downstream position, but it is not monotonically decreasing due to the turbulent mixing (Figure 5.22). The larger vertical dispersion of the plume under convective stratification leads to a faster decrease of C_{peak} .

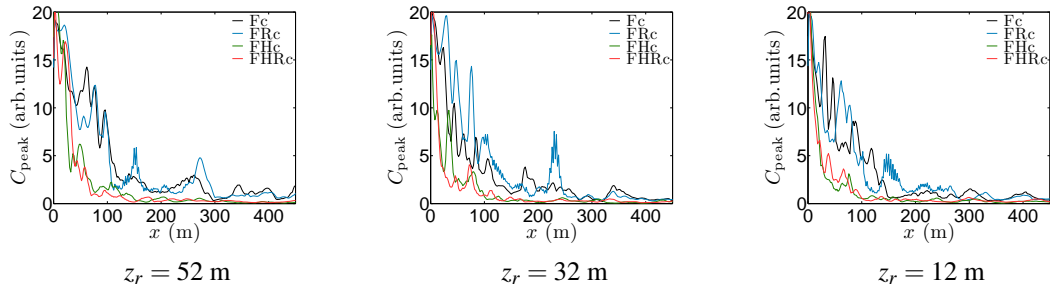


Figure 5.22: [**Fc**,**FHc**,**FRc**,**FHRc**] Maximum concentration C_{peak} in the $y - z$ plane as a function of x for the different release heights z_r .

Figure 5.23 shows the tracer concentration $\langle C_{\text{surf}} \rangle_y$ at the pedestrian height $z_p = 2$ m as function of x and averaged in the y -direction. The difference between the neutral and the convective stratification is significant when the tracer is released at $z_r = 52$ m and $z_r = 32$ m. $\langle C_{\text{surf}} \rangle_y$ is approximately 2 - 12 times larger than $\langle C_{\text{surf}} \rangle_y$ under neutral conditions. When the source is located at $z_r = 12$ m the influence of the buoyant turbulence is less significant because mechanical turbulence is the dominant mechanism.

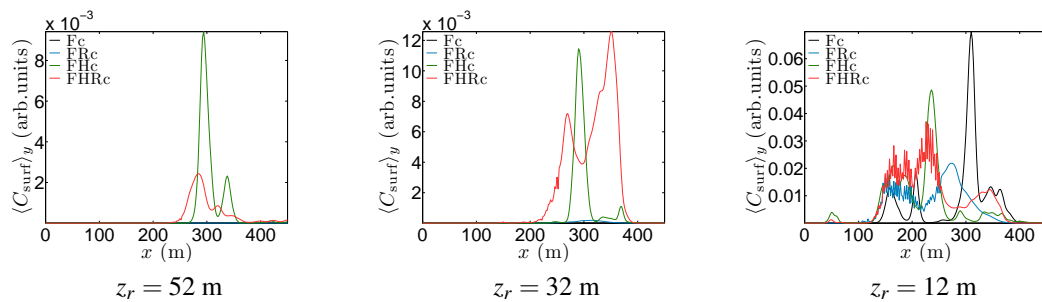


Figure 5.23: [**Fc**,**FHc**,**FRc**,**FHRc**] Laterally averaged concentration $\langle C_{\text{surf}} \rangle_y$ at the pedestrian height z_p as a function of x averaged in the for the three release heights z_r . Please note the different y -axis scales.

Chapter 6

Tracer Dispersion in an Idealised Aare Valley

In this chapter the tracer dispersion in an idealised Aare valley is studied. The application of street canyon flow characteristics to the geometry of the Aare valley is discussed, and the results of an analytical Gaussian plume model are compared with the output from the EULAG simulations. Furthermore, the flow above a homogeneous and inhomogeneous flat terrain is matched against the flow above the Aare topography. Two main questions arise:

1. Is the flow across the Aare valley comparable to the flow above a street canyon?
2. What is the difference between the results of a Gaussian plume model and the results of the EULAG simulations?

6.1 Comparison of the EULAG Simulations with a Street Canyon Flow

6.1.1 Street Canyon Flow

A street canyon is defined as a narrow street that is surrounded by high buildings on each side. Although no real street canyon is considered in the simulations, the

geometry of the Aare valley (Figure 4.3) shows similarities to this definition. Figure 6.1 shows a description of the terms that are used. The leeward side corresponds to the west shore of the Aare while the windward side corresponds to the east shore. H is the average height of the buildings which, in this study, is the mean height of the east and west terrain in the Aare valley. The canyon width W is equivalent to the width of the Aare. As the eastern area is lower than the western terrain height the setup corresponds to a step down canyon.

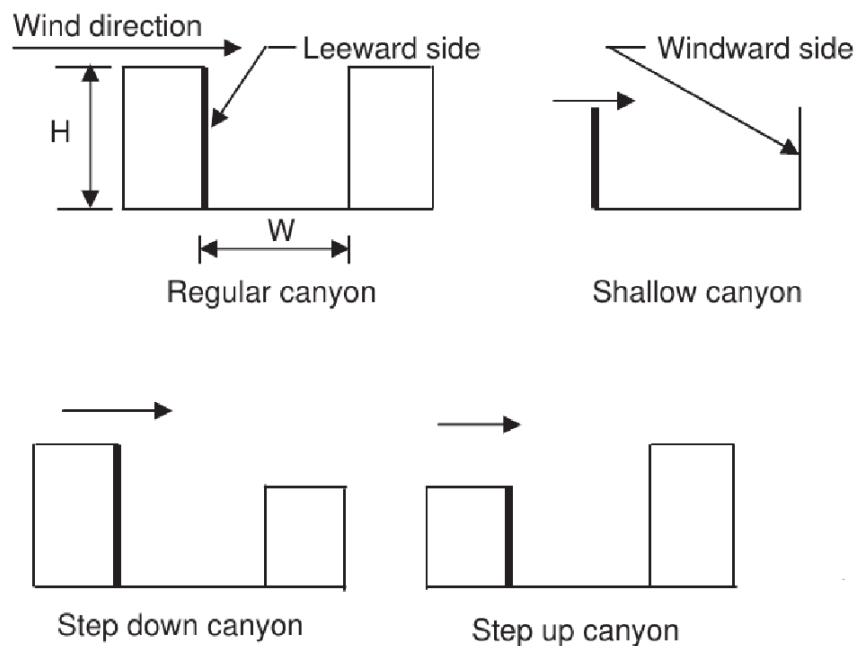


Figure 6.1: Description of street canyon characteristics. Adapted from Ahmad et al. (2005).

According to Oke (1988) the flow inside the street canyon depends on the geometry: the building density and the H/w ratio. As the building density is not applicable for this case study, only the H/w ratio, also called aspect ratio, is referred to. There are three different types (see Figure 6.2): the Isolated Roughness Flow (IRF: $H/w < 0.3$), the Wake Interference Flow (WIF: $0.3 < H/w < 0.7$) and the Skimming Flow (SF: $H/w > 0.7$) (Li et al., 2006; Vardoulakis et al., 2003). In the IRF regime the flow fields that are related to the individual buildings do not interact. In the WIF regime the mean flow is disturbed by the formed eddy while in the SF regime the flow inside the street canyon is decoupled from the flow above the canyon.

The Aare setup corresponds to an IRF because the aspect ratio is

$$\frac{H}{W} = \frac{15 \text{ m}}{150 \text{ m}} = 0.1$$

$H = \frac{22+8}{2}$ m is the average height between the west and the east side of the Aare.

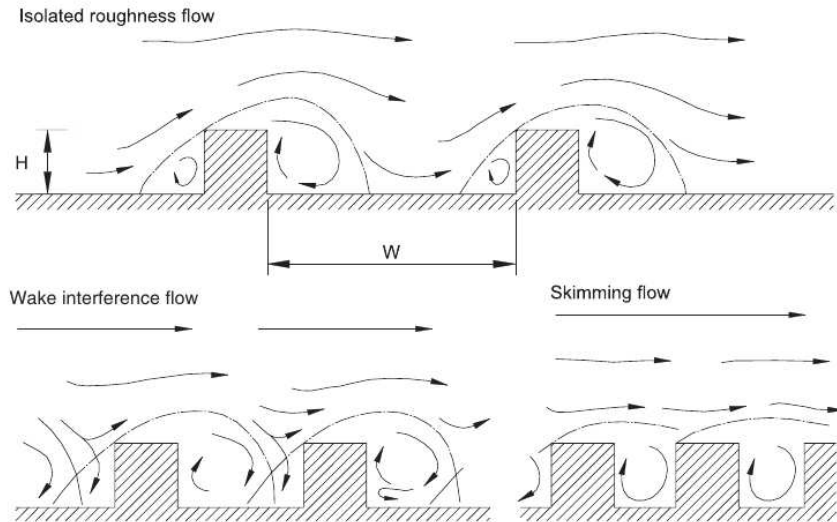


Figure 6.2: Three flow regimes associated with different values of the aspect ratio H/w (Li et al., 2006).

6.1.2 Velocity and Concentration Profiles

Figure 6.3 shows $\langle u \rangle_{yt}$ and $\langle w \rangle_{yt}$ for the three cases T1 (also called neutral stratification in the following), TH1 and TH2 (referred to as convective stratification in this chapter) after 30 min simulation time. For a description of the different cases see Table 4.4. In all cases downdrafts and updrafts occur at the west and east shore, respectively. The thermal updraft due to temperature differences has a minor influence. It is largest in the case TH2 where the downdraft is less confined to the western shore and covers also a part of the Aare and the eastern shore. The updraft at the shore in this case therefore becomes smaller than in the neutral case. This tendency can already be seen in TH1 with the smaller surface heat flux. $\langle u \rangle_{yt}$ is only slightly influenced by the up- and downwinds as is the mean vertical velocity $\langle w \rangle_{yt} \approx 1 \text{ ms}^{-1}$ on average. It remains almost the same for each thermal stratification.

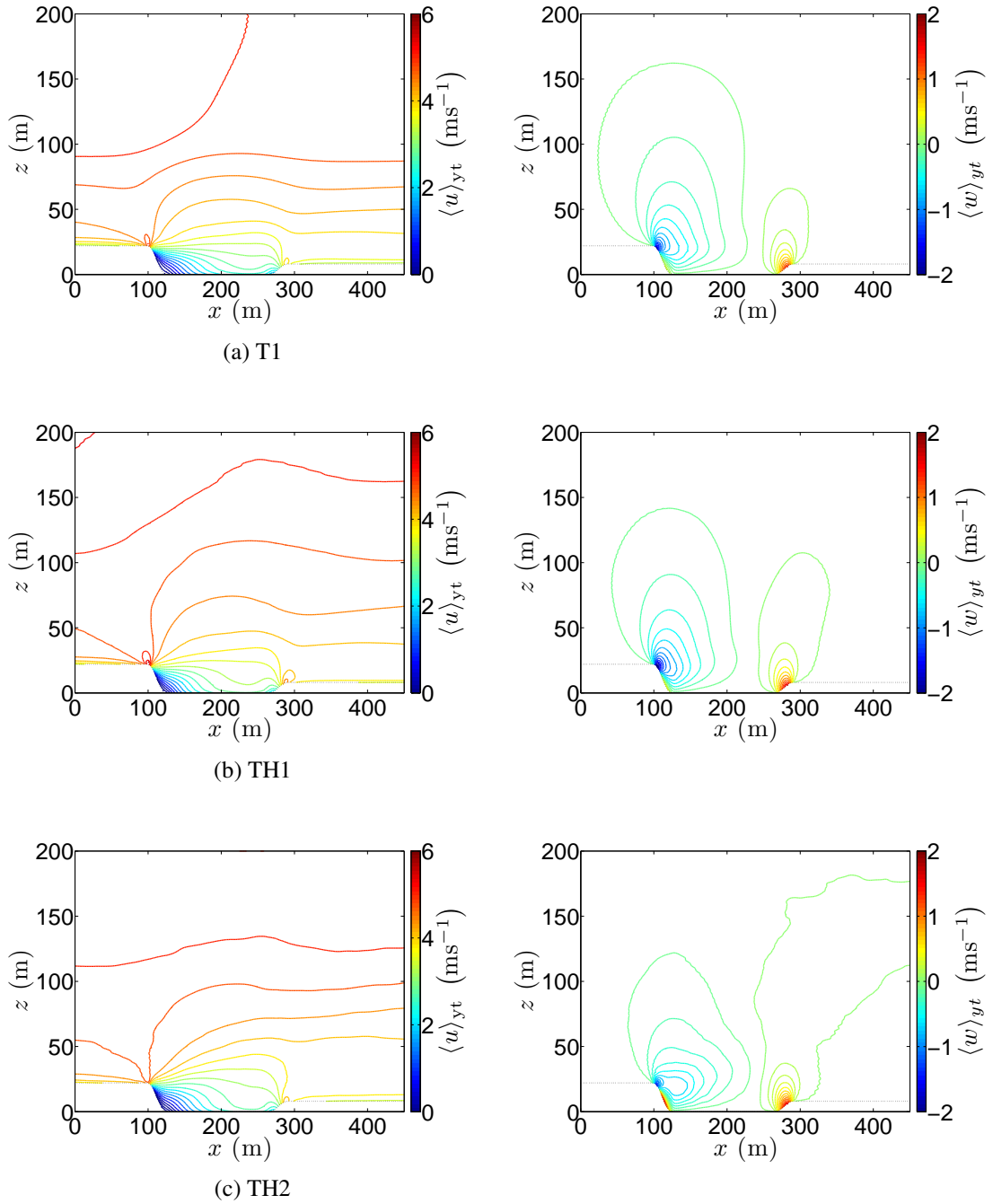


Figure 6.3: [T1,TH1,TH2] Contours of laterally and temporally averaged horizontal $\langle u \rangle_{yt}$ and vertical $\langle w \rangle_{yt}$ velocity for neutral (a) and convective stratification (b) and (c) at $t = 18000$ s. The dashed line represents the topography.

In contrast to the classical IRF one eddy forms at the leeward side, but there is no eddy at the windward side. Huang et al. (2000) performed simulations with different canyon

geometries and found out that a formed vortex moves closer to the leeward wall and turns from circular to elliptical with decreasing aspect ratio but all setups had the same building height on the left and right side. There are also studies considering different building heights such as step-up and step-down canyons (Assimakopoulos et al., 2003) or roof geometries (Kastner-Klein et al., 2004) but these studies deal with SF or WIF regimes because the IRF can be considered as a flow over isolated buildings or simple obstacle arrays. The flow patterns around an isolated obstacle include the upstream displacement and recirculation zone at the windward wall, the cavity zone (also called recirculation or wake zone) at the lee wall of the obstacle and the wake zone downwind of the cavity (see e.g. Hanna et al. (2002) and references therein). To our knowledge no study has been performed considering an IRF flow within a step-down canyon. In the Aare canyon setup the height of the eastern area is 15 m smaller than the western area and the shore is not perpendicular, therefore no recirculation zone at the windward shore exist.

Figure 6.4 shows the concentration contours C in the centerline of the plume at $t = 200$ s. With increasing surface heat flux Q_{hf} the release height z_r has less influence on the tracer dispersion because large eddies form which transport pollutants to the surface. The vertical spread of the plume increases from $\Delta z \approx 100$ m (T1) to $\Delta z \approx 200$ m (TH2). Due to the absence of bouyant convection the Aare topography becomes more significant under neutral stratification. The downwards directed vertical velocity at the eastern shore transports the tracer to the surface (see Figure 5.9 for a comparison). The influence is stronger with decreasing z_r and can also be seen in the case TH1 in contrast to TH2 as explained above. The characteristics of plume behaviour and concentration distribution are further discussed in Section 6.2.

6.1.3 Turbulent Kinetic Energy and Turbulent Statistics

Street canyon flow is highly turbulent, therefore the turbulent kinetic energy $\langle \text{TKE} \rangle_y$, the turbulent fluxes of momentum $\langle u'w' \rangle_y$ and heat $\langle w'\theta \rangle_y$, as well as the mean streamwise velocity $\langle u \rangle_{yt}$ are investigated. Vertical profiles at three different locations above the Aare are shown: in the west ($x = 126$ m), in the middle ($x = 196$ m) and in the east ($x = 264$ m) of the river.

Figure 6.5 shows the profiles of the mean streamwise velocity $\langle u \rangle_{yt}$ at the three x -

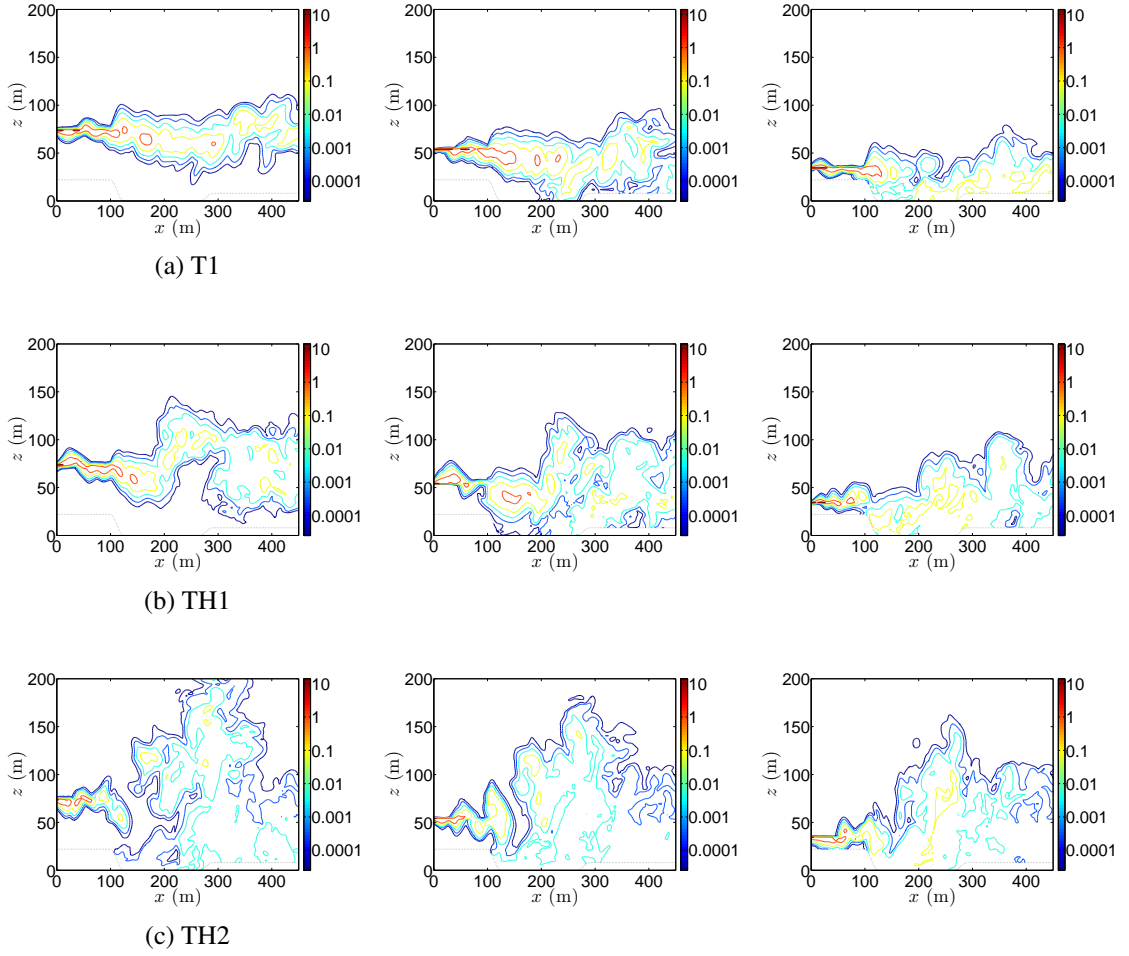


Figure 6.4: **[T1,TH1,TH2]** Dimensionless concentration contours C for $z_r = 73.7$ m (left), $z_r = 54.6$ m (middle) and $z_r = 34.4$ m (right) in the centerline of the plume $y = \frac{ny-\Delta y}{2}$ at $t = 200$ s. The dashed line represents the topography.

positions. The profiles $\langle u \rangle_{yt}$ only differ for $z/H \lesssim 3$. In the west $\langle u \rangle_{yt}$ is negative at the surface due to the forming eddy at the leeward shore. An inflection point exists at $z/H \cong 2$, i.e. $\langle u \rangle_{yt}$ increases slower above this height. Typical for an IRF the disturbed flow can readjust before reaching the east shore, as can be seen by the increase of $\langle u \rangle_{yt}$ for $z/H \lesssim 3$ further downstream. To compare the results with the flow over a homogeneous and inhomogeneous surface as discussed in Chapter 5, $\langle u \rangle_{yt}$ is plotted in the west, in the middle and in the east above the roughness elements for the flow over an inhomogeneous terrain. Over a homogeneous surface the same positions are chosen (Figure 6.6). As expected, the vertical profiles only slightly change over the homogeneous terrain. Above the inhomogeneous terrain the mean velocity decelerates

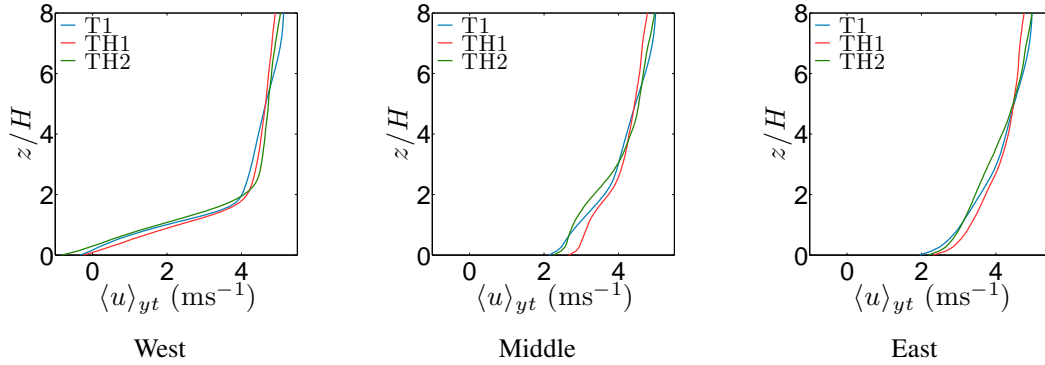


Figure 6.5: [T1,TH1,TH2] Temporally and laterally averaged profiles of the velocity $\langle u \rangle_{yt}$ at $x = 126$ m (left), $x = 196$ m (middle) and $x = 264$ m (right).

due to the roughness elements but it does not become negative or zero as it is the case in the west of the Aare canyon. A qualitative comparison between the flow over a flat inhomogeneous terrain with the flow over the Aare canyon is thus not possible.

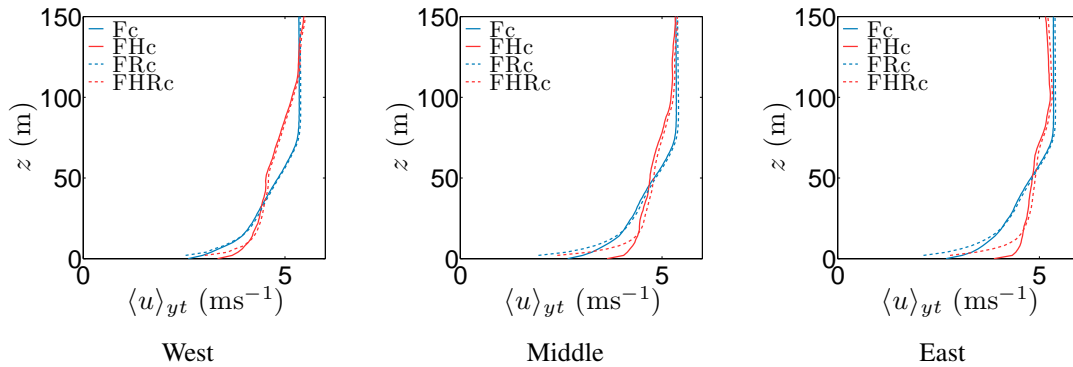


Figure 6.6: [Fc,FHc,FRc,FHRc] Temporally and laterally averaged profiles of the velocity $\langle u \rangle_{yt}$ at the same x -positions as in Figure 6.5. The dashed lines denote the profiles above the roughness area. $\langle u \rangle_{yt}$ is zero below the averaged height of the roughness.

The vertical profiles of the across-flow averaged turbulent fluxes $\langle \text{TKE} \rangle_y$, $\langle u'w' \rangle_y$ and $\langle w'\theta \rangle_y$ are illustrated in Figure 6.7. Only the resolved fluxes of the LES are shown. In the west the profiles have their maximum near the averaged shore height $z/H = 1$ except for the turbulent heat flux under neutral stratification (T1) because the surface is not heated. The inflection point in $\langle u \rangle_{yt}$ causes instabilities that generate a turbulent transport. The height of the inflection points of the turbulent fluxes is smaller than

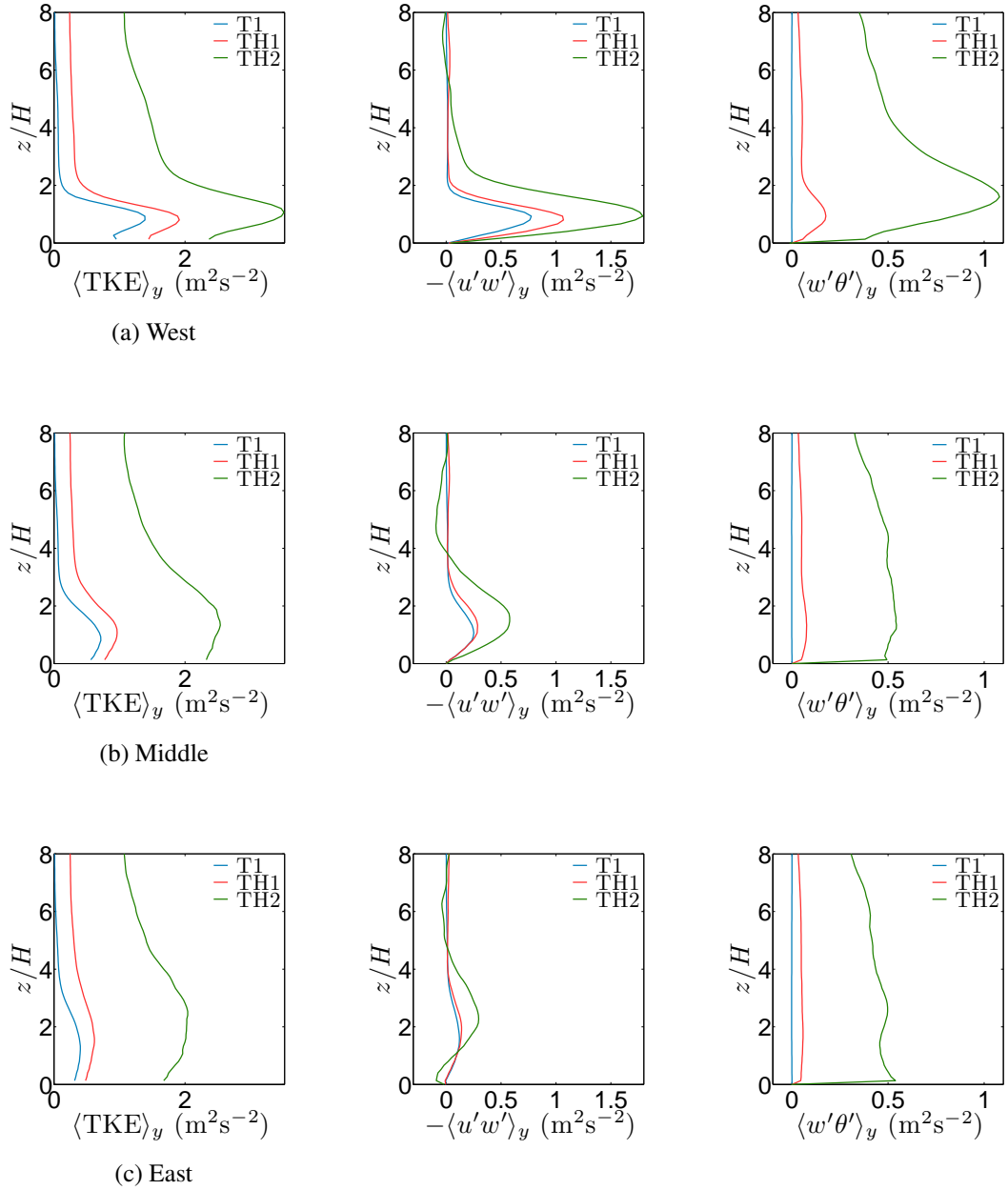


Figure 6.7: [T1,TH1,TH2] Vertical Profiles of the turbulent fluxes $\langle \text{TKE} \rangle_y$, $\langle u'w' \rangle_y$ and $\langle w'\theta' \rangle_y$ at $x = 126$ m (a), $x = 196$ m (b) and $x = 264$ m (c) averaged over 20 min.

the inflection point of $\langle u \rangle_{yt}$. This means that the instabilities caused by the change of $\langle u \rangle_{yt}$ generate a turbulent transport downward into the Aare canyon. In the middle and in the east of the Aare the turbulent fluxes become smaller and there is no distinctive difference between the profiles. The decrease of the turbulent fluxes is based on the

IRF because the disturbed flow can readjust before reaching the east shore. In the west $\langle \text{TKE} \rangle_y$, $\langle u'w' \rangle_y$ and $\langle w'\theta \rangle_y$ are nearly zero except for the case TH2. In this case the surface heat flux leads to a larger turbulent flux of heat than in the other two cases and the TKE is larger, too.

6.1.4 Surface Heat Flux

Simulations are performed for neutral and convective stratification including two different surface heat fluxes Q_{hf} . It shall be studied how Q_{hf} influences the turbulence generation and the tracer dispersion across the Aare valley.

6.1.4.1 Influence on the Turbulence

The amount of mechanically and buoyant generated turbulence above the Aare shall be identified which is supposed to be dependent on the surface heat flux Q_{hf} . The turbulence can be determined with the TKE governing equation that describes the turbulence generating processes (Equation (2.3)). Terms I and II are relevant. Figure 6.8 shows the vertical distributions of buoyant and mechanical production in the west and in the east of the Aare canyon. In the west the mechanically generated turbulence dominates at the surface under both neutral and convective stratification while the difference between the two terms becomes smaller in the east. For the case TH2 the buoyancy term is larger than the shear term and the shear generation is negative close to the ground although it is supposed to be positive in the surface layer (Stull, 1989). A possible reason could be the chosen value $Q_{\text{hf}} = 0.6 \text{ Kms}^{-1}$ because the surface heat flux on a typical sunny day in Southern Germany is $Q_{\text{hf}} = 0.06 \text{ Kms}^{-1}$ (Schmidt and Schumann, 1989). Summarised, the mechanical production term is about one magnitude larger in the west than in the east because a characteristic canyon flow profile is observed. Further downstream where the flow readjusts, the influence of the mechanical turbulence decreases and the surface heat flux has a more significant influence.

6.1.4.2 Influence on the Tracer Dispersion

The difference of the plume shape and concentration distribution depending on the thermal stratification and the release height was already discussed in Section 6.1.2.

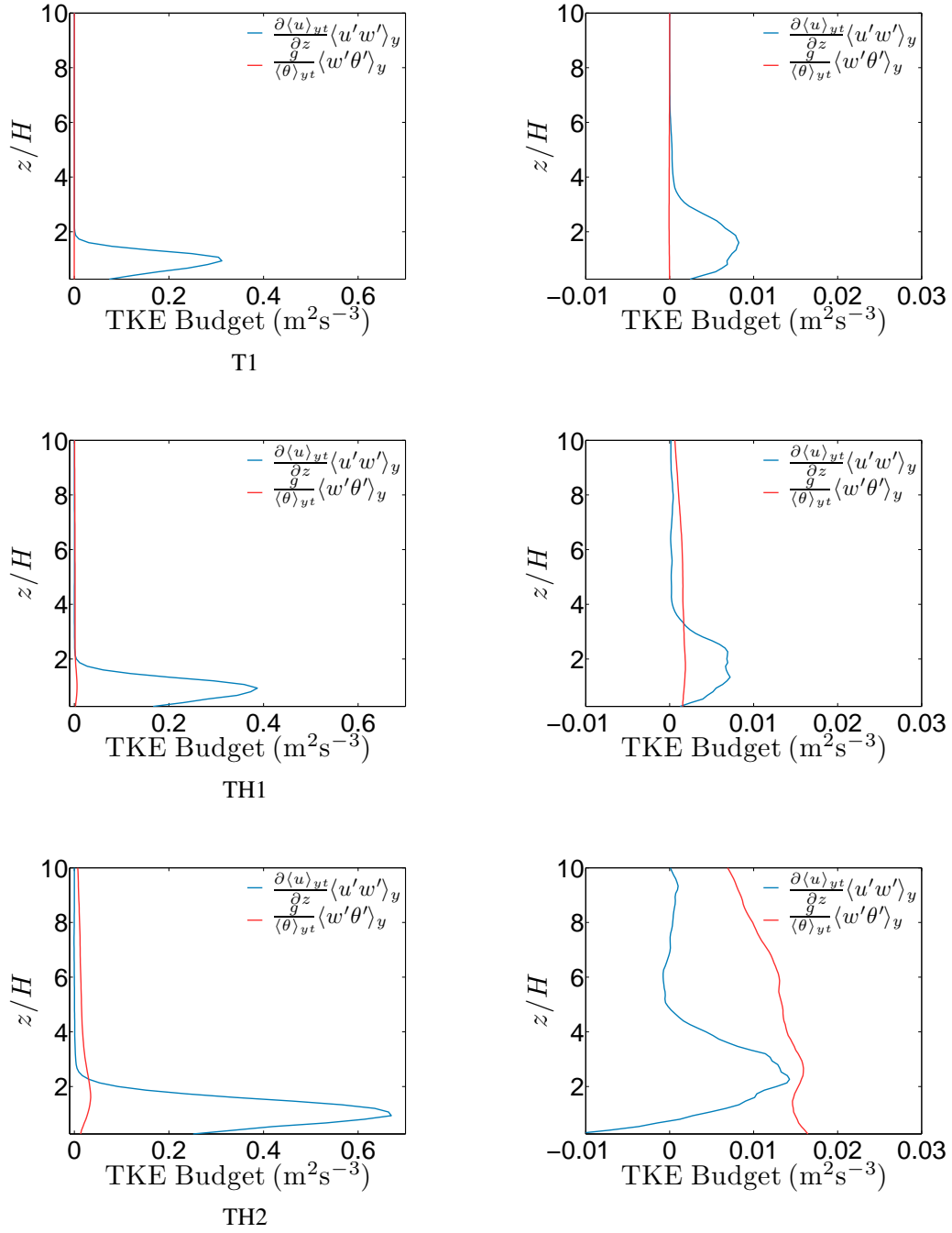


Figure 6.8: [**T1,TH1,TH2**] Vertical distributions of buoyant and shear production terms in the TKE budget for T1, TH1 and TH2. The vertical profiles are averaged over 20 min and taken at the western (left) and eastern shore (right). Please note the different x -axis scales.

Now the distance x_{dist} to the source where the tracer hits the pedestrian height z_p , and the time t_{th} taken for this distance, shall be determined. For a description see Section

5.1.4. Figure 6.9 (a) shows Q_{hf} as a function of x_{dist} and t_{th} . Two main characteristics are illustrated. x_{dist} becomes smaller with both increasing Q_{hf} and decreasing release height z_r . t_{th} also becomes smaller with decreasing z_r (Figure 6.9) but for an increasing surface heat flux this characteristic is only fulfilled for $z_r = 73.7$ m and for $z_r = 54.6$ m given $Q_{\text{hf}} > 0.06 \text{ K s}^{-1}$.

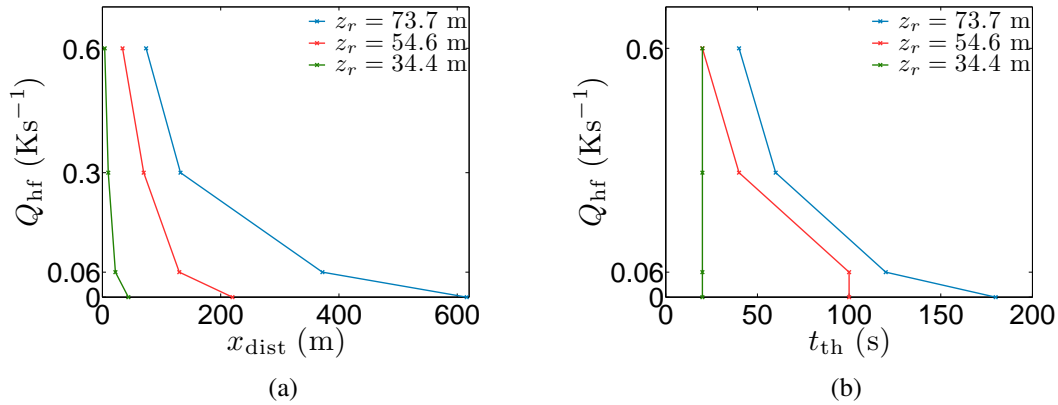


Figure 6.9: [T1,TH1,TH2] Q_{hf} as a function of x_{dist} (a) and time t_{th} (b). See also text.

6.1.5 Conclusions

The flow across the idealised Aare valley can be described by an IRF regime. At the west shore the turbulence rises and the mean velocity decreases inside the canyon. In the downstream direction the flow readjusts to the surface. Due to the small slope and height of the shore the displacement zone and the characteristic eddy at the west side of the Aare do not exist. With increasing surface heat flux the turbulent fluxes and the turbulent kinetic energy rises. Its influence on the flow is smallest in the west of the Aare where the mechanical turbulence dominates buoyancy. The Aare topography and the surface heat flux also affect the tracer dispersion. Under neutral stratification and for a low release height the surface shape influences the plume. With increasing surface heat flux the tracer can reach the surface nearly independent of the release height due to the thermal convection.

Wind flow over a homogeneous and inhomogeneous flat terrain leads to different velocity and concentration profiles than the flow across the Aare valley. Under neutral stratification the main difference between the dispersion over a homogeneous and an

inhomogeneous flat terrain is the widening of the plume when it reaches the roughness elements. This results in a larger vertical plume spread. In contrast, the surface inhomogeneity does not influence the dispersion under convective stratification due to the thermal turbulence that causes eddies much larger than the velocity variation over the roughness elements (see Figure 5.18). A simple change of surface roughness can therefore not mimic the flow in and above a canyon.

6.2 Comparison of the EULAG Simulations with a Gaussian Plume Model

In this Section the concentration distribution χ , calculated with an analytical Gaussian plume model (Equation 2.1), is compared with the concentration distribution C of the EULAG simulations.

6.2.1 Analytical Gaussian Plume Model

For a first comparison of the analytical Gaussian plume model with the EULAG simulations the neutral simulation Fc over flat terrain with a release height $z_r = 32$ m is taken. The concentration χ is calculated along the spanwise centerline $y = 0$ of the plume. Equation (2.1) then becomes

$$\chi(x, 0, z) = \frac{Q}{2\pi\langle u \rangle \sigma_y \sigma_z} \left[\exp\left(\frac{-(h_{\text{eff}} - z)^2}{2\sigma_z^2}\right) + \exp\left(\frac{-(h_{\text{eff}} + z)^2}{2\sigma_z^2}\right) \right]$$

with

$$\begin{aligned} \sigma_y &= \sigma_y(x) = p_y \cdot x^{q_y} \\ \sigma_z &= \sigma_z(x) = p_z \cdot x^{q_z} \end{aligned} \tag{6.1}$$

The reference velocity $\langle u \rangle$ is the temporally averaged velocity $\langle u \rangle_t = 4.43 \text{ ms}^{-1}$ in the grid cell of the tracer source, taken from the simulation Fc. It is only initialised in the source term of equation (6.1) and it does not change downstream. The same emission rate $Q = 50 \text{ s}^{-1}$ as used for the EULAG simulations is chosen. The coefficients p_y , q_y , p_z and q_z are taken from German Federal Ministry of Justice (1990) on which the calculation of the coefficients within the model ESS41 is based. For the chosen release

height $z_r = 32$ m and neutral stratification (stability class D) the following constant coefficients must be used:

$$\begin{aligned} p_y &= 0.640 & q_y &= 0.784 \\ p_z &= 0.215 & q_z &= 0.885 \end{aligned}$$

6.2.2 First Results

Figure 6.10 shows the vertical profiles of χ and C as a function of x . The main dif-

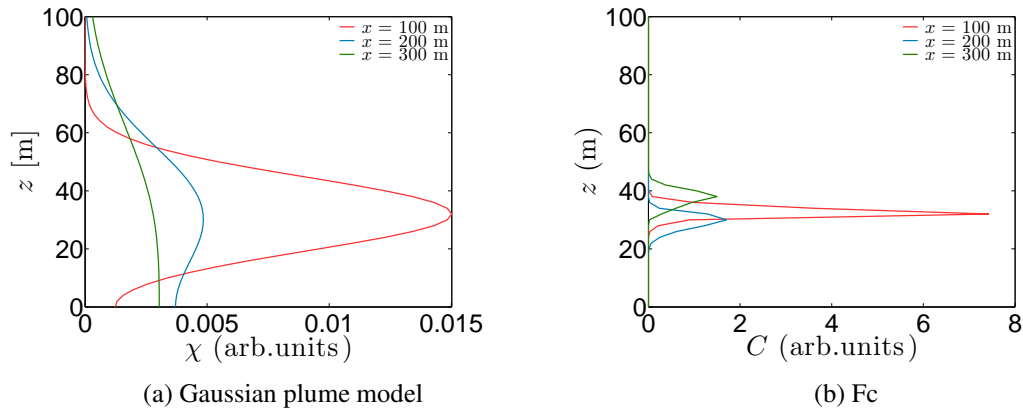


Figure 6.10: [F_c] Vertical profiles of the concentration distribution at $x = 100$ m, $x = 200$ m and $x = 300$ m. Compared are the results of an analytical Gaussian plume model (a) and the EULAG simulation F_c (b). The vertical profiles are taken at $y = 0$ (a) and $y = \frac{ny \cdot \Delta y}{2}$ at $t = 100$ s (b).

ference between the two models is the shape of the plume. The vertical spread of χ is larger than the vertical spread of C so that the plume can already reach the surface at $x = 100$ m. Using EULAG the mean maximum concentration peak shifts in the z -direction while it remains at the same height using the Gaussian plume model. Furthermore, χ is approximately two orders of magnitude smaller than C .

The determined σ -values are valid for a temporal average over one hour, therefore dispersion and concentration distribution differs from an instantaneous plume as illustrated in Figure 6.11. As explicit turbulent dispersion is not taken into account by the Gaussian plume model the concentration C is averaged over one hour in the interval $[0, 6, \dots, 60$ min] and plotted as a function of x using $\langle u \rangle_t = 4.09 \text{ ms}^{-1}$ (Figure 6.12). The maximum concentration becomes smaller and the vertical plume spread is larger

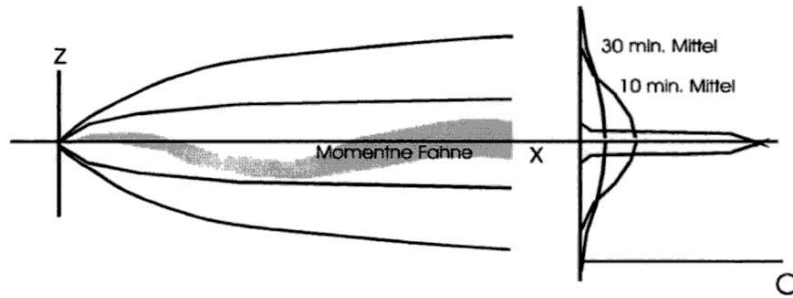


Figure 6.11: Influence of different averaging times on the form of the Gaussian distribution. From Zenger (1998, p. 90).

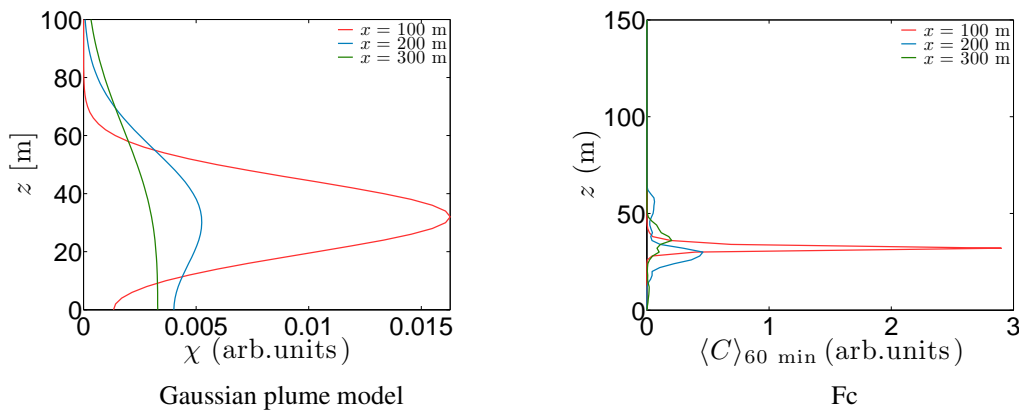


Figure 6.12: [Fc] Same as Figure 6.10 but for $\langle C \rangle_{60 \text{ min}}$ averaged over one hour.

in contrast to the non-averaged concentration profiles (Figure 6.10 (b)) but the fluctuations do not diminish and the vertical shift in the z -direction still exists. Possibly, an average using data at more time steps would lead to a higher vertical plume spread and a smaller maximum concentration but this would probably not result into a decrease of about two orders of magnitude.

Figure 6.13 shows the mean maximum concentration values $\max(C)$, the temporally averaged concentration $\max(\langle C \rangle_{60 \text{ min}})$ and $\max(\chi)$ as a function of x . An exponential function is fitted to the data points of C and $\max(\langle C \rangle_{60 \text{ min}})$. The fluctuations of C decrease when averaged over one hour and $\max(\langle C \rangle_{60 \text{ min}}) < \max(C)$ because the spread in the y -direction becomes larger with time and Figure 6.10 only shows the maximum concentration values at $y = \frac{ny \cdot \Delta y}{2}$. While the maximum concentration of the EULAG simulations decreases with $\exp(-x)$, $\max(\chi)$ decreases with $\exp(-x^2)$. The

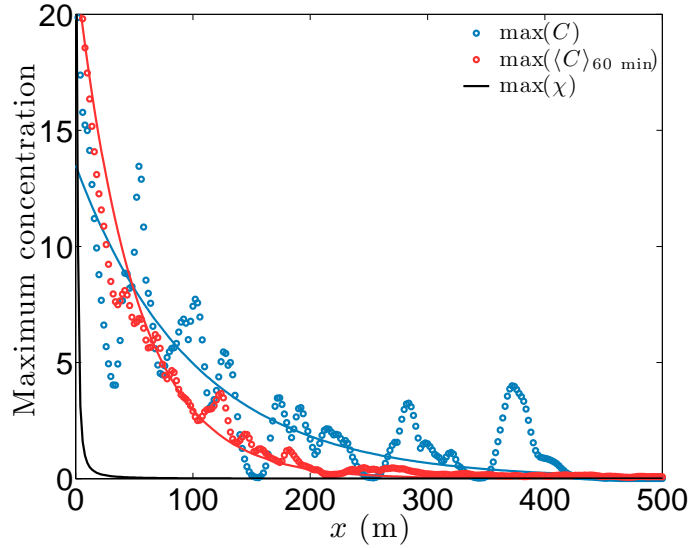


Figure 6.13: [Fc] Maximum concentration $\max(C)$ (blue points), $\max(\langle C \rangle_{60 \text{ min}})$ averaged over one hour (red points) and $\max(\chi)$ (black) as a function of x in the centerline of the plume. The blue and red curves denote exponential fits to the data points. The maximum values in the z -direction are determined at $y = 0$ and $y = \frac{ny\Delta y}{2}$.

disagreement is distinctive for $x \lesssim 200$ m where Gaussian plume models are known to be incorrect (see Section 2.2.4 and Figure 2.5). With growing distance to the source the maximum concentration values converge.

6.2.3 Application of the Gaussian Plume Model in the Idealised Aare Canyon Setup

In order to compare the plume shapes above the Aare valley the concentrations $\chi(x, y = 0, z)$ are plotted in Figure 6.14. The applied stability classes are D (comparison with T1), C (comparison with TH1) and B (comparison with TH2) using the following σ -coefficients:

Class B :	$p_y = 0.876$	$q_y = 0.823$
	$p_z = 0.127$	$q_z = 0.108$
Class C :	$p_y = 0.659$	$q_y = 0.807$
	$p_z = 0.165$	$q_z = 0.996$

The source heights are $h_s = 52$ m, 32 m and 12 m. For a comparison with the EULAG simulations $z = 22$ m is added to h_s to get the topographic heights $h_t = 74$ m, 54 m and 34 m so that $h_t = h_s + 22$ m. The addition can only be done after the computation because the result would be different as can be seen in Equation 6.1 (see also Section 4.2).

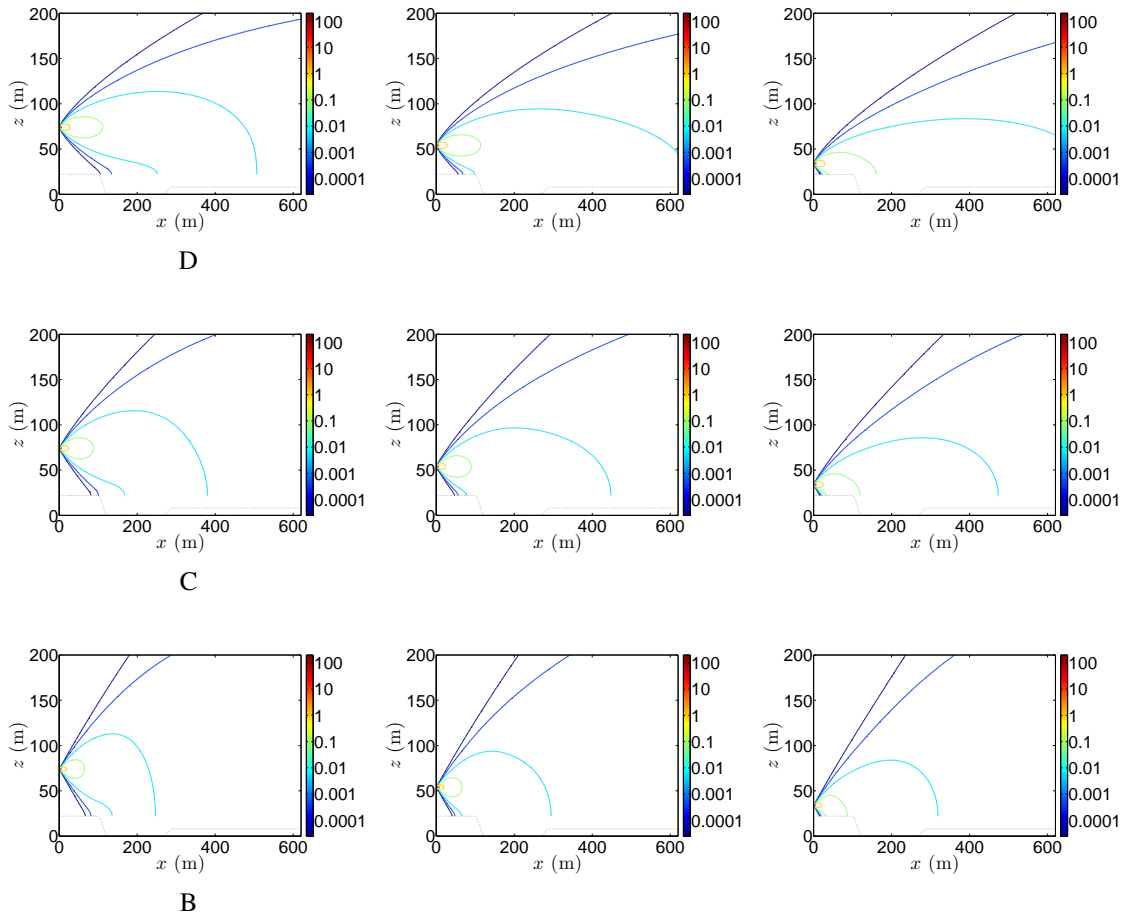


Figure 6.14: Concentration contours averaged over 60 min computed with the Gaussian plume model for the release heights $h_s = 52$ m (left), $h_s = 32$ m (middle), $h_s = 12$ m (right) using the stability classes D (neutral), B (slightly unstable) and B (moderately unstable). The cross section is taken in the centerline $y = 0$.

The topography (dashed line) in Figure 6.14 is shown for a comparison with the EULAG simulations but it has no influence on the tracer dispersion. The difference of the concentration distribution between the tracer dispersion under the three thermal stratifications ranging from neutral to moderately unstable is small. With decreasing release height the concentration at the surface rises in the vicinity of the source. Compared

to the EULAG simulations (Figure 6.4) the missing fluctuations and the irrelevance of the surface shape are evident. However, it must be kept in mind that Figure 6.4 shows an instantaneous plume after 200 s. Therefore an average of the tracer concentration C over 1 hour is performed and the cross section in the centerline $y = \frac{ny \cdot \Delta y}{2}$ is taken. The results for T1, TH1 and TH2 for $z_r = 54.6$ m are shown in Figure 6.15. Compared to the instantaneous cross sections after $t = 200$ s (Figure 6.3) the vertical concentration distribution is more uniform and the vertical plume spread rises in all cases. Under neutral stratification the plume does not cover more than half of the domain in the vertical while it covers the whole domain after $x \approx 350$ m when stability class D is applied. Under convective stratification the plume spread and the concentration distribution is similar in both models. The difference is mainly evident in the concentration inhomogeneity due to turbulent diffusion.

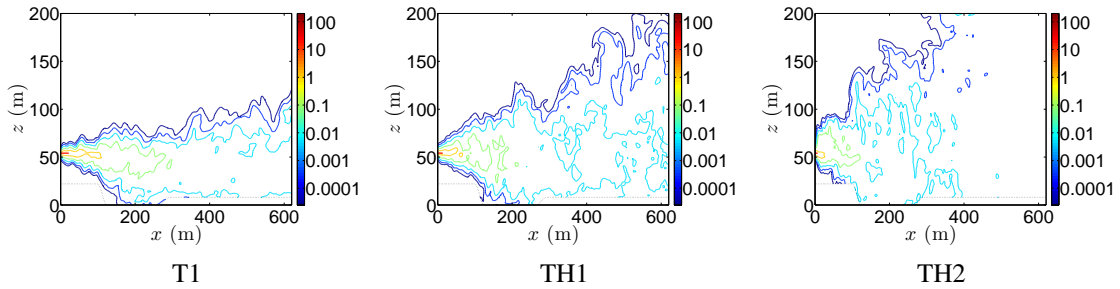


Figure 6.15: [T1,TH1,TH2] Dimensionless concentration contours $\langle C \rangle_{60 \text{ min}}$ averaged over 60 min for $z_r = 54.6$ m in the centerline of the plume $y = \frac{ny \cdot \Delta y}{2}$.

6.2.4 Plume Behaviour at the Pedestrian Height

Figure 6.16 illustrates the distance from the source where the tracer hits the pedestrian height $z_p = 2$ m for both the Gaussian plume model (a) and the EULAG simulations (b), (c) and (d). Figure 6.16 (b) shows x_{dist} for a temporally averaged concentration distribution, Figure 6.16 (c) shows the same but for a flat topography ($z = 22$ m) without the Aare canyon. In Figure 6.16 (d) x_{dist} denotes the distance from the source where the tracer reaches z_p the first time after the release.

Using the Gaussian plume model the influence of both the thermal stratification and the release height have less influence compared to the EULAG results. x_{dist} is not larger

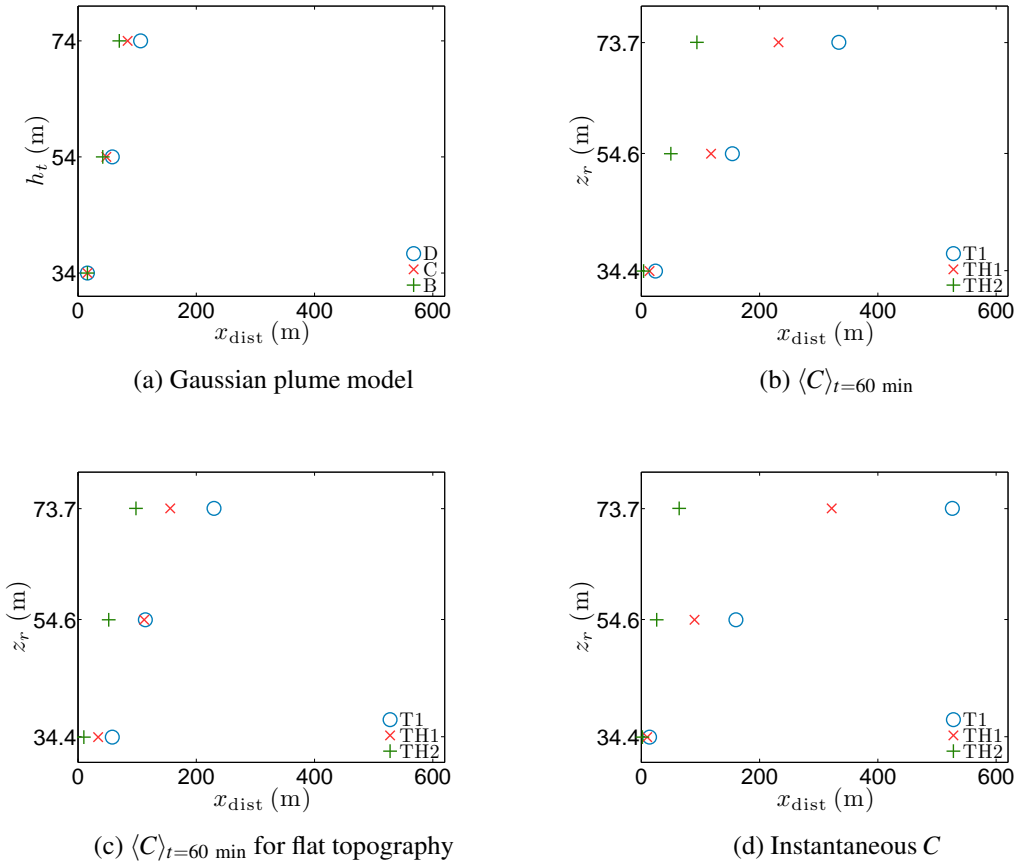


Figure 6.16: [**T1,TH1,TH2**] Distance from the source x_{dist} until the tracer hits the pedestrian height z_p depending on the release height for the Gaussian plume model (a) and the EULAG simulations with concentration values averaged over one hour (b) and (c) and an instantaneous plume after $t = 200 \text{ s}$ (d). In plot (c) the surface height is set to $z = 22 \text{ m}$.

than 106 m and at $h_t = 34 \text{ m}$ it is the same for all stability classes. The difference to the EULAG simulations is smallest for the tracer dispersion over a flat terrain (Figure 6.16 (c)) as expected. However, x_{dist} is approximately twice as large for the case T1 and about $1/3$ larger for TH1. The best agreement is observed for the stability class *B* and the simulation TH2. The variation between T1 and TH1 is most dominant at $z_r = 73.3 \text{ m}$ and more distinctive for the case T1. Without averaging x_{dist} is larger because a time average over one hour increases the probability for the tracer to reach the surface in the vicinity of the source. This probability gets smaller with decreasing z_r because of the dominant mechanical turbulence close to ground.

Disregarding the exact values of x_{dist} , the systematic is similar to that found for the

tracer dispersion over a flat terrain: The smaller the release height and the larger the surface heat flux, the closer to the source the tracer hits the ground independent of the respective model.

6.2.5 Vertical Concentration Distribution

A comparison of the vertical concentration profiles of $\langle C \rangle_{60 \text{ min}}$ and χ at the four locations $x = 50 \text{ m}$ (in the area west of the Aare), $x = 126 \text{ m}$ (west shore), $x = 264 \text{ m}$ (east shore) and $x = 500 \text{ m}$ (in the area east of the Aare) is performed (see for instance Figure 6.15 for an identification of those locations). The release height is $z_r \approx 54 \text{ m}$ which corresponds to $z_r = 32 \text{ m}$ above the surface, the approximate release height of the pollutants at PSI.

The mean maximum concentration χ decreases by two orders of magnitude between $x = 50 \text{ m}$ and $x = 500 \text{ m}$. For $x > 264 \text{ m}$ the concentration maximum is found at the surface due to the vertical widening of the plume in the downstream direction. $\langle C \rangle_{60 \text{ min}}$ also decreases by two orders of magnitude. In contrast to the Gaussian plume model turbulent fluctuations still exist leading to more than one maximum in the downstream direction. Therefore no distinctive concentration maximum at the surface exist for $x > 264 \text{ m}$.

6.2.6 Conclusions

The main differences between the Gaussian plume model and the EULAG model are the missing influence of the topography and the concentration distribution. The impact of the stability classes on the plume shape is not distinctive and therefore the distance until the tracer hits the pedestrian height does not show a dominant variation. Especially under neutral stratification the plume shape and the concentration distribution at the surface differ significantly between the two models. As discussed in Section 5.2.3, increasing wind shear reduces the vertical plume spread. This characteristic behaviour cannot be found in the Gaussian model results. For short term dispersion the analytical Gaussian model cannot be applied because the time average modifies the concentration distribution and variations due to turbulence are not taken into account.

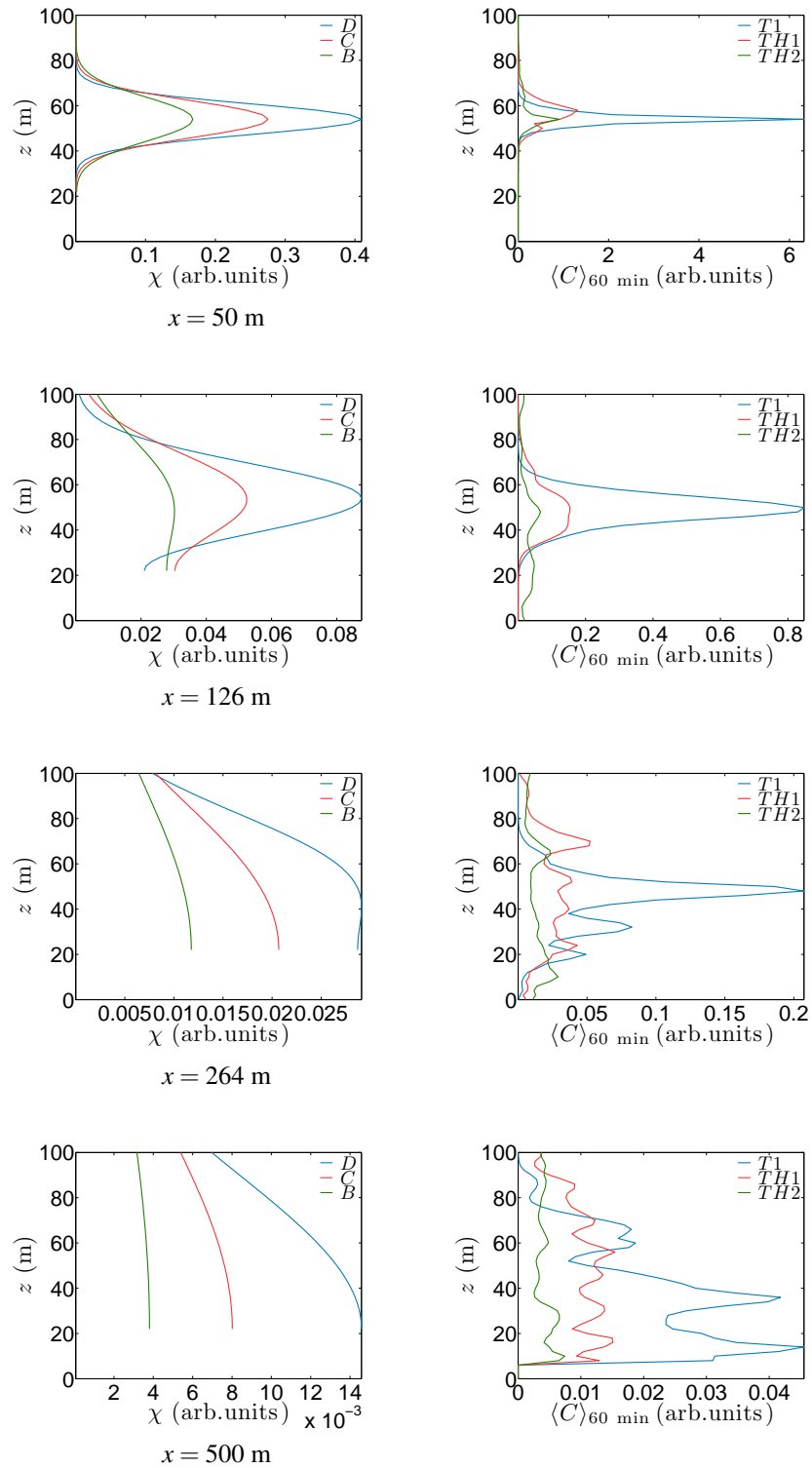


Figure 6.17: [T1,TH1,TH2] Vertical concentration profiles χ (left) and $\langle C \rangle_{60 \text{ min}}$ (right) at four locations x for the release heights $h_t = 54 \text{ m}$ and $z_r = 54.6 \text{ m}$, respectively.

Chapter 7

Tracer Dispersion with Idealised Building and Aare Valley

In this chapter a building, representing Experimentierhalle and ZFA PSI West, is implemented in the idealised Aare canyon setup. It consists of a cuboid and a stack at the northern wall of the building. The IMB method is used to model building and stack (see Section 4.3 for details). Flow and dispersion in this modified setup is compared to turbulent flow and tracer dispersion across the idealised Aare valley as discussed in Chapter 6.

7.1 The Atmospheric Flow

7.1.1 Velocity Profiles

Figure 7.1 shows an $x - z$ cross section for the temporally averaged streamwise $\langle u \rangle_t$ and vertical $\langle w \rangle_t$ velocity under neutral (Z) and convective (ZH) stratification. The building is not heated. In both cases the flow patterns around an isolated obstacle can be observed including the upstream displacement and the recirculation at the windward and leeward wall (see Section 6.1.2 and Hanna et al. (2002)). Behind the building and at the western shore of the Aare the downdraft is more distinctive in the convective case due to the large-scale convective eddies. The dominant velocity changes occur at the edges of the building and at the Aare shore. This can also be seen in Figure 7.2 which

shows the mean profiles $\langle u \rangle_t$ and $\langle w \rangle_t$ at $x = 98$ m (2 m behind the building), $x = 192$ m (west shore) and $x = 330$ m (east shore) as a comparison between the simulations Z, ZH, T1 and TH1. Z/ZH and T1/TH1 are also referred to as disturbed (by the building) and undisturbed flows, respectively.

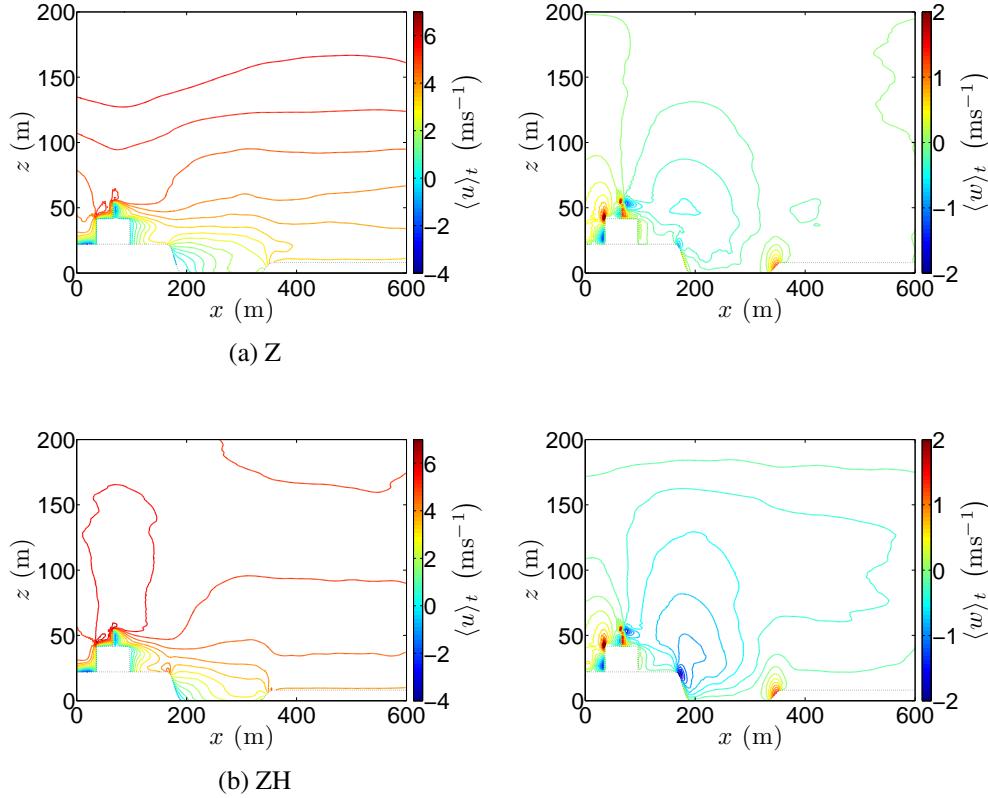


Figure 7.1: [Z,ZH] Contours of temporally averaged 20-min horizontal $\langle u \rangle_t$ and vertical $\langle w \rangle_t$ velocity for neutral (a) and convective stratification (b). The cross section is taken at the position of the stack at $y = 216$ m. The dashed line represents the topography and the building ZFA PSI West.

The velocity variations due to the disturbance occur behind the building where $\langle u \rangle_t \approx 0$. An inflection point forms at the building height $h_{\text{build}} = 20$ m and at the stack height $h_{\text{zfa}} = 32$ m above the west shore, i.e. at 42 m and 54 m above the Aare level (Figure 7.2 (a)). The streamwise velocity decreases below h_{zfa} and remains approximately zero between the surface and the obstacle height. A similar behaviour is found for the other vertical profiles. The minimum of $\langle w \rangle_t$ occurs between the stack and building height for Z and ZH, the downward velocity being larger under convective stratification. For the simulations T1 and TH1 $\langle u \rangle_t$ decreases towards the ground and $\langle w \rangle_t \approx 0$. The

minimum of $\langle w \rangle_t$ at the western surface height (22 m) can be found in all simulations but for Z and ZH it is a secondary minimum (Figure 7.2 (b)). In these cases the main minimum occurs at the building height as does the typical inflection point in the $\langle u \rangle_t$ profile. While the west shore influences the vertical velocity there is no additional influence of the shore on the streamwise velocity because $\langle u \rangle_t$ is approximately 5 times larger than $\langle w \rangle_t$. In the east (Figure 7.2 (c)) there is no distinctive difference between the vertical profiles of the four cases because the flow can downstream readjust to the surface.

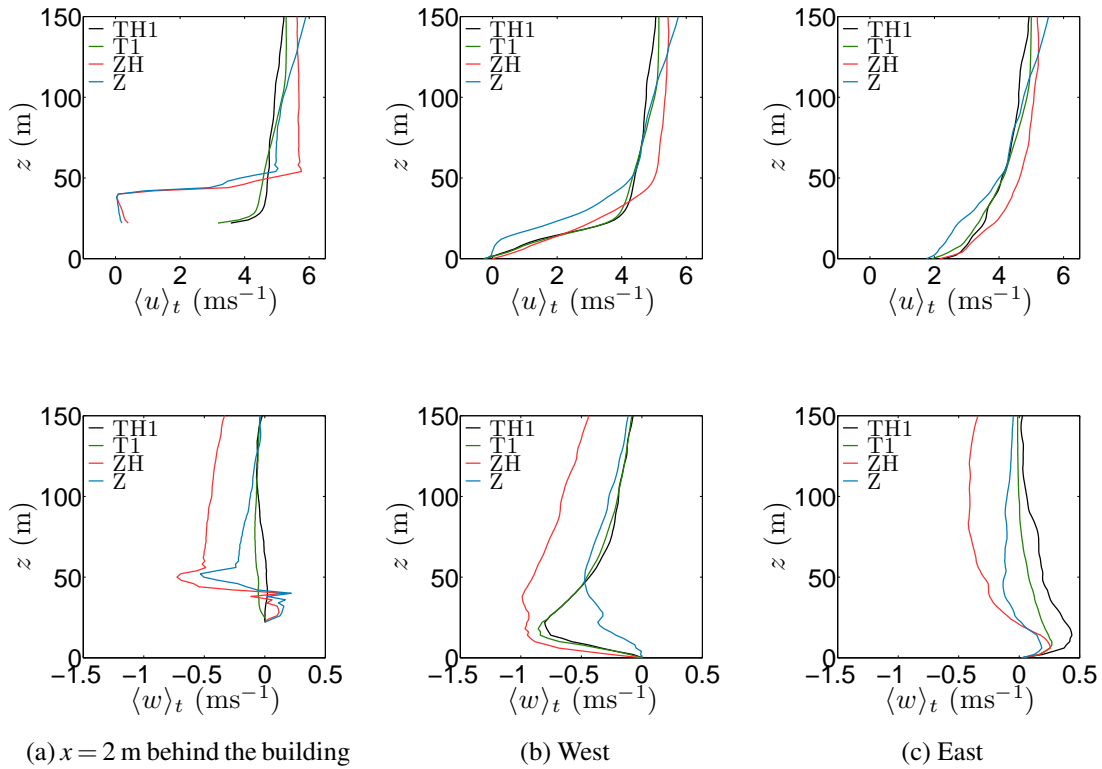


Figure 7.2: [Z,ZH,T1,TH1] Temporally averaged profiles of the streamwise $\langle u \rangle_t$ and vertical velocity $\langle w \rangle_t$ at $x = 98$ m (a), $x = 192$ m (b) and $x = 330$ m (c) for the different simulations. The profiles are averaged over 20 min and taken at the stack position at $y = 216$ m (Z,ZH) and $y = \frac{ny \cdot \Delta y}{2}$ (T1,TH1).

7.1.2 Turbulent Statistics

The vertical profiles of the turbulent kinetic energy $\langle \text{TKE} \rangle$ and the turbulent fluxes of momentum $\langle u'w' \rangle$ and heat $\langle w'\theta' \rangle$ are shown in Figure 7.3. Behind the building

(Figure 7.3 (a)) both the turbulent kinetic energy and the turbulent flux of momentum rise at the building height for the simulations Z and ZH. This is consistent with the inflection point in $\langle u \rangle_t$ that causes instabilities leading to the generation of turbulence. $\langle u'w' \rangle$ shows one maximum slightly below the western terrain height ($z = 22$ m) in all cases except for Z that shows two maxima, one at the western terrain height and one at the building height. The maximum of $\langle \text{TKE} \rangle$ in simulation Z also lies above the maxima of the other simulations which is consistent with $\langle u'w' \rangle$ and $\langle u \rangle_t$ (Figure 7.2 (b)). In the east there is no significant difference between the shape of $\langle u'w' \rangle$ and $\langle \text{TKE} \rangle$ being consistent with the mean velocity profiles. In all cases a turbulent flux of heat exists under convective stratification. It is smaller in the disturbed flow because of the dominant shear generation process caused by the building.

7.1.3 Conclusions

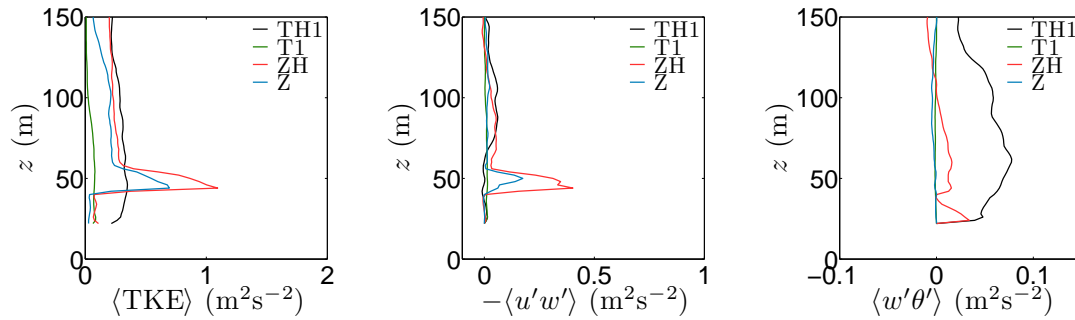
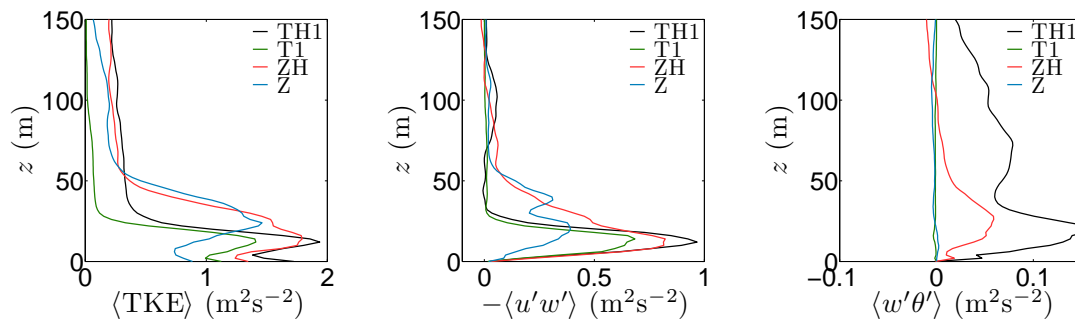
The building and the stack modify the flow so that a characteristic flow over an isolated obstacle develops. The maximum shear stress occurs approximately at the building height and decreases towards zero (see e.g. Cheng and Castro (2002)). The disturbance of the building still dominates the flow at the west shore and the inflection point in $\langle u \rangle_t$ is therefore at the building height for Z,ZH and at the shore height for T1,TH1. In the eastern part of the Aare $\langle \text{TKE} \rangle$ is larger for the convective cases but there is no significant difference between the disturbed and the undisturbed flow.

7.2 Tracer Dispersion

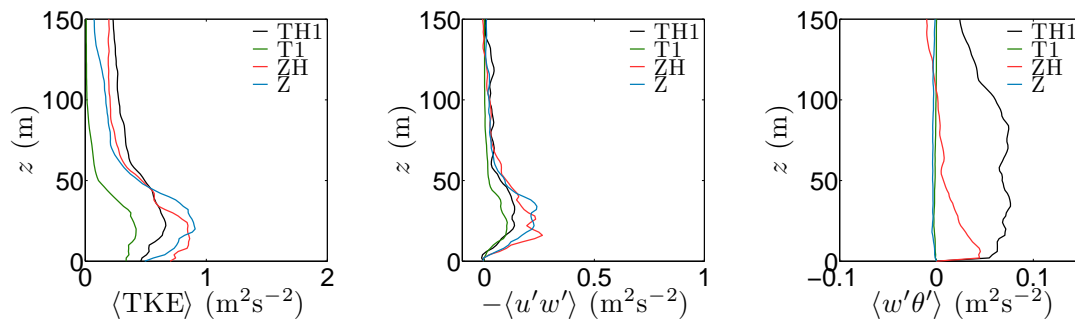
The tracer dispersion over the Aare valley including the obstacle shall be investigated and compared to the dispersion over the idealised Aare valley without the building.

7.2.1 Contour Plots and Vertical Concentration Profiles

Figure 7.4 shows the concentration contours under neutral and convective stratification. The downward transport of C is more distinctive for case Z resulting into a higher concentration above the Aare. The plume height does not rise above the stack


 (a) $x = 2$ m behind the building


(b) West



(c) East

Figure 7.3: [Z,ZH,T1,TH1] Vertical profiles of turbulent kinetic energy $\langle \text{TKE} \rangle$ and the turbulent fluxes $\langle u'w' \rangle$ and $\langle w'\theta' \rangle$ at $x = 98$ m (a), $x = 192$ m (b) and $x = 330$ m (c) for the different case studies. The profiles are averaged over 20 min and taken at the stack position at $y = 216$ m (Z,ZH) and $y = \frac{ny \cdot \Delta y}{2}$ (T1,TH1).

height. This is a difference compared to the flow over the idealised Aare valley where the vertical plume spread becomes larger with growing heat flux. The reason for this is the dominant vertical downdraft behind the building (see Figure 7.1 (b)).

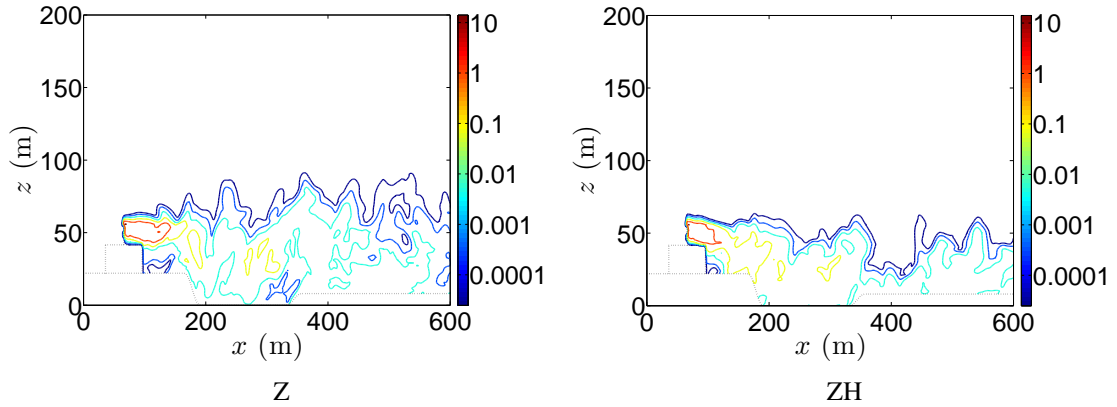


Figure 7.4: [Z,ZH] Dimensionless concentration contours C for the release height $z_r = 55.82$ m showing both the dispersion under neutral (left) and convective (right) stratification at $t = 1600$ s (right). The cross section is taken at the position of the stack at $y = 216$ m. The dashed line represents the topography and the building ZFA PSI West.

Figure 7.5 shows a comparison between the vertical concentration profiles 2 m behind the building, in the west and in the east of the Aare. The profiles are averaged over 20 min and are taken in the centerline of the plume (y -direction). Behind the obstacle (Figure 7.5 (a)) all profiles show a concentration maximum at the release height. For the simulations Z and ZH the concentration is not zero below the building height due to the downward velocity that transports pollutants to the surface. Behind the building and at the western shore the tracer concentration at the surface rises by 2 orders of magnitude (Z,ZH). For the simulation TH1 the tracer hits the ground but the concentration is approximately 4 orders of magnitude smaller compared to the disturbed flow. In the east where the flow readjusts to the surface the profiles assimilate but the concentration is still smaller for the undisturbed flow.

Table 7.1 shows the vertically averaged concentration

$$C_{\text{avg}} = \sum_{k=0}^{nz-1} \frac{C_k}{nz}$$

for each position and case. C_{avg} is highest in the simulation T1 because the flow is neither disturbed by the building nor by a positive surface heat flux. Therefore the dispersion in the y -direction is less distinctive leading to a higher concentration in the centerline. While C_{avg} decreases with distance from the source in the disturbed cases it rises at the east shore for TH1. This systematically changes when the concentration

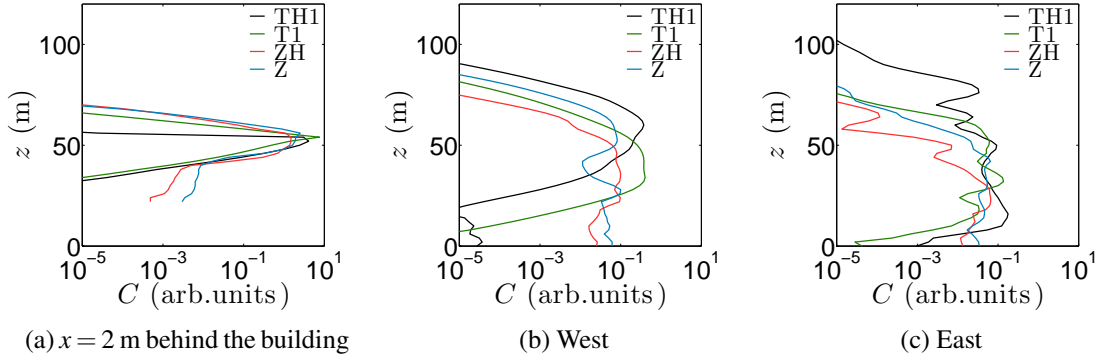


Figure 7.5: [Z,ZH,T1,TH1] Vertical concentration profiles averaged over 20 min at $x = 98$ m (a), $x = 192$ m (b) and $x = 330$ m (c) for the different cases. The profiles are taken at the stack position $y = 216$ m (Z,ZH) and at $y = \frac{ny \cdot \Delta y}{2}$ (T1,TH1). Open boundary conditions at the lateral sides of the domain are used in all simulations.

	$x = 2$ m behind the building	West	East
Z	$C_{\text{avg}} = 0.097$	$C_{\text{avg}} = 0.012$	$C_{\text{avg}} = 0.008$
ZH	$C_{\text{avg}} = 0.074$	$C_{\text{avg}} = 0.012$	$C_{\text{avg}} = 0.005$
T1	$C_{\text{avg}} = 0.136$	$C_{\text{avg}} = 0.023$	$C_{\text{avg}} = 0.010$
TH1	$C_{\text{avg}} = 0.001$	$C_{\text{avg}} = 0.001$	$C_{\text{avg}} = 0.007$

Table 7.1: Vertically averaged concentration values at $t = 20$ min in the y -centerline of the plume at the three positions $x = 98$ m, $x = 192$ m and $x = 330$ m. Open boundary conditions at the lateral sides of the domain are used in all simulations.

is averaged over 20 min (Table 7.2). $\langle C_{\text{avg}} \rangle_t$ decreases with distance from the source in all cases because local concentration peaks disappear.

	$x = 2$ m behind the building	West	East
Z	$\langle C_{\text{avg}} \rangle_t = 0.105$	$\langle C_{\text{avg}} \rangle_t = 0.017$	$\langle C_{\text{avg}} \rangle_t = 0.011$
ZH	$\langle C_{\text{avg}} \rangle_t = 0.077$	$\langle C_{\text{avg}} \rangle_t = 0.016$	$\langle C_{\text{avg}} \rangle_t = 0.007$
T1	$\langle C_{\text{avg}} \rangle_t = 0.106$	$\langle C_{\text{avg}} \rangle_t = 0.048$	$\langle C_{\text{avg}} \rangle_t = 0.013$
TH1	$\langle C_{\text{avg}} \rangle_t = 0.109$	$\langle C_{\text{avg}} \rangle_t = 0.033$	$\langle C_{\text{avg}} \rangle_t = 0.023$

Table 7.2: Same as Table 7.1 but for temporally averaged (over 20 min) concentration values.

Figure 7.6 shows the vertical concentration profiles 2 m behind the building at different y -positions: in the centerline of the plume and with a 10 m distance to the north ($y = 226$ m) and to the south ($y = 206$ m). The concentration above the building height

is largest in the centerline of the plume under both neutral and convective stratification. Towards the surface C becomes larger in the south. In both cases the concentration values are smaller in the north than in the south because the flow is not directly disturbed by the building. The building disturbance leads to a larger spanwise dispersion to the south.

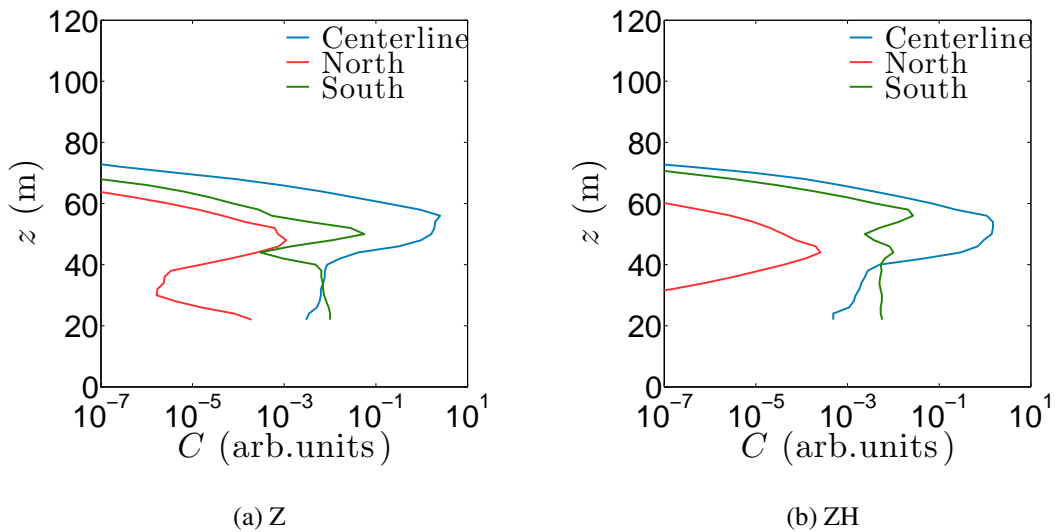


Figure 7.6: [**Z,ZH**] Vertical concentration profiles 2 m behind the building averaged over 20 min. The profiles are taken at the stack position $y = 216$ m (blue), in the north of the stack at $y = 226$ m (red) and in the south of the stack at $y = 206$ m (green).

7.2.2 Conclusions

The main difference between the tracer dispersion in the disturbed and undisturbed cases concerns the plume rise under convective and neutral stratification. When an obstacle is implemented into the domain the upward plume spread is significantly smaller in the buoyant case because of the dominant vertical downdraft behind the building. For both thermal states the circulation behind the obstacle causes a higher concentration at the surface and the tracer hits the ground closer to the source. The concentration in the north of the stack is smaller than the concentration in the south of the stack, i.e., the building disturbance leads to a larger spanwise dispersion to the south.

Chapter 8

Summary and Outlook

In this PhD thesis the dispersion of a passive scalar in the atmospheric boundary layer is investigated. Three different setups are applied, consisting of a flat terrain, an idealised Aare valley and the latter one extended by a building, representing the source of radionuclides at the Paul Scherrer Institute. The focus is on the influence of topography, release height and thermal stratification on turbulent flow and tracer dispersion. For this purpose different simulations are performed under neutral and convective thermal stratification with tracer release heights of 12 m, 32 m and 52 m above the surface. Flow and dispersion across the idealised Aare valley is simulated using terrain-following coordinates based on the classical Gal-Chen and Sommerville transformation (Gal-Chen and Somerville, 1975), while the numerical approach to model the building is based on the IMB method (Goldstein et al., 1993; Mittal and Iaccarino, 2005). The simulations are performed with a high spatial resolution of 2 m in the x -, y - and z -direction applying the numerical flow solver EULAG (Prusa et al., 2008).

A roughness parameterisation included in a flat terrain setup leads to a velocity change close to the surface and a vertical plume spread under neutral stratification. Therefore the pollutants can reach the ground at smaller distances to the source with a shorter advection time, compared to the dispersion over a flat homogeneous terrain. A comparison of the tracer dispersion under both neutral and convective conditions shows that the wind shear reduces the looping of the plume, resulting in a reduction of the vertical plume spread. Increasing wind therefore tends to advect the plume horizontally for a longer time.

The turbulent flow through the idealised Aare canyon setup can be described by an IRF regime in analogy to a step down canyon. The characteristic profile includes the upstream displacement and recirculation zone at the windward side, the cavity zone at the leeward side and the wake zone downwind of the cavity. As a consequence, a simple surface roughness change as applied in the flat terrain setup cannot mimic the complex flow above the Aare river. At the western Aare shore the mechanical turbulence dominates buoyancy due to the characteristic canyon flow profile, while its influence decreases further downstream where the thermal turbulence becomes more important. With increasing surface heat flux the release height has less influence on the tracer dispersion because larger eddies form which transport pollutants to the surface. Due to the absence of buoyant convection the influence of topographic inhomogeneities becomes more significant under neutral stratification.

The third setup is modelled using terrain-following coordinates and the IMB method for the idealised Aare valley and the additional building, respectively. The building in the domain influences the flow substantially in the vicinity of the building and leads to a higher pollutant concentration both behind the building and at the western shore of the Aare. In the buoyant case the upward plume spread is distinctly smaller than the plume spread under neutral stratification because of a dominant vertical downdraft behind the building. This is in contrast to the plume behaviour over both a flat terrain and the idealised Aare valley setup where a surface heat flux leads to a plume spread in the vertical.

Atmospheric flow and tracer dispersion differ significantly within the three setups. A simple roughness parameterisation as it is used in Gaussian plume models, is neither sufficient to take into account the turbulent phenomena that evolve in particular near the Aare canyon and in the lee of the building, nor their effects on the tracer dispersion. An investigation of the mean maximum concentration values with distance from the source shows a decrease with $\exp(-x)$ applying EULAG compared to a decrease with $\exp(-x^2)$ in Gaussian models. The Gaussian plume model ESS41 that is used at PSI predicts an hourly averaged concentration distribution. In contrast, turbulent flow and plume dispersion can be modelled with a high temporal and spatial resolution using EULAG. Apart from numerical restrictions there are almost no constraints on time step and implemented topography. In case of an incident EULAG would in principle be capable to predict the emissions, potentially with a high accuracy, taking into account temporal and local concentration peaks and the pollution at the PSI area. Realistic

initial and boundary conditions are needed for this purpose, such as wind speed, wind direction, temperature or humidity. These meteorological conditions can be taken from another meteorological model (e.g. COSMO-2) or from weather stations that are setup at different locations and heights.

The combination of terrain-following coordinates and the IMB method as used in the third computational setup is a promising approach to model the dispersion of radionuclides at the PSI. A reasonable extension of the model could be as follows:

- Additional buildings are implemented into the domain, e.g. the accelerator SLS in the western area or an array of obstacles in the eastern area of the river Aare. A heating of these buildings and their response on the turbulence structure of the atmospheric flow shall be investigated.
- The application of a stable thermal stratification or a surface heat flux above the Aare, that differs from the surrounding area, could result in different flow and concentration patterns.
- The terrain shape at and around the PSI is more complex than the setups used for the simulations. There is a hill in the west, a forest in the east and trees at the Aare shores. An extension of the domain including the line of hills in the west of the PSI (see Figure 1.2) could have an influence on the atmospheric flow under west wind conditions. The results can be compared with well-studied valley and slope wind patterns (e.g. Rampanelli et al., 2004; Schmidli et al., 2011).
- The forest in the western part could be modelled using fractal Pythagoras trees as applied in Schrötle and Dörnbrack (2012). The influence on the tracer dispersion is probably most significant under east wind conditions and therefore the wind directions should vary.
- Finally, the whole PSI topography based on Swiss topo data shall be implemented into the EULAG model investigating flow and dispersion under different weather conditions.

Recommendations to protect the population could be given based on the EULAG model results. For such an operational setup it would be important to use both reasonable initial and boundary conditions and a realistic topography. The capability to

implement this complex topography into the model could be shown. With these data new simulations can be performed to determine the concentration distribution at different places at the PSI and its surroundings. For the verification of the results there are already setup three measuring stations detecting the γ -radiation that is proportional to the concentration of the β^+ emitters. Two stations are placed in the western part of the PSI, one close to the surface and one above the Experimentierhalle close to the ZFA. The third station is setup in the east near the Aare river. With the measured data it should be possible to compare concentration differences and time patterns of the release with the model results of a more realistic setup.

The multiscale numerical flow solver EULAG can thus overcome important weaknesses of Gaussian plume models and is therefore in principle capable to replace the model ESS41 for modelling the tracer emissions in the future.

Bibliography

- Ahmad, K., M. Khare, and K. Chaudhry, 2005: Wind tunnel simulation studies on dispersion at urban street canyons and intersections—a review. *J. Wind Eng. Ind. Aerodyn.*, **93**, 697–717, doi:10.1016/j.jweia.2005.04.002.
- Ahrens, C., P. Jackson, and C. Jackson, 2012: *Meteorology Today. An Introduction to Weather, Climate, and the Environment*. Brooks Cole Pub Co.
- Assimakopoulos, V., H. ApSimon, and N. Moussiopoulos, 2003: A numerical study of atmospheric pollutant dispersion in different two-dimensional street canyon configurations. *Atmos. Environ.*, **37**, 4037–4049, doi:10.1016/S1352-2310(03)00533-8.
- Blackadar, A., 1996: *Turbulence and Diffusion in the Atmosphere*. Springer-Verlag, Berlin-Heidelberg.
- Britter, R. E. and S. R. Hanna, 2003: Flow and Dispersion in Urban Areas. *Annual Review of Fluid Mechanics*, **35**, 469–496, doi:10.1146/annurev.fluid.35.101101.161147.
- Cheng, H. and I. P. Castro, 2002: Near wall flow over urban-like roughness. *Boundary-Layer Meteorol.*, **104**, 229–259.
- Coceal, O., T. G. Thomas, I. P. Castro, and S. E. Belcher, 2006: Mean Flow and Turbulence Statistics Over Groups of Urban-like Cubical Obstacles. *Boundary-Layer Meteorol.*, **121**, 491–519, doi:10.1007/s10546-006-9076-2.
- Dosio, A., J. de Arellano, and A. Holtslag, 2003: Dispersion of a Passive Tracer in Buoyancy- and Shear-Driven Boundary Layers. *J. Appl. Meteorolog.*, **42**, 1116–1130.

- Fröhlich, J., 2006: *Large Eddy Simulation turbulenter Strömungen*. Vieweg+Teubner Verlag.
- Gal-Chen, T. and R. C. J. Somerville, 1975: On the Use of a Coordinate Transformation for the Solution of the Navier-Stokes Equations Considerable progress has been made in the last decade toward a better numerical solution of the Navier-Stokes equations without topography . The simulation of fluid. *J. Comput. Phys.*, **228**, 209–228.
- German Federal Ministry of Justice, 1990: Allgemeine Verwaltungsvorschrift zu §45 Strahlenschutzverordnung: Ermittlung der Strahlenexposition durch die Ableitung radioaktiver Stoffe aus kerntechnischen Anlagen (AVV). *Bundesanzeiger*, **42**, 1–29.
- Ghizaru, M., P. Charbonneau, and P. K. Smolarkiewicz, 2010: Magnetic cycles in global large-eddy simulations of solar convection. *The Astrophysical Journal Letters*, **715**, 133–137, doi:10.1088/2041-8205/715/2/L133.
- Goldstein, D., R. Handler, and L. Sirovich, 1993: Modeling a No-Slip Boundary with an External Force Field. *J. Comput. Phys.*, **105**, 354–366.
- Grabowski, W. W., 2007: Representation of Turbulent Mixing and Buoyancy Reversal in Bulk Cloud Models. *J. Atmos. Sci.*, **64**, 3666–3680, doi:10.1175/JAS4047.1.
- Hanna, S., S. Tehranian, B. Carissimo, R. Macdonald, and R. Lohner, 2002: Comparisons of model simulations with observations of mean flow and turbulence within simple obstacle arrays. *Atmos. Environ.*, **36**, 5067–5079, doi:10.1016/S1352-2310(02)00566-6.
- Huang, H., Y. Akutsu, M. Arai, and M. Tamura, 2000: A two-dimensional air quality model in an urban street canyon: evaluation and sensitivity analysis. *Atmos. Environ.*, **34**, 689–698, doi:10.1016/S1352-2310(99)00333-7.
- International Atomic Energy Agency (IAEA), 2000: Regulatory Control of Radioactive Discharges to the Environment. *IAEA Safety Standard Series*, **No. WS-G-2**, 1–43.
- 2002: Dispersion of Radioactive Material in Air and Water and Consideration of Population Distribution in Site Evaluation for Nuclear Power Plants. *IAEA Safety Standard Series*, **NS-G-3.2**, 1–32.

- Kanda, M., R. Y. O. Moriwaki, and F. Kasamatsu, 2004: Large-eddy simulation of turbulent organized structures within and above explicitly resolved cube arrays. *Boundary-Layer Meteorol.*, 343–368.
- Kastner-Klein, P., R. Berkowicz, and R. Britter, 2004: The influence of street architecture on flow and dispersion in street canyons. *Meteorol. Atmos. Phys.*, **87**, 121–131, doi:10.1007/s00703-003-0065-4.
- Kljun, N., M. W. Rotach, and H. P. Schmid, 2002: A three-dimensional backward Lagrangian footprint model for a wide range of boundary-layer stratifications. *Boundary-Layer Meteorol.*, **103**, 205–226.
- Klug, W., 1969: Ein Verfahren zur Bestimmung der Ausbreitungsbedingungen aus synoptischen Beobachtungen. *Staub-Reinhalt. Luft*, **29**, 143–147.
- Leonard, A., 1974: Energy Cascade in large-eddy simulations of turbulent fluid flows. *Adv. Geophys.*, **18A**, 237–248.
- Li, X., C. Liu, D. Leung, and K. Lam, 2006: Recent progress in CFD modelling of wind field and pollutant transport in street canyons. *Atmos. Environ.*, **40**, 5640–5658, doi:10.1016/j.atmosenv.2006.04.055.
- Milliez, M. and B. Carissimo, 2006: Numerical simulations of pollutant dispersion in an idealized urban area, for different meteorological conditions. *Boundary-Layer Meteorol.*, **122**, 321–342, doi:10.1007/s10546-006-9110-4.
- Mittal, R. and G. Iaccarino, 2005: Immersed Boundary Methods. *Annu. Rev. Fluid Mech.*, **37**, 239–261, doi:10.1146/annurev.fluid.37.061903.175743.
- Moeng, C.-H. and P. Sullivan, 1994: A Comparison of Shear- and Buoyancy-Driven Planetary Boundary Layer Flows. *J. Atmos. Sci.*, **51**, 999–1022.
- Oke, T., 1988: Street design and urban canopy layer climate. *Energy and Buildings*, **11**, 103–113, doi:10.1016/0378-7788(88)90026-6.
- Panofsky, H. and A. Townsend, 1963: Change of terrain roughness and the wind profile. *Quart. J. R. Met. Soc.*, 147–155.

- Park, S.-B., J.-J. Baik, S. Raasch, and M. O. Letzel, 2012: A Large-Eddy Simulation Study of Thermal Effects on Turbulent Flow and Dispersion in and above a Street Canyon. *J. Appl. Meteorol. Climatol.*, **51**, 829–841, doi:10.1175/JAMC-D-11-0180.1.
- Pasquill, F., 1961: The estimation of the dispersion of windblown material. *Met. Mag.*, **90**, 33–49.
- Peterson, E. W., 1969: Modification of mean flow and turbulent energy by a change in surface roughness under conditions of neutral stability. *Quart. J. R. Met. Soc.*, **95**, 561–575.
- Pope, S., 2000: *Turbulent Flows*. Cambridge University Press, Cambridge.
- Prusa, J. M., P. K. Smolarkiewicz, and A. a. Wyszogrodzki, 2008: EULAG, a computational model for multiscale flows. *Computers & Fluids*, **37**, 1193–1207, doi:10.1016/j.compfluid.2007.12.001.
- Rampanelli, G., D. Zardi, and R. Rotunno, 2004: Mechanisms of Up-Valley Winds. *J. Atmos. Sci.*, **61**, 3097–3111.
- Rao, K. S., J. C. Wyngaard, and O. R. Coté, 1973: The Structure of the Two-Dimensional Internal Boundary Layer over a Sudden Change of Surface Roughness. *J. Atmos. Sci.*, **31**, 738–746.
- Rotach, M., S.-E. Gryning, and C. Tassone, 1996: A two-dimensional Lagrangian stochastic dispersion model for daytime conditions. *Quart. J. R. Met. Soc.*, **122**, 367–389.
- Rotach, M. W., S.-E. Gryning, E. Batchvarova, A. Christen, and R. Vogt, 2004: Pollutant dispersion close to an urban surface - the BUBBLE tracer experiment. *Meteorol. Atmos. Phys.*, **87**, 39–56, doi:10.1007/s00703-003-0060-9.
- Schmidli, J., B. Billings, F. K. Chow, S. F. J. de Wekker, J. Doyle, V. Grubišić, T. Holt, Q. Jiang, K. a. Lundquist, P. Sheridan, S. Vosper, C. D. Whiteman, A. a. Wyszogrodzki, and G. Zängl, 2011: Intercomparison of Mesoscale Model Simulations of the Daytime Valley Wind System. *Mon. Weather Rev.*, **139**, 1389–1409, doi:10.1175/2010MWR3523.1.

- Schmidt, H. and U. Schumann, 1989: Coherent structure of the convective boundary layer derived from large-eddy simulations. *J. Fluid Mech.*, **200**, 511–562.
- Schrötte, J. and A. Dörnbrack, 2012: Turbulence structure in a diabatically heated forest canopy composed of fractal Pythagoras trees. *Theor. Comput. Fluid Dyn.*, **27**, 337–359, doi:10.1007/s00162-012-0284-8.
- Schumann, U., 1991: Subgrid Length-Scales for Large-Eddy Simulation of Stratified Turbulence. *Theor. Comput. Fluid Dyn.*, **2**, 279–290.
- Sini, O. I. S., S. Anquetint, E. Centrale, N. Cedex, and E. Bldo, 1996: Pollutant dispersion and thermal effects in urban street canyons. *Atmos. Environ.*, **30**, 2659–2677.
- Slade, D., 1968: Meteorology and Atomic Energy 1968. *U.S. Atomic Energy Commission Office of Information Services*, 1–447.
- Smagorinsky, J., 1963: general circulation experiment with the primitive equations, I, The basic experiment. *Mon. Weather Rev.*, **91**, 99–164, doi:10.1126/science.27.693.594.
- Smolarkiewicz, P., 1983: A Simple Positive Definite Advection Scheme with Small Implicit Diffusion. *Mon. Weather Rev.*, **111**, 479–486.
- Smolarkiewicz, P., R. Sharman, J. Weil, S. Perry, D. Heist, and G. Bowker, 2007: Building resolving large-eddy simulations and comparison with wind tunnel experiments. *J. Comput. Phys.*, **227**, 633–653, doi:10.1016/j.jcp.2007.08.005.
- Smolarkiewicz, P. K. and L. G. Margolin, 1998: MPDATA : A Finite-Difference Solver for Geophysical Flows. *J. Comput. Phys.*, **140**, 459–480.
- Sorbjan, Z., 1996: Numerical Study of Penetrative and "Solid Lid" Nonpenetrative Convective Boundary Layers. *J. Atmos. Sci.*, **53**, 101–112.
- Spichtinger, P., K. M. Gierens, and C. Science, 2009: Modelling of cirrus clouds – Part 1a : Model description and validation. *Atmos. Chem. Phys.*, **9**, 685–706.
- Stull, R., 1989: *An Introduction to Boundary Layer Meteorology*. Kluwer Academic Publishers, Dordrecht.

- Swiss Federal Nuclear Safety Inspectorate, 2009: *Berechnung der Strahlenexposition in der Umgebung aufgrund von Emissionen radioaktiver Stoffe aus Kernanlagen - Richtlinie für die schweizerischen Kernanlagen G14*.
- Taylor, P. A., 1968: On wind and shear profiles above a change in surface roughness. *Quart. J. R. Met. Soc.*, 77–91.
- Turner, D., 1964: A diffusion model for an urban area. *J. Appl. Meteorolog.*, **3**.
- United Nations Population Division, 2011: World Urbanization Prospects, the 2011 Revision.
URL <http://esa.un.org/unup/CD-ROM/Urban-Agglomerations.htm>
- Vardoulakis, S., B. E. Fisher, K. Pericleous, and N. Gonzalez-Flesca, 2003: Modelling air quality in street canyons: a review. *Atmos. Environ.*, **37**, 155–182, doi:10.1016/S1352-2310(02)00857-9.
- Vogt, K., 1977: Empirical investigations of the diffusion of waste air plumes in the atmosphere. *Nucl. Technol.*, **34**, 43–57.
- Warn-Varnas, A., J. Hawkins, P. Smolarkiewicz, S. Chin-Bing, D. King, and Z. Hallock, 2007: Solitary wave effects north of Strait of Messina. *Ocean Modelling*, **18**, 97–121, doi:10.1016/j.ocemod.2007.03.003.
- Wyszogrodzki, A. A. and P. K. Smolarkiewicz, 2010: Proceedings of the ASME 2010 3rd Joint US-European Fluids Engineering Summer Meeting and 8th International Conference on Nanochannels, Microchannels, and Minichannels FEDSM-ICNMM2010-30157. *Large-Eddy Simulation of Urban Flows: Porous-Media Analogy*, 1–8.
- Xie, Z.-T. and I. P. Castro, 2009: Large-eddy simulation for flow and dispersion in urban streets. *Atmos. Environ.*, **43**, 2174–2185, doi:10.1016/j.atmosenv.2009.01.016.
- Xie, Z.-T., O. Coceal, and I. P. Castro, 2008: Large-Eddy Simulation of Flows over Random Urban-like Obstacles. *Boundary-Layer Meteorol.*, **129**, 1–23, doi:10.1007/s10546-008-9290-1.
- Yee, E., 2004: Concentration fluctuation measurements in a plume dispersing through a regular array of obstacles. *Boundary-Layer Meteorol.*, **111**, 363–415.

Zenger, A., 1998: *Atmosphärische Ausbreitungsmodellierung: Grundlagen und Praxis*. Springer-Verlag, Berlin-Heidelberg.

Curriculum Vitae

Personal Information

Name: Irina Heese
Date of Birth: 08 October 1979
Nationality: German

Professional Experience

2009 – 2013 **ETH Zurich / Paul Scherrer Institute, Switzerland**
Doctoral Student

2008 – 2009 **Westfälische Wilhelms-Universität Münster, Germany**
Research Assistant

2007 – 2008 **Westfälische Wilhelms-Universität Münster, Germany**
Undergraduate Teaching Assistant (physics laboratory)

Education

2009 – 2013 **ETH Zurich / Paul Scherrer Institute, Switzerland**
Dr. sc. ETH Zurich
Thesis successfully defended in September 2013 with the title:
"Large Eddy Simulation of Tracer Dispersion in an Idealised River
Canyon Setup"

2003 – 2008 **Westfälische Wilhelms-Universität Münster, Germany**
Physik Diplom (equivalent to Physics MSc) 2008

1999 – 2003 **Westfälische Wilhelms-Universität Münster, Germany**
Friedrich-Schiller-Universität Jena, Germany
Studies of Political Science and Law

1990 – 1999 **Grammar School (Gymnasium), Germany**
Abitur (equivalent to A-Levels) 1999

Organisational Skills

2010 **Course on Project Management, Switzerland**

2002 – 2003 **AEGEE (Association des Etats Généraux des Etudiants de l'Europe)**
Member of the Board

June 11, 2014

Acknowledgements

Ich möchte allen, die zur Entstehung dieser Dissertation beigetragen haben, herzlich danken.

An erster Stelle bedanke ich mich bei Heini Wernli für die kontinuierliche Unterstützung und Motivation während meiner gesamten Zeit als Doktorandin. Bei Johannes Keller bedanke ich mich für wertvolle Diskussionen zu Beginn meiner Doktorarbeit und sein hilfreiches Feedback zu den Kapiteln dieser Dissertation. Andreas Dörnbrack danke ich für die Hilfe bei der Anwendung von EULAG und die Durchsicht dieser Arbeit. Besonderer Dank gilt Sabine Mayer und Christian Wernli, welche die Doktorarbeit initiierten und mir die Möglichkeit gaben, dieses interessante Thema zu bearbeiten.

Björn Broetz danke ich für die Unterstützung besonders bei technischen Problemen und die Zeit, die er sich stets bei meinen Aufenthalten am DLR nahm. Gernot Butterweck danke ich für die Mithilfe beim Einstieg ins Thema und bei der Erstellung des Forschungsantrages.

Allen Mitgliedern der Arbeitsgruppe "Atmospheric Dynamics" danke ich für das angenehme Arbeitsklima. Im Besonderen danke ich Franziska und Winni für die wissenschaftlichen und nicht-wissenschaftlichen Diskussionen im Büro sowie zahlreiche Konzert- und Opernbesuche.

Den Kollegen am PSI danke ich für die freundliche Aufnahme als einzige Doktorandin in der Abteilung. Hierbei möchte ich vor allem Heide Beer danken, die mir als Gotte bei der Eingewöhnung half und mich mit vielen wertvollen Tipps unterstützte. Dem ENSI danke ich für die finanzielle Unterstützung und das Interesse an meiner Arbeit.

Zuletzt danke ich meiner Familie, meinen Freunden und Clemens, der mir den Rückhalt gab, um diese Dissertation zu beenden.